T.C.

DOKUZ EYLÜL
ÜNİVERSİTESİ İZMİR
ULUSLARARASI BİYOTIP VE
GENOM ENSTİTÜSÜ

THE VITAL ROLE OF THE ATG9A GENE IN THE SURVIVAL OF MALIGNANT PLEURAL MESOTHELIOMA CELLS

MERVE UYSAL

DEPARTMENT OF GENOMICS AND MOLECULAR
BIOTECHNOLOGY

MASTER THESIS

IZMIR-2023

Thesis Code: DEU.IBG.MSc- 2020850014

T.C.
DOKUZ EYL¦ L ¦ NĶVERSĶTESĶ
ĶZMĶR ULUSLARARASI
BĶYOTIP VE GENOM ENSTĶT¦ S¦

THE VITAL ROLE OF THE ATG9A GENE IN THE SURVIVAL OF MALIGNANT PLEURAL MESOTHELIOMA CELLS

DEPARTMENT OF GENOMICS AND MOLECULAR BIOTECHNOLOGY

MASTER THESIS

MERVE UYSAL

Adviser: Assoc. Prof. Serif SENTURK

(This PROJECT is partially supported by The Scientific and Technological Research Council of Turkey (TUBITAK) with the grant number 117Z227)

Thesis Code: DEU.IBG.MSc-2020850014

T.C.
DOKUZ EYLÜL ÜNİVERSİTESİ

İZMİR ULUSLARARASI BİYOTIP VE GENOM ENSTİTÜSÜ

YÜKSEK LİSANS TEZ SAVUNMA SINAVI TUTANAĞI

Dokuz Eylül Üniversitesi İzmir Uluslararası Biyotıp ve Genom Enstitüsü Genom Bilimleri ve Moleküler Biyoteknoloji Anabilim Dalı Moleküler Biyoloji ve Genetik Yüksek Lisans Programı 2020850014 numaralı öğrencisi Merve Uysal, "The Vital Role of the ATG9A Gene in the Survival of Malignant Pleural Mesothelioma Cells" konulu Yüksek Lisans tezini 21/07/2023 tarihinde yapılan savunma sınavı sonucunda başarılı / başarısız olmuştur.

BAŞKAN

Doç. Dr. Şerif Şentürk

JÜRİ ÜYESİ	**JÜRİ ÜYESİ**
Doç. Dr. Özden Yalçın Özuysal	Dr. Öğr. Üyesi Yavuz Oktay

TABLE OF CONTENTS

LIST OF TABLES

LIST OF FIGURES

ABBREVIATIONS

MPM	Malignant Pleural Mesothelioma
ATG9A	Autophagy Related 9A
TMEM41B	Transmembrane Protein 41B
gRNA	Guide RNA
CRISPR	Clustered Regularly Interspaced Short Palindromic Repeats
Cas9	CRISPR Associated Endonuclease 9
SA-ɓ-Gal	Senescence-Associated ɓ-galactosidase
BrdU	Bromodeoxyuridine
IF	Immunofluorescence
MTT	3-(4,5-Dimethylthiazol-2-yl)-2,5-Diphenyltetrazolium Bromide
qRT-PCR	Quantitative Real Time Polymerase Chain Reaction
PI	Propidium Iodide
GSEA	Gene Set Enrichment Analysis
ROS	Reactive Oxygen Species
CNA	Copy Number Alteration
CMA	Chaperone-Mediated Autophagy
PAS	Pre-Autophagosomal Structure

ERES	ER Exit Site
IM	Isolation Membrane
NAC	N Acetyl L cysteine

ACKNOWLEDGEMENT

I would like to thank the T¦ BĶTAK-BĶDEB 2210-A Domestic General Master Scholarship Program for providing me with financial support during my master studies. Next, I would like to express my gratitude to my supervisor, Assoc. Prof. Serif SENTURK, for giving me the opportunity to pursue a master's degree and for helping me to find the field I want to work in for the rest of my life. He has always been there for me when my motivation was low, encouraging me to return to my work with renewed enthusiasm. He has not only been a supervisor but also a mentor throughout my life, creating a warm environment where I could freely discuss any topic. I am immensely grateful to him, especially for introducing me to the amazing people in his lab. They have become more than just lab colleagues; they have become my family. I never felt alone in Izmir because they were always by my side.

First and foremost, I want to thank Ec¿k Sultan (Ece CAKIROGLU) and Dilara DEMIRCI for patiently and generously teaching me everything I know when I first joined the lab. They are my respected teachers, and they will be the sisters I turn to when I encounter difficulties. Specially, I would like to thank Ece CAKIROGLU for her contribution more than anyone else during the thesis writing process. Also, Ec¿k Sultan please don't know every question we ask. Sudiĸ (Sude ERIS), you are my brilliant hacker. Thank you so much for your exceptional analyses on the computer and for always sincerely helping me whenever I encountered the slightest issue on the computer. Especially for your meticulous care and effort in handling my RNA sequencing data during those incredibly busy times, I am immensely grateful. Moreover, you have always been there for me during the worst moments in my life, and I cannot repay you enough. Zeyno (Medine Zeynep GUNGOR), you are my constant co-author. Only you and I know the experiences we have been through and the challenges we have overcome together. You are my sister, friend, and confidante, and I hope one day we will become partners in our dreamed-of company. Minu

(Minenur KALYONCU), you are my psychologist. I'm grateful that you joined our lab and brought us all together. Our lab has become vibrant because of you. Throughout this process, you have become a sister to me, always by my side, and I felt your support at all times. Thank you very much. I would also like to express my gratitude to Beng ablam (Bengisu ULUATA DAYANC) and Ayb¿k (Fatma Aybuke MAZI) because both of you have become sisters to me. Bengisu, you are the most courteous person in our lab, and Ayb¿k, you are the most angry bird. Thank you for kindly answering all my questions and rushing to my aid whenever I had a problem. Buse (Buse AKDEMIR) and Ege (Ege GULFIRAT), you are the young members of our lab, and I feel fortunate to have met you and had the opportunity to work together. To all my sisters in the lab, I hope you all achieve your desired positions in life and become highly successful. You all deserve the best in life.

Ay-a OZKAN and Esma OZKAN, you are my dear sisters. I am incredibly grateful for your presence in my life and your unwavering support. You lifted me up every time I fell, and I'm so thankful that you exist. And of course, Bartu KULAK, thank you for always being by my side, supporting me through all the stresses and calming me when experiments didn't go well. I am immensely grateful for your financial and emotional support. Also, thank you for never hesitating to help me with my analyses or any tasks in the lab. Without your support, I couldn't have completed most of the analyses or this master program. I love you.

Of course, I would like to express my gratitude to my dear family, who have been my biggest source of spiritual support throughout my master's and thesis writing journey. Especially, I want to thank my mother for her unconditional love and support.

And finally, I want to thank my beloved Hedwig, my pet budgie. Even though she is currently unaware, chirping away on top of my computer, I cannot fully express the moral and motivational support she brings to my life. Thank you for being with me.

THE VITAL ROLE OF THE ATG9A GENE IN THE SURVIVAL OF MALIGNANT PLEURAL MESOTHELIOMA CELLS

Merve Uysal, Dokuz Eylul University, Izmir International Biomedicine and Genome Institute, merve.uysal@ibg.edu.tr

ABSTRACT

Malignant pleural mesothelioma (MPM) is a cancer that originates in the mesothelial cells lining the pleural surface of the chest wall and lung. Despite its rarity, the global impact of MPM underscores the urgent need to identify specific therapeutic targets and novel risk factors associated with disease. However, the characterization of genes and pathways involved in MPM carcinogenesis with potential therapeutic implications has been limited. To address this gap, our laboratory has conducted molecular studies based on genome-wide CRISPR/Cas9 screening on MPM cell lines. Through this approach, we identified several candidate genes that potentially play a vital role in MPM carcinogenesis. One of these associated with cancer cell survival is the autophagy related 9A (ATG9A) gene. To elucidate the role of ATG9A in MPM, we employed CRISPR/Cas9 technology to knockout the *ATG9A* gene in MPM cells. Our studies demonstrate that depletion of *ATG9A* gene elicits a dramatic reduction in cellular proliferation. Importantly, the observed phenotypes were rescued by *ATG9A* overexpression. Moreover, these phenotypic changes were accompanied by senescence and apoptosis, likely triggered by DNA damage mediated by reactive oxygen species (ROS). Transcriptomic analysis of *ATG9A* depleted cells revealed gene clusters associated with cellular senescence and apoptosis pathways. Finally, our research underscores the essential role of both the canonical and non-canonical functions of ATG9A, such as lipid transport and mitophagy, in the MPM survival. These novel findings contribute to a better understanding of MPM pathogenesis and provide valuable insights into potential therapeutic strategies targeting ATG9A.

Keywords: Malignant Pleural Mesothelioma, ATG9A, Autophagy, CRISPR/Cas9

MALĶGN PLEVRAL MEZOTELYOMA H¦ CRELERĶNĶN

SAĜ KALIMINDA ATG9A GENĶNĶN HAYATĶ ROL¦

Merve Uysal, Dokuz Eyl¿l ¦ niversitesi Ķzmir Uluslararasē Biyotēp ve Genom Enstit¿s¿, merve.uysal@ibg.edu.tr

<u>¥ ZET</u>

Malign Plevral Mezotelyoma (MPM), gºĝ¿s duvarē ve akciĝerin plevral y¿zeyini kaplayan mezotelyal h¿crelerden meydana gelen bir kanserdir. Nadir olmasēna raĝmen, MPM' in k¿resel etkisi, hastalēkla iliĸkili ºzel terapºtik hedefler ve yeni risk faktºrlerinin acil olarak belirlenmesi gerekliliĝini vurgular. Ancak, MPM'in kanser oluĸumunda potansiyel terapºtik sonu-larē olan genler ve yolaklarēn karakterizasyonu sēnērlē kalmēĸtēr. Bu boĸluĝu doldurmak i-in laboratuvarēmēz, birka- MPM h¿cre hattēnda genom -apēnda CRISPR/Cas9 taramasē temelinde molek¿ler -alēĸmalar y¿r¿tm¿ĸt¿r. Bu yaklaĸēm ile MPM kanser oluĸumunda kritik bir rol oynayan birka- aday gen belirledik. Kanser h¿cresi saĝ kalēmē ile iliĸkilendirilen bu genlerden biri, otofaji iliĸkili 9A (ATG9A) genidir. ATG9A'nēn MPM'deki rol¿n¿ a-ēklēĝa kavuĸturmak i-in CRISPR/Cas9 teknolojisini kullanarak MPM h¿crelerinde *ATG9A* genini susturduk. ¢alēĸmalarēmēz, *ATG9A* geninin t¿kenmesinin h¿cresel -oĝalma ¿zerinde dramatik bir azalmaya neden olduĝunu gºstermektedir. ¥nemli bir ĸekilde, gºzlemlenen fenotipler *ATG9A* aĸērē ifadesi ile kurtarēlmēĸtēr. Ayrēca, bu fenotipik deĝiĸiklikler reaktif oksijen t¿rleri (ROS) tarafēndan tetiklenen DNA hasarē tarafēndan ind¿klenen h¿cresel yaĸlanma ve apoptoz ile birlikte gelmektedir. *ATG9A* t¿kenen h¿crelerin t¿m genome transkriptomik analizi, h¿cresel yaĸlanma ve apoptoz yollarē ile iliĸkili gen k¿melerini ortaya -ēkardē. Son olarak, araĸtērmamēz, ATG9A'nēn kanonik ve lipid taĸēma, mitofaji gibi non-kanonik iĸlevlerinin, MPM h¿crelerinin saĝ kalēmēnda ºnemli bir rol oynadēĝēnē vurgulamaktadēr. Bu yeni bulgular, MPM patogenezi hakkēnda daha iyi bir anlayēĸ saĝlamakta ve bu zorlu hastalēk i-in ATG9A'yē hedefleyen potansiyel terapºtik stratejilere deĝerli bilgiler sunmaktadēr.

Anahtar Kelimeler: Malign Plevral Mezotelyoma, ATG9A, Otofaji, CRISPR/Cas9

1. AIM OF THE STUDY

MPM represents a highly aggressive and lethal cancer, accounting for approximately 26,000 deaths globally in 2020 (1). Despite the current therapeutic strategies, long-term survival remains elusive, necessitating the urgent development of more effective treatment approaches. The overall incidence of MPM demonstrates the imperative need for better therapies (2). To address this, our laboratory has previously performed a genome-wide CRISPR/Cas9 negative selection screening to identify genes and/or gene families that potentially contribute to MPM carcinogenesis (1). Notably, our analysis revealed several genes demonstrating statistically significant reductions specifically in H2052 and H2452 MPM cell lines compared to the non-tumorigenic MeT-5A cell line. Critically, the *ATG9A* gene emerged as a candidate associated with MPM cell survival. *The ATG9A* gene has a vital role in the initiation of the autophagy (3-5). Surprisingly, there is a dearth of literature elucidating the impact of ATG9A on survival in MPM or other cancers. Given this knowledge gap and the intriguing results from our CRISPR/Cas9 screening, our research hypothesis posits that the *ATG9A* gene plays a crucial role in MPM development. Consequently, the primary objective of this thesis work is to investigate the vital role of the *ATG9A* gene in MPM and elucidate the causal underlying molecular mechanisms through comprehensive experiments conducted on different cell lines *in vitro*.

2. INTRODUCTION

2.1. Malignant Pleural Mesothelioma

Malignant pleural mesothelioma occurs in the mesothelial cells of the pleural surface lining the chest wall and lung. (6). Despite its rarity, MPM is the most prevalent type of all mesotheliomas (7). According to GLOBOCAN 2020 results, the global incidence of new cases and deaths due to MPM is estimated at nearly 30,000 and 26,000, respectively (6). Males have a higher susceptibility to MPM than females (male-to-female ratio=5:1), and the risk of developing this cancer rises with age. In the United States, the mean age at diagnosis is 73 years, while the range is 45 to 85 years (8).

Mesotheliomas are classified into three types based on their cellular structure, namely epithelioid, biphasic, and sarcomatoid subtypes (Figure 1). Histological categorization relies on the morphological characteristics of tumor cells. Among these subtypes, epithelioid MPM represents the most prevalent form, although the incidence rates of each subtype may vary depending on the specific research population and specimen employed (9). Overall, epithelioid, biphasic, and sarcomatoid subtypes have prevalence rates of 61.5%, 22%, and 16.4%, respectively. The epithelioid subtype has the most favorable prognosis (10). Both surgery and chemotherapy have been found to be beneficial for patients with epithelioid MPM. Conversely, the median overall survival rate for patients with sarcomatoid tumors is the lowest among the three subtypes. Biphasic mesotheliomas are composed of both epithelioid and sarcomatoid cells (11).

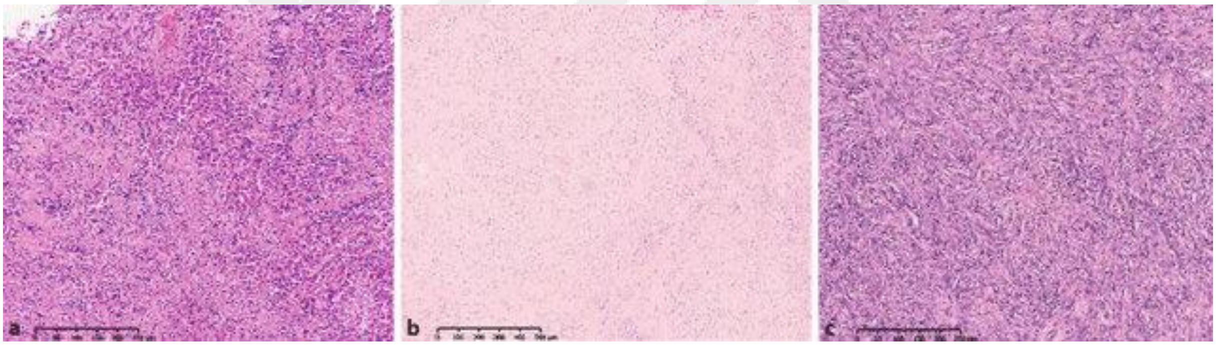

Figure 1: Three histological subtypes of MPM; A) epithelioid, B) biphasic and C) sarcomatoid (adopted from Verma et al. (10)).

2.1.1. Epidemiology of MPM

MPM derives from the neoplastic mesothelial transformation of the parietal pleura. Notably, exposure to asbestos fibers represents a major risk factor, accounting for 70-90% of all MPM cases (12,13). The consequences of asbestos exposure manifest over an extended period, with a significant latency of 10-40 years before MPM diagnosis (14). Even though the exact mechanisms by asbestos induced mesothelioma remain incompletely understood, various pathways have been implicated in this context. These include the generation of reactive oxygen species, direct cytotoxicity, chronic inflammation, kinase-mediated signaling, and dysregulation of growth factors and cytokine (15,16). Concomitantly, widespread loss of heterozygosity is observed in some cases, potentially stemming from direct spindle damage caused by asbestos fibers. However, these mechanisms overlay and more than one pathway is required to fully explain the malignant transformation (2)**.**

As previously mentioned, asbestos fibers exert their impact on mesothelial cells through ROS generation, thereby leading to both epigenetic and somatic genetic alterations. For example, elevated ROS levels have been associated with DNA methylation alterations. Furthermore, asbestos fibers can incite mutagenesis at the chromosomal and gene levels, leading to tumorigenesis (17). Notably, such mutagenesis patterns frequently coincide with modifications in DNA repair genes. In addition to mutagenesis, asbestos fibers have the capacity to disrupt mitosis, perturb chromosome structure, and interfere with mesothelial cell function, all of which are key steps in the development of asbestos-induced mesothelioma (18,19) (Figure 2). Subsequently, inflammatory cytokines such as, platelet-derived growth factor, vascular endothelial growth factor (VEGF) and tumor growth factor-B can promote tumor formation in mesothelial cells when exposed to asbestos (20).

Although many routes have been linked to the pathophysiology of MPM caused by asbestos, high-risk individuals exposed to occupational asbestos have only a 5% chance of acquiring this malignancy. (21). Non-asbestos mineral fibers, chronic pleural inflammation, and therapeutic radiation are additional causes of mesothelioma. (22). Currently, a molecular signature capable of differentiating between these various etiologies, except for germline mutations, has yet to be elucidated (12).

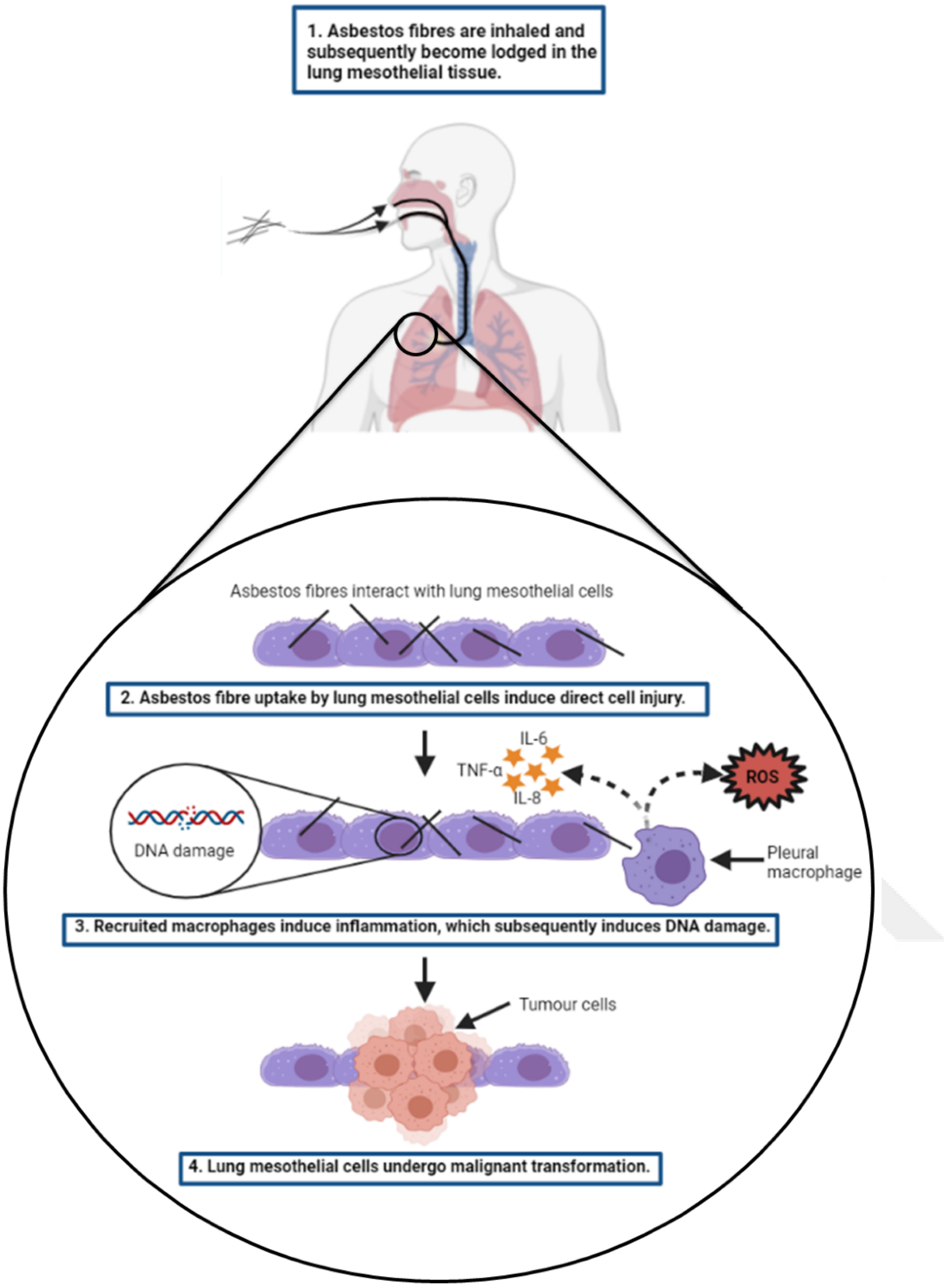

Figure 2: Asbestos-induced MPM (adopted from Johnson et al. (22))

2.1.2. Genomics of MPM

Continuous acquisition of genetic abnormalities that aid in the development of cancerous cells, their growth, and invasion is a fundamental mechanism of tumorigenesis. In the past 20 years, extensive genomic landscape studies have contributed significantly to our understanding of the biology of MPM (23ï 25). Recurring mutations in various regions of the genome have been identified, with a majority being loss of function alterations caused by copy number alterations and point mutations. Unlike other cancers that commonly have oncogenic gain of function alterations, in carcinogenesis of MPM more frequently involves genomic losses. Previous research has demonstrated that MPM frequently involves deletions in the chromosome regions 1p, 3p, 6q, 9p, 13q, 15q, and 22q. The three tumor suppressor genes involved in restricting malignant transformationð NF2, BAP1, and CDKN2A ð have inactivating mutations most frequently observed in these areas. Over 50 percent of the tumors in MPM have BAP1 mutations, making it one of the most frequently occurring genes. (23ï 25). Nonsynonymous somatic mutations, splice changes, gene fusions, and changes in copy number are the most common factors in the loss of function of the BAP1 gene (25). Homozygous deletions of the CDKN2A locus, specifically 9p21, are also frequent in MPM. The whole genetic loss of INK4 locus, includes CDKN2A and CDKN2B, is less common but also observed in MPM (24). Another prevalent mutation in MPM is the inactivation of the NF2 gene, which affects over half of the tumors. This is linked to focal deletions of the 22q12 gene and homozygous chromosomal loss. (23).

So far, several regions of the MPM genome have been found to have gained chromosomes, including 1q, 5p, 7p, 8q, and 17q. It's interesting to note that the TERT gene, which has hotspot promoter mutations and copy number gains, is the first oncogenic gain of function modification that is frequently discovered in MPM, occurring in roughly 10-15% of all cancer types (26,27). Recently, novel copy number gains in oncogenes with recognized oncogenic functions in other malignancies, like CD79B and MDM4, have been discovered in MPM by low-pass whole genome sequencing. These oncogenes may make appealing targets for MPM therapy. Recurrent gains in RPTOR, a gene with established oncogenic activities in colorectal cancer, were also found (26,28).

2.1.3. Treatment of MPM

The prevailing approach for managing MPM involves a combination of surgery and chemotherapy. Notably, radiation therapy is not routinely used, except in a specific subgroup of patients characterized by overall favorable health and good lung and kidney function (29,30). However, most patients are ineligible for surgical intervention upon initial diagnosis, and thus receive only palliative chemotherapy. The standard treatment regimen for MPM entails the administration of cisplatin and pemetrexed, which has demonstrated efficacy in prolonging both overall and progression-free survival. In cases who are unable to receive cisplatin, carboplatin-based regimens are a reasonable alternative (31,32). Recently, a phase 3 trial found that adding bevacizumab to the cisplatin/pemetrexed combination could further increase overall survival, and this may be considered for patients eligible for triplet therapy. Furthermore, in 2020, the FDA approved a new treatment option for unresectable MPM using a combination of nivolumab and ipilimumab, which significantly extended overall survival compared to the cisplatin/pemetrexed doublet (33). Currently, researchers are actively investigating various targeted treatment approaches for MPM to develop a comprehensive and effective treatment strategy (34). These studies involve the use of small chemical inhibitors targeting specific molecules like PI3K/mTOR (LY3023414) and aurora kinase A (alisertib). Monoclonal antibody-drug combinations that target mesothelin, such as anetumab, ravtansine and BMS-986148, as well as monoclonal antibodies targeting immune control points like pembrolizumab, avelumab, and tremelimumab, are also being studied (35).

2.2. Functional Studies

Discovering the links between genetic abnormalities and the visible symptoms of diseases is the goal of functional genomics. The objective is to apply these discoveries in clinical settings in a practical way. Researchers have been able to find novel mutations and alterations in gene expression in cancer thanks to the development of large-scale genomic and transcriptome sequencing technology (1). Researchers can globally define the intricate interactions between genotype and phenotype by combining "gene-by-gene" low-throughput investigations with high-throughput techniques like RNAi and CRISPR. Although there are not much functional genomics research in MPM, the literature that is out there shows that many genetic modifications that have an impact on vital biological processes including transcription, signal transduction, cell division, and migration have functional importance. (1,34). Employing the CRISPR/Cas9 system enables the identification of genes implicated in specific biological processes. This approach involves designing a guide RNA (gRNA) that targets a specific genomic region of interest and the Cas9 enzyme, which serves as a molecular scissor that cleaves the DNA at the targeted location (36). By doing so, the CRISPR/Cas9 system facilitates the knockout of the target gene, leading to its functional loss. This allows researchers to investigate the impact of gene loss-of-function on cellular or physiological processes of interest (37). CRISPR/Cas9 screening is often performed on a large scale, testing multiple genes simultaneously in a systematic manner. This approach can help to identify key genes and pathways involved in specific diseases or cellular processes, enabling researchers to gain a more understanding of the underlying biology and potentially identify new therapeutic targets (38,39).

2.3. Autophagy

More than four decades ago, Christian de Duve introduced the term "autophagy," which originates from the Greek word for "self-eating," to describe a cellular process that was not well understood at the time (40). Autophagy is an intracellular process that involves breaking down proteins and/or damaged organelles due to folding errors. This degradation process is usually triggered by hunger or other stressors and is non-selective in nature. However, even under conditions of nutrient abundance, there is a constitutive or basic form of autophagy that occurs (41). Autophagy is a complicated process that requires a large regulatory mechanism that is essential in both pathological and physiological circumstances. Numerous studies have demonstrated that autophagy is closely linked to a number of illnesses, including aging, malignant tumors, and neuropathy (42). Macro-autophagy, micro-autophagy, and chaperone-mediated autophagy (CMA) are the three main subtypes of autophagy (Figure 3). Large structures can be ingested either selectively or randomly via macro- and micro-autophagy. An autophagosome, a double membrane-bound vesicle that transports cytoplasmic cargo to the lysosome during macro-autophagy, combines with the lysosome to create an autolysosome (40). Micro-autophagy, on the other hand, involves the lysosome directly absorbing cytosolic components via invagination of the lysosomal membrane. With the aid of chaperone proteins like Hsc-70, specific proteins are transported across the lysosomal membrane in CMA. The lysosomal membrane receptors identify these chaperone proteins, which causes the targeted proteins to unfold and degrade (43).

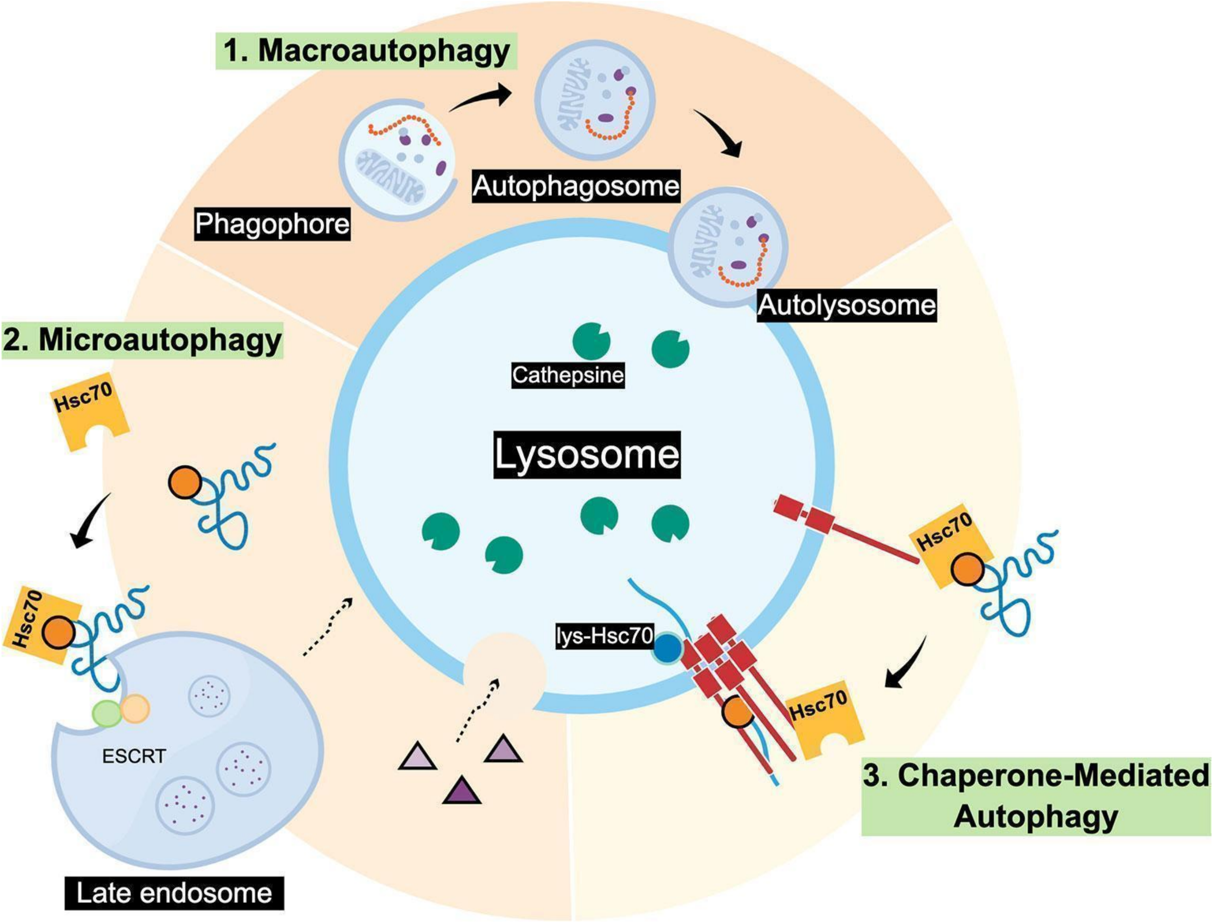

Figure 3: Autophagy is composed of three main subjects: Macroautophagy, Microautophagy and Chaperone-Mediated Autophagy (adopted from Keller et al. (44)).

Generally, autophagy refers to macroautophagy in many articles. In detail, macroautophagy begins with the creation of an isolating membrane (known as phagophore), which engulfs the cytoplasmic material, including organelles and/or cytosol (45). The autophagosome is created by the elongation and fusion of the phagophore membrane. Phagophore and autophagy related proteins (ATG) are used to build the autophagosome at the pre-autophagosomal structure (PAS) (46). The autophagic body/autolysosome is created when the autophagosome joins forces with the vacuole in yeast cells or the lysosome in mammalian cells. Vacuolar/lysosomal hydrolases degrade the luminal substance and internal membrane of the autophagic body/autolysosome. The resultant macromolecules are then recycled in the cytosol after being liberated by permeases (47) (Figure 4).

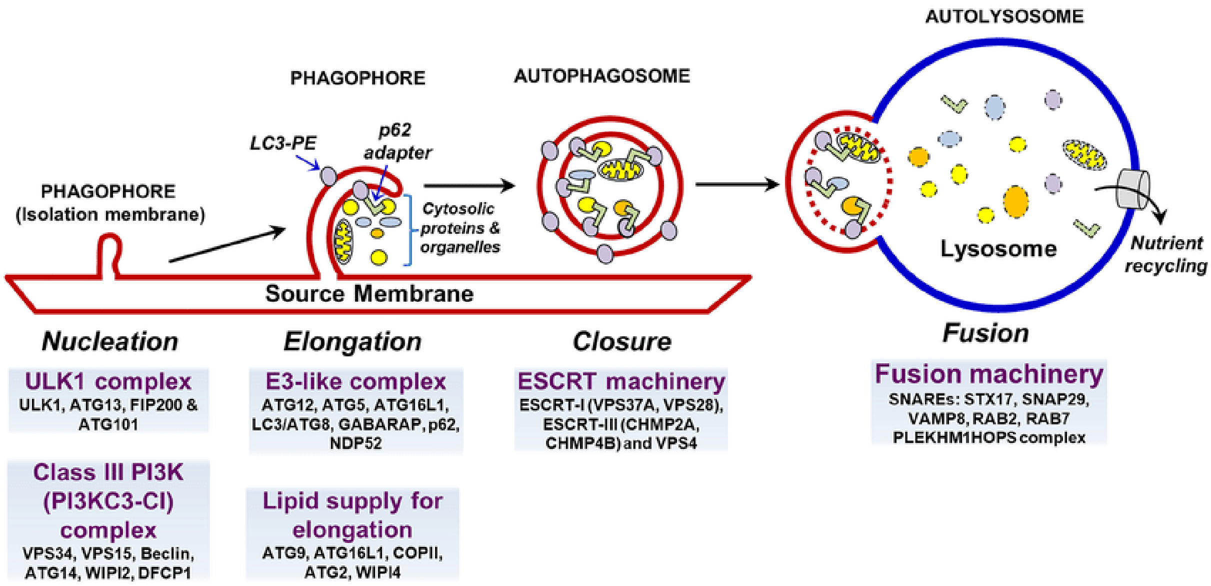

Figure 4: Mechanism of Macroautophagy (adopted from Kliniosky et al. (48)).

2.4. Autophagy Related 9A (ATG9A)

For a while now, there has been a mystery surrounding how autophagosomes are formed, particularly during the step of membrane expansion. In the case of budding yeast, approximately 20 ATG proteins play a role in formation of autophagosome. When the yeast is starved, these core ATG proteins come together to form the PAS via liquid-liquid phase separation (3). This PAS acts as the region for autophagosome formation. Among the core ATG proteins, ATG9 is the only one that is a transmembrane protein. Generally, it is found in the trans golgi network, endosomes, and small vesicles. ATG9 is found in yeast and C. elegans as a single protein (ATG-9) and as two paralogs (ATG9A and ATG9B) in humans. ATG9B is only expressed in the placenta and neuroendocrine cells, whereas ATG9A is present in all organs (49). ATG9A consists of 16 exons and 839 amino acids. The structure of ATG9A has been examined by new studies using cryo-electron microscopy (EM). The investigations showed that ATG9A is a homotrimer protein with domain switching, where each protomer contributes two -helices that partially penetrate the membrane and four -helices that are transmembrane (50). The studies also showed that ATG9A contains a network of internal cavities, which may facilitate trans-bilayer phospholipid transport (51) (Figure 5).

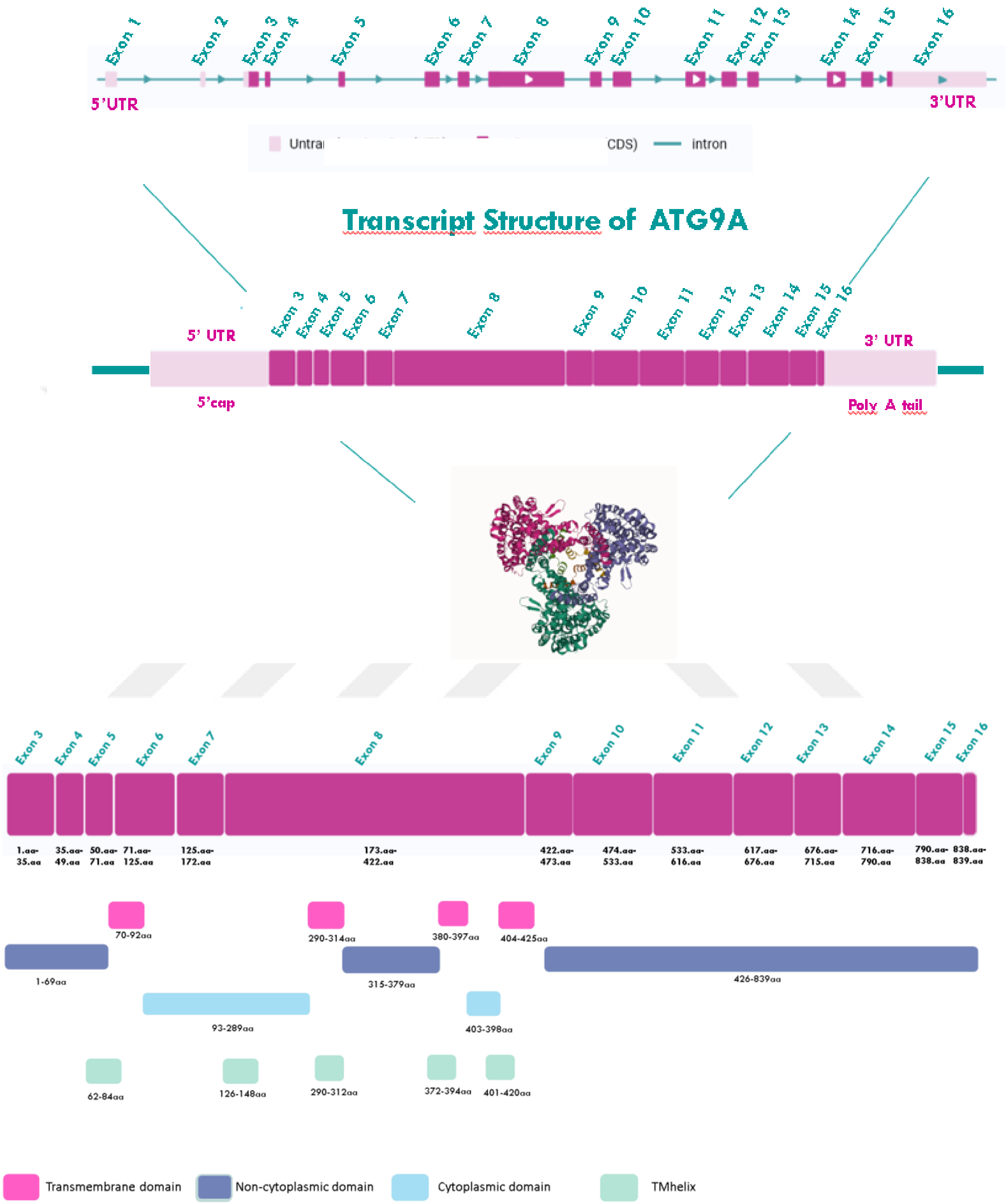

Figure 5: Structure of the ATG9A. (Created with BioRender.com)

Biochemical assays conducted *in vitro* showed that both yeast Atg9 and human ATG9A act as scramblases. When focused on this specific function, ATG9A vesicles separated from the Golgi apparatus are transported to the PAS and serve as an initial membrane source for the isolation membrane (IM) (3,4). After the original IM is created, ATG9A, ATG2, and ATG18 are moved to the expanding edge of the IM and establish a contact site with the ER exit site (ERES). ATG2 is used to take phospholipids from the ER and give these lipids to the cytoplasmic leaflet of the IM. ATG9A takes lipids from the ATG2 and places the lipids to the inner and outer membrane of the phagophore. This function is called as scramblase activity of ATG9A (3) (Figure 6).

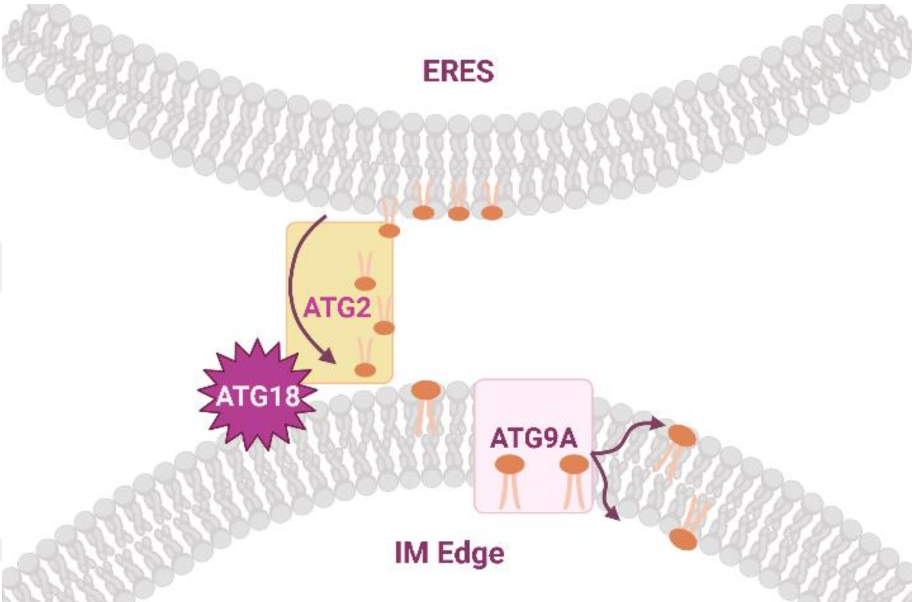

Figure 6: ATG9A has a scramblase function in macroautophagy. Created in BioRender.

Scramblase activity is the known canonical function of ATG9A. As I mentioned above, the ATG9A protein was discovered in the 2000s thanks to this function. Especially after 2020, the functions of ATG9A that we can call non-canonical have emerged. The first found non-canonical function of ATG9A was to provide initiation of mitophagy with the OPTN protein (52). In addition to this, some of the ATG9A proteins in the cell are found in the plasma membrane, although the ratio is small. It has been reported in the literature that it is responsible for protecting the plasma membrane from incidental permeabilization (51). Finally, it turned out that ATG9A transports lipids not only for autophagosome formation but also from lipid droplets to mitochondria where they participate in mitochondrial respiration (53). In addition to the important duties I mentioned, ATG9A has a relationship with cancer. However, this association has so far been observed in a small number of cancers. For example, when *ATG9A* is silenced, it has been observed that triple negative breast cancer and hepatocellular cancer lose their aggressive phenotype.

3. MATERIALS AND METHODS

3.1. Type of the Research

This research study is experimental.

3.2. Place and Time of Research

This study was conducted at the Functional Cancer Genomics Laboratory (also known as Senturk Lab) in the Izmir Biomedicine and Genome Center between September 2020 and June 2023.

3.3. Research Material

3.3.1. Cell Lines

H2052 and H2452 malignant pleural mesothelioma cell lines and non-tumorigenic MeT-5A mesothelioma cell line (transformed with SV40 T antigen) were purchased from ATCC (NCI-H2052, Cat. No: CRL5915, NCI-H2452, Cat. No: CRL5946, MeT-5A, Cat. No: CRL-9444). HEK293T human embryonic kidney cell line was taken from Prof. Dr. Nuri ¥zt¿rk (Department of Molecular Biology and Genetics, Gebze Technical University). Cell culture plates, dishes, sterile falcon, serological pipettes, and cryogenic vials were purchased from Sarstedt (N¿mbrecht, Germany), Cornomics Life Sciences (Arizona, United States), and Greiner Bio-One (Kremsm¿nster, Austria). Common consumables used in cell culture studies are listed in Table 1.

Table 1: List of common cell culture consumables.

Name	**Cat. No**	**Vendor**
RPMI	21875034	Gibco
DMEM	41965039	Gibco
FBS	10500064	Gibco
	SV301060.03	Hyclone
	SF101H-500	Serox
Penicilin-Streptomycin	15140122	Gibco
PBS (10X)	70011036	Gibco

	SH30258.01	Hyclone
0.25% Trypsin-EDTA (1X), phenol red	25200-056	Gibco
TrypLE Express (-) Phenol Red	12604013	Gibco
Polybrene (Hexadimethrine bromide)	H9268-5G	Sigma
PEI	23966	Polyscience
Puromycin	ant-pr-1	Invivogen
Syringe Filter (0,22 um)	16532	Sartoriaus
0,45 um PES Membrane Filter	AND2545	Gilson
DMSO	472301	Sigma

3.3.2. Oligonucleotides

The oligonucleotides synthesized by Macrogen company (Seoul, South Korea) were listed in Table 2. gRNAs were designed by using the online CRISPR gRNA design tool; https://chopchop.cbu.uib.no/, yet some of them were retrieved from the Brunello gRNA library (Addgene plasmids #73179, #73179-LV, #73178, #73178-LV). BsmBI recognition sites "CACC" and "AAAC" were appended at the 5ôsites of the forward and reverse oligonucleotides, respectively. To facilitate translation from the U6 promoter, one "G" nucleotide was added after the ñCACCò site of the forward oligonucleotide. Similarly, one "C" was added at the end of the reverse oligonucleotide. As a positive control, the RPA3 gene, responsible for encoding a protein crucial for accurate DNA replication, was employed. Conversely, the negative control consisted of gRen, a gRNA specifically designed to target the Renilla luciferase gene, which is not encoded by the human genome.

Table 2: List of the oligonucleotide sequences.

Name	**Sequence (5'-3')**
gRen_F	CACCGGTAGCGCGGTGTATTATACC
gRen_R	AAACGGTATAATACACCGCGCTACC
gATG9A-1_F	CACCGCCGTTTCCAGAACTACATGG
gATG9A-1_R	AAACCCATGTAGTTCTGGAAACGGC
gATG9A-2_F	CACCGCTTCACATGTATGCTCATCG
gATG9A-2_R	AAACCGATGAGCATACATGTGAAGC
gATG9A-3_F	CACCGTGCCCTTCCGTATTGCACG
gATG9A-3_R	AACCGTGCAATACGGAAGGGCAC

gATG9A-4_F	CACCGCTCAAGGCCGAGTACAAACG
gATG9A-4_R	AAACCGTTTGTACTCGGCCTTGAGC
gTMEM41B-1_F	CACCGGCTCACCACACGACCCCCGT
gTMEM41B-1_R	AAACACGGGGGTCGTGTGGTGAGCC
gTMEM41B-2_F	CACCGTATACTTACTCACTAAGCTG
gTMEM41B-2_R	AAACCAGCTTAGTGAGTAAGTATAC

3.3.3. Plasmids

Plasmids used in this study were listed in Table 3. In addition to the name and the sources of the plasmids, the map of the plasmids with restriction sites is also shown as figures.

Table 3: List of the plasmid used in this study.

Name	**Source**
pECPV (pEFS-Cas9-P2A-Venus)	Senturk, S. *et al.*, 2017
pLentiCRISPR v2	Addgene Plasmid #52961
pMD2.G	Addgene Plasmid #12259
pSPAX2	Addgene Plasmid #12260
pLP/ VSVG	Invitrogen #K497500
pCL-Eco	Lowe, S. *et al.*, 2015
mtKeima-Red-Mito-7	Addgene Plasmid #56018
pMXs-puro-RFP-ATG9A	Addgene Plasmid #60609

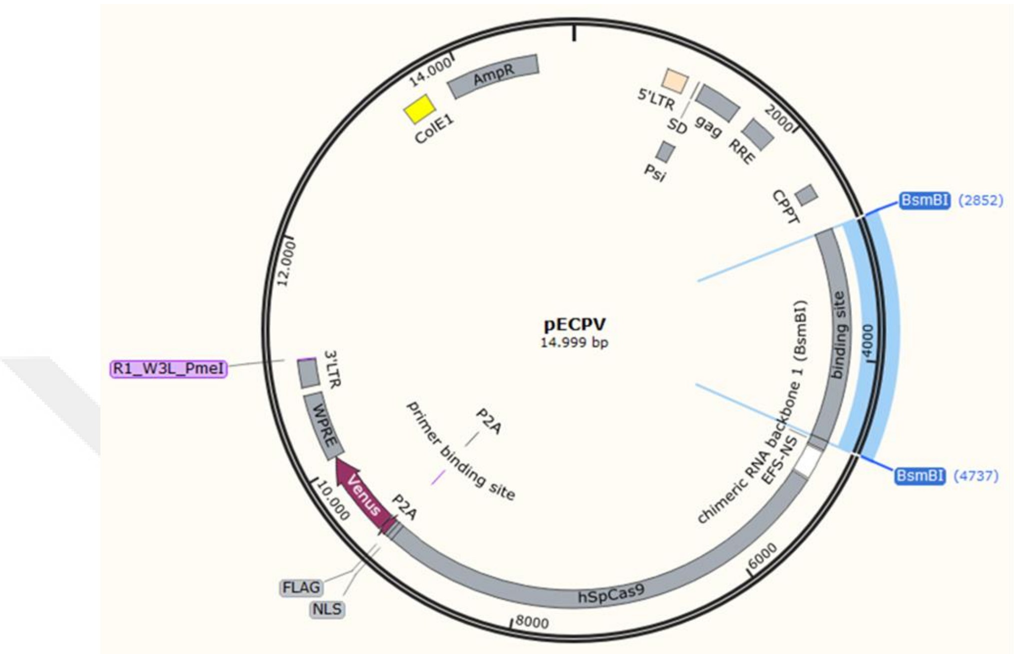

Figure 7: pECPV plasmid map (54).

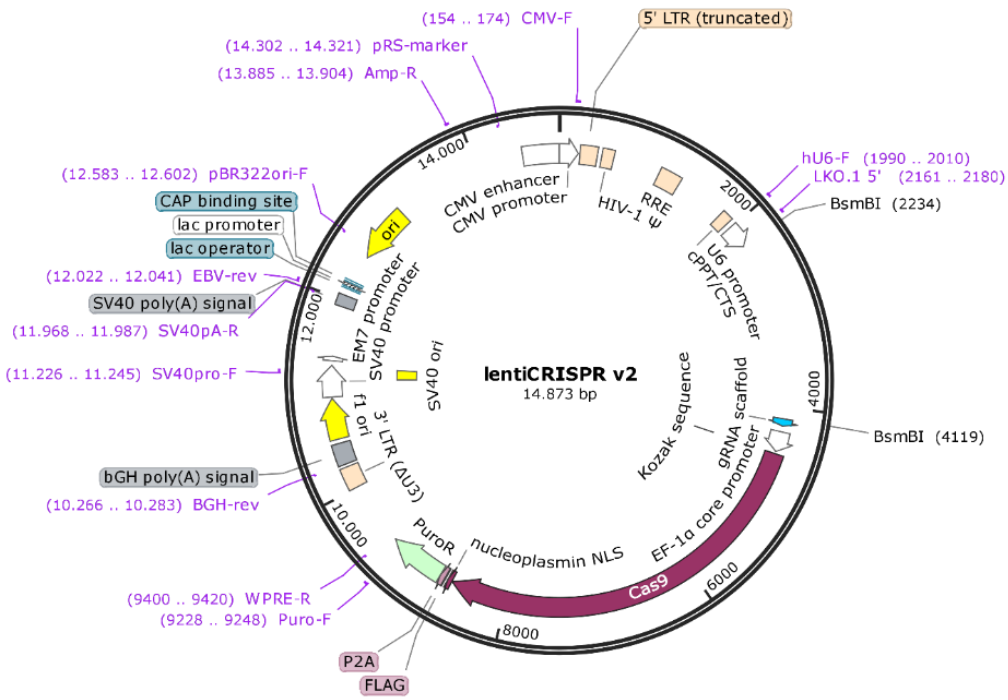

Figure 8: pLentiCRISPR v2 plasmid map.

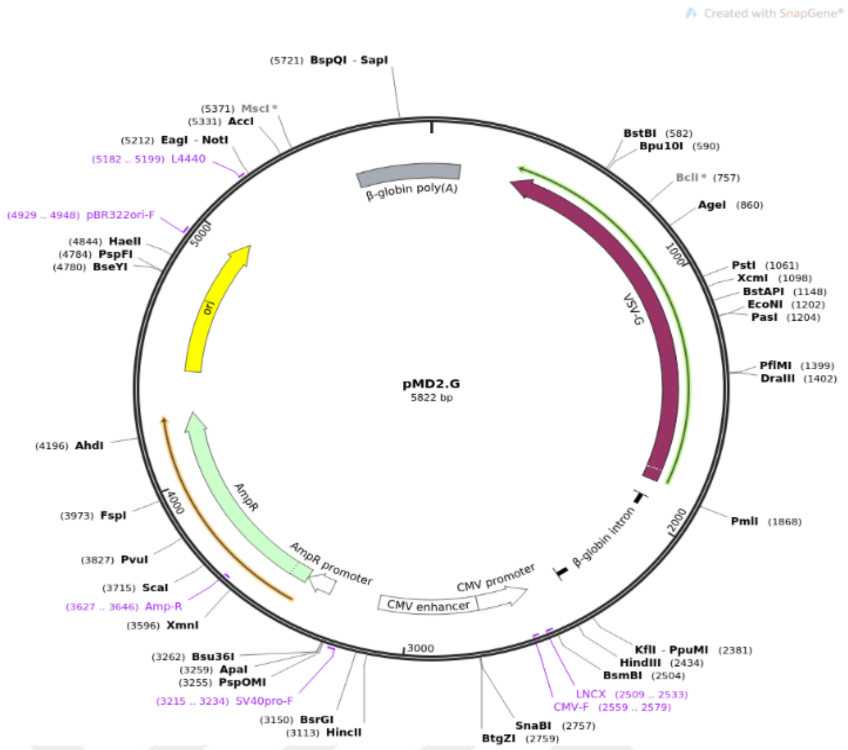

Figure 9: pMD2.G plasmid map.

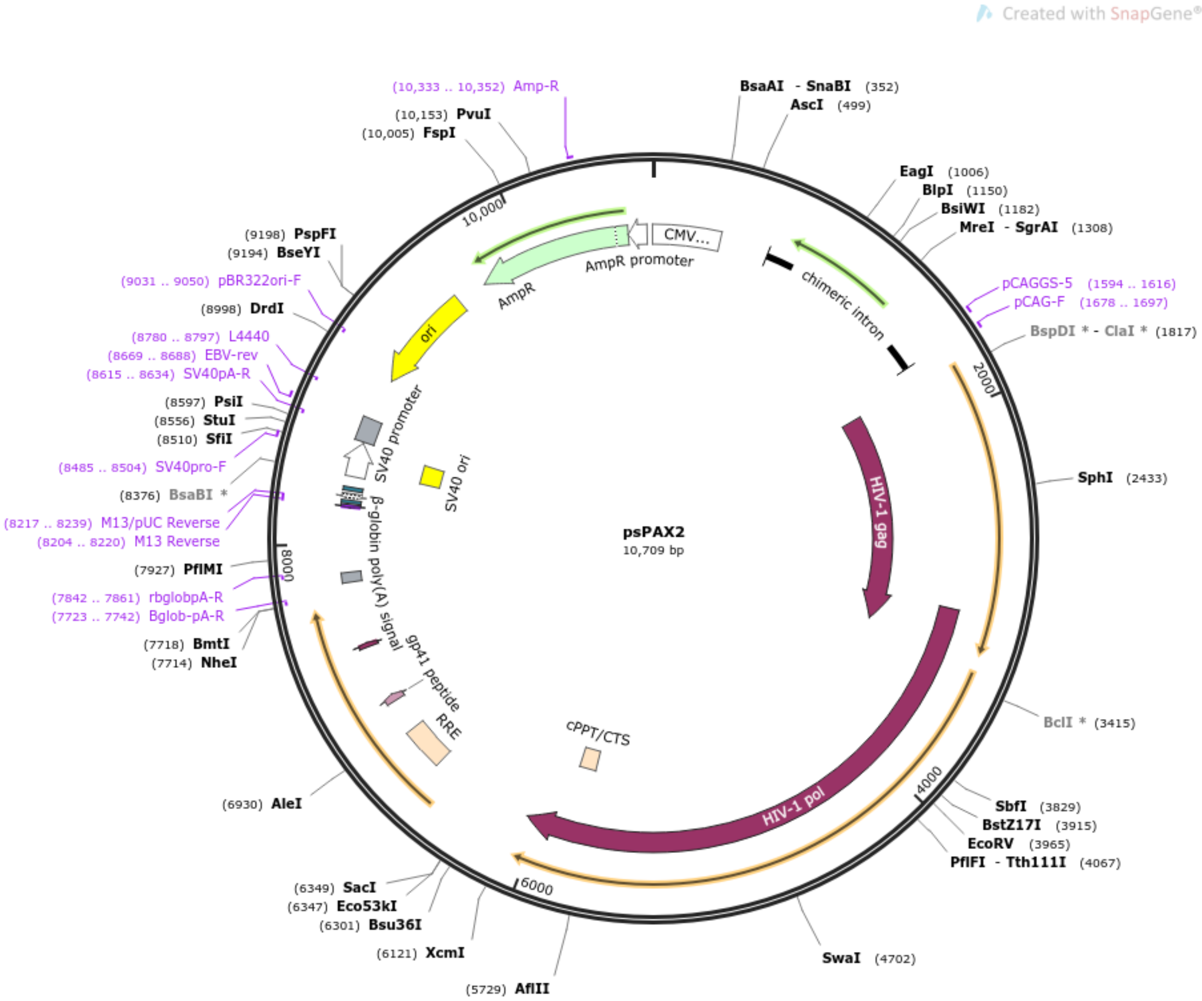

Figure 10: psPAX2 plasmid map.

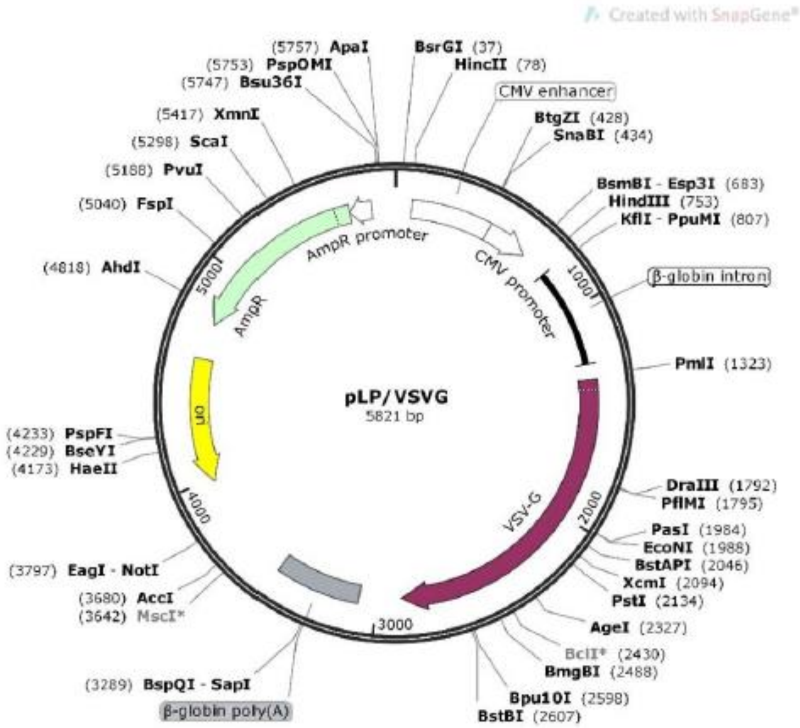

Figure 11: pLP/VSVG plasmid map.

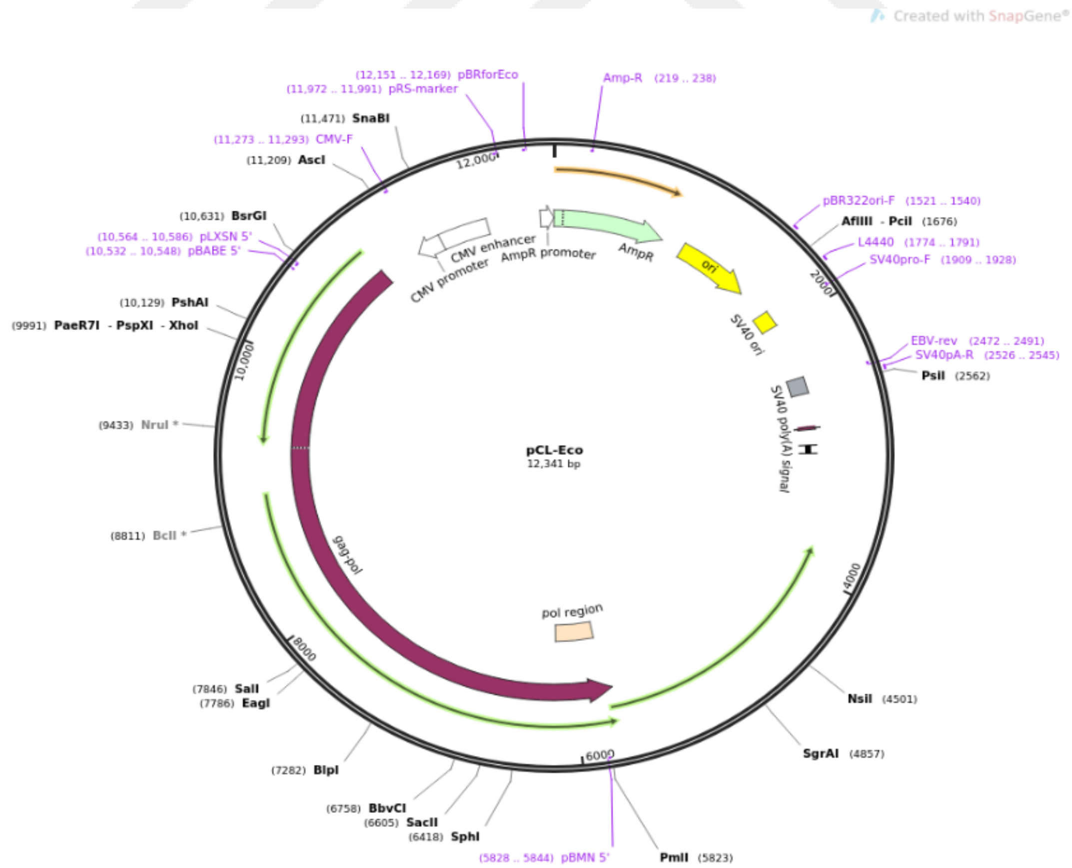

Figure 12: pCL-Eco plasmid map.

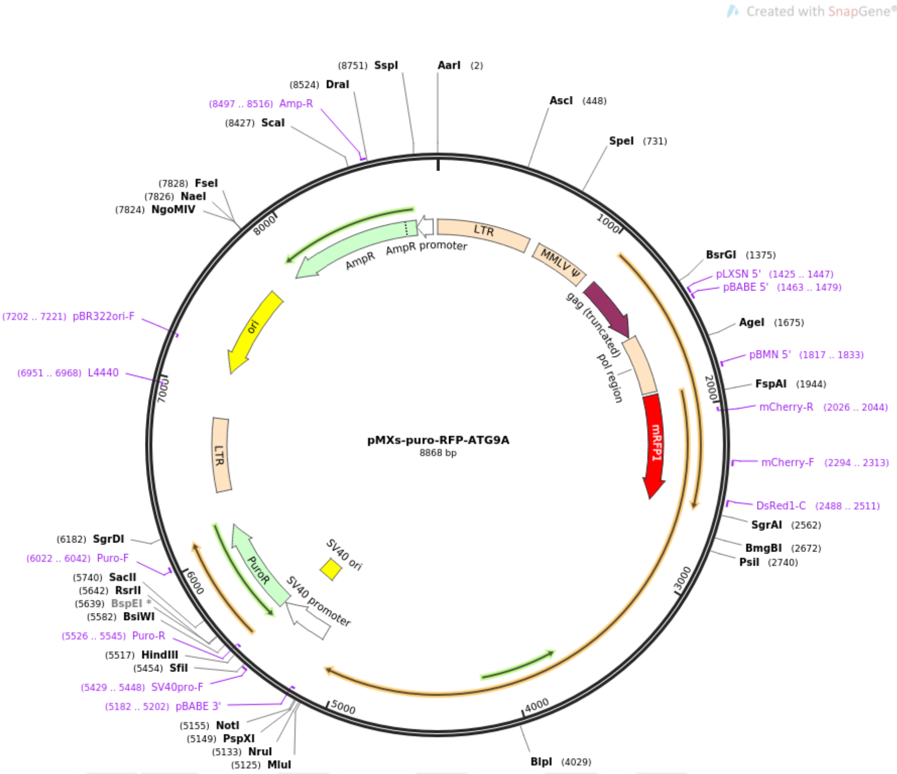

Figure 13: pMXs-puro-RFP-ATG9A plasmid map.

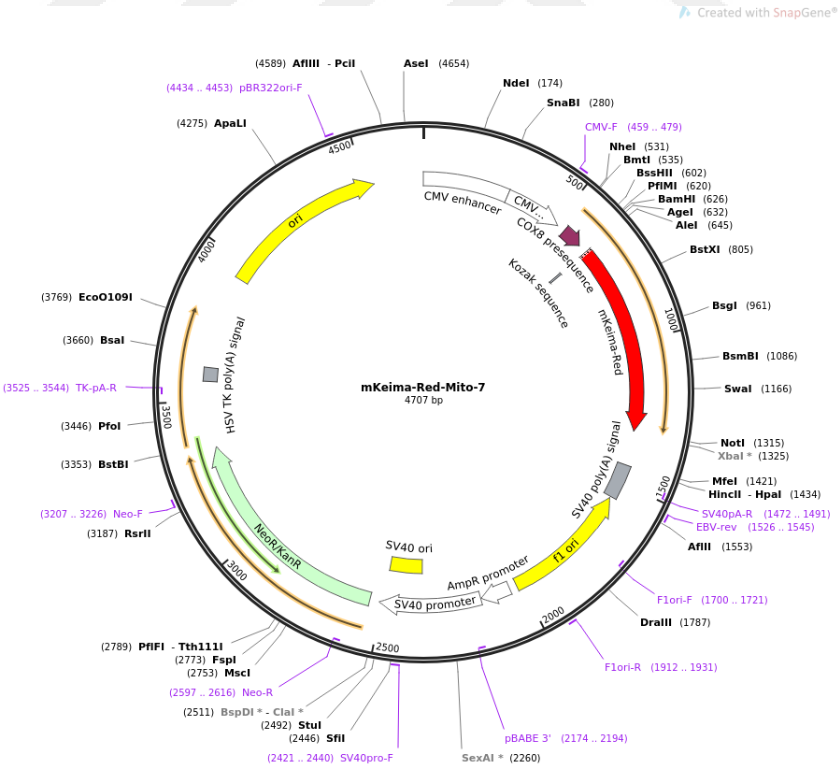

Figure 14: mKeima-Red-Mito-7 plasmid map.

3.3.4. PCR Reagents

Direct PCR of intact bacteria (colony PCR), quantitative reverse transcription PCR (qRT-PCR) and cDNA synthesis reagents are listed in Table 4. gATG9A-1_R, gATG9A-2_R, gATG9A-3_R, gATG9A-4_R, gTMEM41B-1_R, gTMEM41B-2_R and hU6_F (5′ GAGGGCCTATTTCCCATGATT -3′) were used as primers for the colony PCR. Nucleotide sequences of the qRT-PCR primer pairs are shown in Table 5.

Table 4: List of the PCR and cDNA synthesis reagents.

Name	Cat. No	Vendor
iScriptÊ cDNA Synthesis Kit	1708891	Bio-Rad
BlasTaq 2X qPCR MasterMix	G891	Abmgood
dNTP Solution mix (10 mM each dNTP)	N0447S	NEB
Dream Taq Hot Start DNA Polymerase	EP1701	ThermoScientific
10X Dream Taq Buffer	B65	ThermoScientific
MicroAmp Fast 96 well Reaction Plate	4346906	Applied Biosystems

Table 5: List of the qRT-PCR primers.

Gene	Forward	Reverse
ATG9A	GTCAGCTGCGTGGACTATGA (20)	GACTTGAGCAGGCAAAAAGG (20)
NOX4	TGGCTGCCCATCTGGTGAATG (21)	CAGCAGCCCTCCTGAAACATGC (22)
NOX1	GTCTGCTCTCTGCTTGAAT (19)	ATGAGATAGGCTGGAGAG (18)
NQO1	CCCTGCGAACTTTCAGTATCC (21)	CTTTCAGAATGGCAGGGACTC (21)

3.3.5. Molecular Cloning Experiments

Buffers and enzymes used in the molecular cloning experiments are listed in Table 6.

Table 6: List of consumables used in molecular cloning experiments.

Name	Cat. No	Vendor
CutSmart Buffer	B7204S	NEB

FastDigest BsmBI	FD0454	Thermo Scientific
Fast AP (Alkalyne phosphatase)	EF0651	Thermo Scientific
10X FastDigest Buffer		Thermo Scientific
10X T4 ligation buffer	B0202L	NEB
T4 Polynucleotide Kinase (3' phosphate minus)	M0236L	NEB
T4 DNA ligase	M0202L	NEB
EcoRI-HF	R3101S	NEB

3.3.6. Reagents Used in Bacterial Experiments

One ShotÊ Stbl3Ê Chemically Competent Cells (ThermoFisher Scientific; Cat. No: 737303) was used in this study. Chemicals used in bacterial experiments are listed in Table 7. Recipes of these chemicals are also listed in Table 8.

Table 7: List of the chemicals used in bacterial experiments.

Name	**Cat. No**	**Vendor**
Ampicillin	A0166	Sigma
Yeast Extract	MB16401	Nzytech
LB Broth with Agar	L2897	Sigma
Tryptone	1553.03	AppliChem
NaCl	M106404.1000	Merck

Table 8: Recipes of the chemicals.

Reagents	**Recipe**
Luria Bertani (LB) Medium	10 g NaCl
	5 g yeast extract
	10 g tryptone
	in 1 L ddH_2O
Ampicillin Stock (100 mg/mL)	1000 mg ampicillin
	in 10 mL ddH_2O

3.3.7. Western Blot Reagents

Cells were lysed with modified RIPA Buffer. Protein concentrations were quantified with the BCA Assay Kit (ThermoFisher Scientific, Cat. No: 23227). Western blot experiments were carried out with the Mini-PROTEAN Tetra Cell system and Mini

Trans-Blot Module (Bio Rad, Cat. No: 1658029). Buffers used in western blot experiments and their recipes were listed in Table 9. Antibodies are listed in Table 10. Other reagents were listed in Table 11.

Table 9: Buffers and their recipes.

	Recipe	
	Stock concentrations	**taken amounts**
RIPA Buffer	Triton X-100 (10%)	500 ÕL
	Na deoxycholate (10%)	250 ÕL
	SDS (20%)	25 ÕL
	Tris-Cl pH:7,4 (1M)	250 ÕL
	NaCl (5M)	150 ÕL
	EDTA pH:8 (0.5M)	10 ÕL
	EGTA (0.1M)	50 ÕL
	ɓ-glycerolphosphate (0.5M)	100 ÕL
	NaF (0.5M)	100 ÕL
	PMSF (0.1M)	50 ÕL
	Na Vanadate (0.1M)	100 ÕL
	Leupeptin (5mg/mL)	10 ÕL
	Aprotinin (5mg/mL)	10 ÕL
	Pepstatin (1mg/mL)	50 ÕL
	dH2O to final volume	
Main Gel Buffer	Tris	72.684 g
	10% SDS	16 mL
	ddH_2O	184 mL
5X LaemmLi Sample Loading Buffer	Tris	321.5 mM
	SDS	10%
	Glycerol	25%
	Bromophenol blue	0.03%

	ƀ-Mercaptoethanol	0.50%
	ddH$_2$O to finall volume	
10X Running Buffer	Tris	250 mM
	Glycine	1.9M
	SDS	1%
10X Transfer Buffer	Tris	250 mM
	Glycine	1.9 M
10X TBS	Tris	24 g
	NaCl	88 g
	ddH$_2$O	1 L
Ponceau S Stain	Ponceau S	0.1 g
	Acetic acid	2.5 mL
	ddH$_2$O	50 mL

Table 10: Antibodies used in this study.

Antibodies	**Cat. No**	**Vendor**	**Working Dilution**
β-Actin (8H10D10) Mouse mAb	3700	Cell Signalling Technology	1:.5000
Anti-Rabbit IgG (H+L) Dylight 800 4X PEG conjugate	5151P	Cell Signalling Technology	1:20000
Anti-mouse IgG (H+l) Dylight 680 conjugate	5470S	Cell Signalling Technology	1:10000
Caspase-3 (D3R6Y) Rabbit mAb	14220	Cell Signalling Technology	1:1000
Cleaved Caspase-3 (Asp175) (5A1E) Rabbit mAb	9664	Cell Signalling Technology	1:1000
PARP Antibody	9542	Cell Signalling Technology	1:1000
Cleaved PARP (Asp214) (D64E10) XPÈ Rabbit mAb	5625	Cell Signalling Technology	1:1000
Atg9A (D4O9D) Rabbit mAb	13509S	Cell Signalling Technology	1:500
Beclin 1 antibody	66665-1-Ig	Proteintech	1:1000
P62 antibody	66184-1-Ig	Proteintech	1:1000
LC3 Rabbit	14600-1-AP	Proteintech	1:1000

Table 11: Other reagents used in western blot experiments.

Name	Cat. No	Vendor
Cell Scraper	70-2180	Biologix
Acetic Acid	21225-2.5L-R	Sigma
APS	1610GR100	BioFroxx
BLUelf Prestained Protein Ladder	PM008/0500	GeneDirex
Bovine Serum Albumin	1126GR100	BioFroxx
ɓ-Mercaptoethanol	8057400250	Merck
Glycine	sc29096A-500g	SantaCruz
Nitrocellulase Membrane (0.2 Õm)	10600004	GE Healthcare
Ponceau S	P3504-10G	Sigma
Protogel Stacking Buffer	EC-893	National Diagnostic
Protogel (Ultra-Pure) 30%	EC-890	National Diagnostic
SDS	8170341000	Merck
Skimmed Milk Powder	70166-500G	Sigma
TEMED	T22500-100	Sigma
TRIS	T1503-1KG	Sigma
Trɨton X-100	t8787-100mL	Sigma
Tween-20	BP337-100	Fisher BioReagents

3.3.8. BrdU Assay

Antibodies and other reagents used in BrdU Assay are shown in Table 12.

Table 12: Consumables used in BrdU Assay.

Name	Cat. No	Vendor
5-Bromo-2'-deoxyuridine	B5002	Sigma
BrdU (Bu20a) Mouse mAb	5292	Cell Signalling Technology
Donkey anti-Mouse IgG Alexa Fluor 488	ab150105	Abcam
Hydrocloric acid fuming 37%	1003172500	Merck
DAPI	1322MG005	Neofroxx
Microscope Cover Glasses 12 mm	111520	Marienfeld

3.3.9. Senescence-Associated β-galactosidase (SA-β-Gal) Assay

Reagents used in SA-ɓ-Gal Assay are listed in Table 13. Recipes of fixative solution and buffers used in this assay are shown in Table 14.

Table 13: Reagents of SA-ɓ-Gal Assay.

Name	**Cat. No**	**Vendor**
Glutaraldehyde Solution	820603.1	Merck
Formaldehyde solution	F1635	Honeywell
Citric Acid Monohydrate	9100461000	Isolab
Sodium phosphate dibasic dihydrate	4272	Sigma
Potassium hexacyanoferrate (II) trihydrate (ferro)	LC-10061.1	Neofroxx
Potassium hexacyanoferrate (III) (ferri)	LC-6423.3	Neofroxx
Sodium Chloride	1064041000	Merck
Magnesium chloride hexahydrate	LC-5041.4	Neofroxx
PBS (1X)	10010-015	Gibco
X-Gal	1168GR001	Neofroxx

Table 14: Recipes of fixative solution and buffers.

Buffer	**Recipe**	
Fixative Solution	25% Glutaraldehyde solution	80 ÕL
	37% Formaldehyde	500 ÕL
	PBS (1X)	9420 ÕL
	ddH_2O	10 mL
200 mM citric acid/Na phosphate buffer	citric acid (0,2 M)	7.37 mL
	sodium phosphate dibasic dihydrate (1 M)	5.052 mL
	dH_2O	40 mL
Staining Solution	200 mM citric acid/Na phosphate buffer	2 mL
	100 mM potassium ferrocyanide	500 ÕL
	100 mM potassium ferricyanide	500 ÕL
	2 M NaCl	750 ÕL
	100 mM $MgCl_2$	750 ÕL
	(1 mg) X-gal in dimethyl formamide	250 ÕL
	dH_2O to final volume	5.8 mL

3.3.10. Comet Assay

Reagents used in Comet Assay are listed in Table 15. Recipes of solutions used in this assay are shown in Table 16. Sodium lauroyl sarcosinate (Sigma, Cat. No: L9150) were kindly gifted by Serap Erkek Laboratory (Izmir Biomedicine and Genome Center).

Table 15: Reagents of Comet Assay.

Name	Cat. No	Vendor
Na_2EDTA	E5134	Sigma
NaOH	1064981000	Merck
Propidium Iodide	81845	Sigma
NaCl	1064041000	Merck
Biomax Agarose	000320PR	Prona

Table 16: Recipes of solutions used in Comet Assay.

Solution	Recipe	
A1 (Alkaline Lysis Solution):	NaCl	1.2M
	Na2EDTA	100mM
	Sodium lauroyl sarcosinate	0.10%
	NaOH (pH > 13)	0.26
	dH_2O to final volume	
A2 (Alkaline Rinse and Electrophoresis Solution):	NaOH	0.03 M
	Na2EDTA	2mM
	dH_2O to final volume	

3.3.11. Other Consumables and Commercial Kits

Consumables and commercial kits used in this study are shown in Table 17.

Table 17: List of Consumables.

Name	Cat. No	Vendor
FITC Annexin V Apoptosis Detection Kit with PI	640914	Biolegend
NucleoSpin Gel and PCR Clean-up	740609.5	MN
Monarch Total RNA Miniprep Kit	T2010S	NEB
EZ-10 Spin Column Plasmid DNA Miniprep Kit	BS614.0612R0C	BioBasic

MatrigelÈ Basement Membrane Matrix, LDEV-free	356234	Corning
Permeable Support for 24-well Plate with 8.0 Õm Transparent PET Membrane, Sterile	353097	Falcon
Gel Loading Dye, Purple (6X) - 4,0 ml	B7024S	NEB
Ultrapure Distiled Water 500 ml	10977-035	Invitrogen
Methanol HPLC Grade	20864320	VWR
Crystal Violet	C6158	Sigma
Thiazoly blue tetrazolium bromide (MTT)	1334GR001	Neofroxx
Absolute Ethanol	9200262500	Isolab
2-Propanol	24137	Sigma
Noble Agar, Ultrapure, Thermo Scientific	J10907-100gr	Alfa Aesar
Rnase A	1263MG050	Neofroxx
1 kb DNA Ladder	N3232S	New England Biolabs
10 ml/cc Steril Enjektºr		Genject
Polystyrene Round Bottom Tube w/cell-strainer cap	352235	Falcon
N-acetyl-L-cysteine (NAC)	A9165	Sigma
AUTODOT	sm1000a	Abcenta
CM-H2DCFDA	C6827	Invitrogen

3.3.12. Machines and Hardware

Machines are listed in Table 18.

Table 18: List of the machines used in this study.

Machine	**Vendor**
pH Meter	HANNA Instruments
Toploader Balance 820 g x 0.01g	Sartorius
MicroCL 17 Microcentrifuge (Ventilated) 230V with Hematocrit rotor	ThermoFisher Scientific
SimpliAmpÊ Thermal Cycler	Applied Biosystems

OwlÊ EasyCastÊ B1A Mini Gel Electrophoresis Systems	ThermoFisher Scientific
microwave oven	Beko
mySPINÊ 6 Mini Benchtop Centrifuge	ThermoFisher Scientific
Vortex Mixer	ThermoFisher Scientific
Hotplate Stirrer Thermolyne	ThermoFisher Scientific
Waterbath	Nuve
Centrifuge 5810R	Eppendorf
Centrifuge MicroCL 17R	ThermoFisher Scientific
Incubator MaxQ 4000	ThermoFisher Scientific
Confocal Microscopy	Zeiss LSM880
ABI 7500 Fast Thermal Cycler	ThermoFisher Scientific
Li-Cor Odyssey Imaging System	Li-Cor
NanoDrop 2000	ThermoFisher Scientific
Multiskan GO Microplate Spectrophotometer	ThermoFisher Scientific
BD LSRFortessaÊ flow cytometer	BD Biosciences
CKX41 Inverted Microscope	Olympus
BX61 Fully Motorized Fluorescence Microscope	Olympus
Gel Doc XR+ System with Image Lab Software	Biorad

3.4. Methods

3.4.1. Cell Culture Methods

MeT-5A non-tumorigenic mesothelial cell line and H2052 and H2452 malignant pleural mesothelioma cell lines were acquired from the American Tissue Culture Collection (ATCC). All cell lines were cultured in Roswell Park Memorial Institute Medium (RPMI 1640, Gibco) supplemented with 10% fetal bovine serum (FBS, Gibco) and 1% penicillin streptomycin (Gibco). HEK293T cells were cultured in high glucose Dulbeccoôs Modified Eagleôs Medium (DMEM) (Gibco) supplemented with 10% FBS and 1% penicillin streptomycin. Cells were maintained at 37ÁC and 5% CO2 culture conditions. The Mycoplasma PCR Detection Kit (G238, ABM) was used on a regular basis to confirm that the cells are negative for contamination.

Subculturing of cells

Cell plates placed in the incubator were taken into cell culture hood. Then, the medium of the cells was discarded by suction. Cells were washed with 1X PBS. After washing, an appropriate amount of TrypLE or trypsin was added on the cells for trypsinization and incubated in 37Ć for 2-5 minutes. Next, cell culture medium was added on the plate and cells were harvested into 15 ml centrifuge tubes with the help of the pipette. Cells were centrifuged at 1600 rpm for 2 min in a tabletop centrifuge. If subculturing was made for maintenance, cells were resuspended by medium and appropriate amounts were separated into another plate. If subculturing was made for experiment, cells were resuspended and 10 εl of the cell-medium mix was taken and loaded into two chambers of hemocytometer to calculate the cell number. After counting, an appropriate amount of cell-medium mix was transferred to specific culture dishes.

Thawing of the cells

One vial of frozen cells was taken out of the freezer at -80Ć or nitrogen tank and placed in a 37Ć water bath to defrost until there was just a small bit of ice remaining. Then, thawed cells were transferred into a 15 ml centrifuge tube with 9 ml of medium and centrifuged for two minutes at 1600 rpm in a tabletop centrifuge. The supernatant was discarded and the cell pellet was resuspended in complete medium and then transferred to the proper cell culture dish.

Cryopreservation

After experiments were done, cells were frozen. Cell plates found in the incubator were taken. Cells were washed with PBS and trypsinized with TrypLE or trypsin. After 2-5 minutes of incubation at 37Ć with TrypLE or trypsin, cells were harvested into 15 ml centrifuge tubes by the addition of medium. Cells were centrifuged at 1600 rpm for 2 min in a tabletop centrifuge. Supernatant was removed and the pellet was resuspended with a freezing medium (20% FBS and 8% DMSO in a particular medium). Cell and freezing medium mix was transferred into the cryovial tube. Cryovial tubes were stable at -80Ć freezer for short-term storage or in liquid nitrogen for long-term storage.

3.4.2. gRNA Vector construction

Four different *ATG9A* gRNA sequences (g1, g2, g3 and g4) and 2 different *TMEM41B* gRNAs (g1 and g2) were cloned into pECPV (49) and pLentiCRISPR v2 plasmids for knockout of the *ATG9A* gene. Firstly, pECPV and pLentiCRISPR v2 plasmids were digested and dephosphorylated. Reaction mixture and conditions are shown in Table 19.

Table 19: Components and conditions of plasmid digestion.

Components	**Amount**
Plasmid	5εg
BsmBI	3εL
FAST AP enzymes	3εL
10X Fast Digest Buffer	6 εL
ddH_2O	to 60 εL
Conditions	
2 hours at 37 ÁC	

Secondly, gRNA oligos (reverse oligos, 100 εM and forward oligos, 100 εM) were phosphorylated and annealed. Reaction mixture and conditions are shown in Table 20. After completion of the reaction, the product was diluted 1/20. The dilution product was used directly in the ligation step.

Table 20: Components and conditions of oligo duplication.

Components	**Volumes**
T4 PNK	0.5 ÕL
10X T4 Ligation Buffer	1 ÕL
Reverse oligo	1 ÕL
Forward oligo	1 ÕL
ddH_2O	6.5 ÕL
Conditions	
37ŚC 30min	
95ŚC 5min	
Ramp down to 25ŚC at 5ŚC/min	

Digested and dephosphorylated plasmids were purified from agarose gel by the NucleoSpin Gel and PCR Clean-up kit. Lastly, digested plasmids and annealed oligos were ligated as shown in Table 21.

Table 21: Components and conditions of ligation.

Components	**Amounts**
Digested plasmid	50 ng
Oligo pair	2 εl
T4 Ligase	0.5 Õl
T4 ligation Buffer	1 Õl
ddH_2O	to 10 εL
Conditions	
2 hours at 25ęC	

3.4.3. Empty Overexpression Plasmid Construction

pMXs-puro-RFP-ATG9A overexpression vector was digested with EcoRI-HF enzyme to excise the *ATG9A* gene and obtain an empty plasmid. Conditions are shown in Table 22.

Table 22: Components and conditions of plasmid digestion.

Components	**Volumes**
Plasmid	1 εg
EcoRI-HF	0.5 Õl
CutSmart Buffer	2 ÕL
ddH_2O	to 20 ÕL
Conditions	
2 hours at 37 ĆC	

Digested product was run on 1.5% agarose gel and the corresponding band was extracted from the gel by the NucleoSpin Gel and PCR Clean-up kit. Digested plasmid was ligated. Reactions and conditions are shown in Table 23.

Table 23: Conditions and components of ligation procedure.

Components	**Amounts**
Digested plasmid	50 ng
T4 Ligase	0.5 Õl

T4 ligation buffer	1 Õl
ddH_2O	to 10 εL
Conditions	
2 hours at 25ȩC	

3.4.4. Transformation

For the transformation of ligated plasmids, Stbl3 competent E.coli strain was used. Total ligated product was transferred into the 50 Õl of Stbl3 competent strain and incubated on ice for 30 minutes. For the heat shock method, the mix was placed in the water bath at 42ȩC for 45-60 seconds then, the mix was immediately incubated on ice for 2 minutes. 1 mL of LB medium was added onto the mix and incubated at 37ȩC for 1 hour for recovery. Mix was centrifuged at 10,000 rpm for 2 minutes. Excess supernatant was removed, and pellet was resuspended in the remaining LB medium. Resuspended pellet was spread on the LB Agar plate containing 100 Õg/ml Ampicillin. Plates were incubated overnight in an incubator at 37ÜC. After 18 hours, 3 colonies were picked to perform colony PCR.

3.4.5. Colony PCR

To test the cloning efficiency, bacteria colony PCR was performed. Three colonies were chosen from an agar plate containing 100 Õg/mL Ampicillin. Using tips, the selected colonies were collected and swirled into a PCR tube. Essentially, the swirling motion was employed to obtain the template for the colony PCR. The tip was then placed in 5 mL of LB medium for an 18-hour incubation at 37ÜC. Other components and conditions of the colony PCR are shown in Table 24.

Table 24: Components and conditions of colony PCR.

Components	**Volumes**	
Taq polymerase	0.1 ÕL	
Taq Buffer (10 X)	2 ÕL	
Reverse primer	0.4 ÕL	
Forward primer	0.4 ÕL	
dNTPs	0.4 ÕL	
ddH_2O	6.7 ÕL	
Conditions		
Initial Denaturation	94ÁC 5 min	1 cycle

Denaturation	94ÁC 30 sec	30 cycles
Annealing	60ÁC 30 sec	
Extension	72ÁC 2 min	
Final extension	72ÁC 5 min	1 cycle

3.4.6. Mini Culture & Midi Culture & Plasmid Isolation

Following the incubation of bacteria in LB medium with ampicillin for 18 hours at 37ŬC on a shaker operating at 225 rpm, the Bio Basic EZ-10 Spin Column Plasmid DNA Miniprep Kit protocol was utilized to isolate the plasmid DNA.

3.4.7. Transfection and Virus Production

For transfection, linear polyethylenimine (PEI 25K) was used. Briefly, 6 εg of DNA and PEI reagent in 1X PBS were mixed and subsequently transfected into the cells. HEK293T cells were used for both lentivirus and retrovirus productions. The helper vectors, psPAX2 and pMD2.G, were used to package the lentivirus. Target vector:psPAX2:pMD2.G were combined in an ideal weight-to-weight ratio of 4:2:1. Helper plasmids pCL-Eco and pLP/VSVG were utilized to produce retroviruses. An optimum 1:1:1 weight-to-weight ratio was used to combine the target vector:pLP/VSVG:pCL-Eco. Generally, a total amount of 6 εg of helper and target plasmid DNA were blended with 1X PBS before adding to the PEI mixture (30 ÕL PEI-170 ÕL PBS for lentiviruses, 120 ÕL PEI-180 ÕL PBS for retroviruses). For lentivirus packaging, HEK293T cells in a 60mm dish were rinsed with 1X PBS and then 2.4 mL of fresh complete DMEM was added. After 25 minutes of incubation, DNA/PEI mix was applied to the cells by dropwise addition. In the case of retrovirus production, 2.4 mL of fresh non-complete DMEM was introduced to the HEK293T cells. After a 6-hour incubation period, the medium was removed and replaced with complete DMEM. In both scenarios, 48 hours after the transfection, the medium containing virus particles was collected and subjected to purification. This was achieved by passing the medium through a 0.45 Õm low protein binding SFCA filter membrane to isolate and purify the viruses.

3.4.8. Viral Infection

Infection was performed by the help of Polybrene to increase the infection efficiency. For lentiviral virus infection, virus containing medium was combined with medium/polybrene (8 Õg/mL) mix in 1:5 ratio. For retroviral virus infection, virus containing medium was combined with medium/polybrene (8 Õg/mL) mix in 1:1 ratio. This mixed solution containing virus was added on the target cells in a 60 mm dish with %50 confluency. After 48h, the medium was removed and rinsed. Cells were transferred to a 100 mm dish and selected with puromycin or sorted according to the GFP signal with FACS. In ATG9A rescue experiment, infection was made twice, 3 days apart.

3.4.9. Cell Sorting

The cell sorting was performed by the iBG Flow Cytometry Facility. Cells were trypsinized and collected in centrifuge tubes. Cells were then centrifuged, and the supernatants were removed. The pellet was resuspended in 1 ml FACS buffer. After that, samples were transferred to FACS tubes with cell strainer caps and placed on ice. Additional FACS tubes containing complete RPMI with 20% FBS and 2% pen/strep were prepared for cell sorting. Sort was performed using the FC-1072 Aria III Sorter.

3.4.10. RNA Isolation

Trypsinized cells were collected in 1.5 ml tubes and centrifuged for 2 minutes at 1600 rpm. The centrifugation step was repeated after the medium was removed and the pellet was washed with 1X PBS. The Monarch Total RNA Miniprep Kit was used to isolate RNA. Isolated RNA concentrations were determined using Nanodrop and diluted to 100 ng/Õl for each sample.

3.4.11. cDNA Synthesis

Isolated RNA was converted to cDNA by iScript cDNA synthesis kit. Samples were diluted 4.2X by nuclease-free water (64 Õl) and stored at -20ęC. Components and conditions of the cDNA synthesis are shown Table 25.

Table 25: Components and conditions of cDNA synthesis.

Components	Volumes
iScript reaction mix (5X)	4 ÕL

iScript reverse transcriptase	1 µL	
RNA template (1ug)	10 µL	
ddH2O	5 µL	
Conditions		
Priming	5 min	25 °C
Reverse Transcription	20 min	46 °C
Reverse Transcriptase Inactivation	1 min	95 °C

3.4.12. Quantitative Real-Time PCR (qRT-PCR)

For quantitative real-time polymerase chain reaction (qRT-PCR) experiments, the Applied Biosystems 7500 Real-Time PCR System was used. The reaction mixture for the qRT-PCR reaction is shown in Table 26 for each sample.

Table 26: Components of qRT-PCR.

Components	**Volumes**
SYBR Green Mastermix (2X)	5 µL
Template cDNA	4.2 µL
Reverse primer (10 µM)	0.4 µL
Forward primer (10 µM)	0.4 µL

The formula for calculating gene expression levels relative to an internal control using Ct values is shown below.

Relative gene expression = $2^{(-\text{delta delta Ct})}$

3.4.13. Western Blot

The cells were harvested by scraping and lysed in modified radioimmunoprecipitation assay (RIPA). After 3 vortex-ice cycles (3 x 10 min), lysates were sonicated for 10 cycles (1 cycle: 30 s off - 30 s on). After 30 minutes of centrifugation (13.000 rpm, + 4 °C), supernatant was collected as protein lysates. Protein concentrations were determined by the Pierce BCA Protein Assay Kit (Thermo Scientific, catalog number 23225). Albumin standards (2000 µg/ml) were prepared by serial dilution with RIPA buffer at the following concentrations: 1000, 500, 250,125, 62.5, 31.25 µg/ml. 2 µl of each sample were added in triplicate to a 96-well plate, beginning with Albumin standards. RIPA lysis buffer was used as a control. Then, 50 εl of a 1:50 (v/v) solution B:solution A mixture was added to each sample, including the blank. The plate was covered with aluminum foil to protect it from light and incubated in 37 C for 30 min. The Multiskan GO Microplate Spectrophotometer was used to measure absorbance at 562 nm at the end of the incubation. After removing the absorbance of blank from all samples, a standard curve was plotted at 562 nm based on the absorbance values of albumin standards at different concentrations. The Varioskan software determined the concentrations of each sample based on the standard curve. Protein concentrations were determined by equating the RIPA lysis buffer with the lowest concentration, and each sample was mixed with 5X laemmli buffer. The samples were then boiled for 5-7 minutes at 95 Ꞓ. Quantified protein lysates (20 Ǭg total) were separated using sodium dodecyl sulfate polyacrylamide gel electrophoresis (SDS-PAGE) on either 8%, 10%, 12% or 15% Tris-Glycine gels. 10 ml SDS-PAGE separating gel recipes are shown in Table 27.

Table 27: Components of SDS separating gel.

Components (for 5 ml)	**6%**	**8%**	**10%**	**12%**	**15%**
Protogel (ml)	1	1,35	1,65	2	2,5
dH_2O (ml)	3.375	3.025	2.725	2.375	1.875
Main gel buffer (ml)	0.625				
10% APS (Ǭl)	25				
TEMED (Ǭl)	5				

After preparing the separating gel according to the recipe, it was loaded between western glasses and polymerized in a flat line with 60% isopropanol. The isopropanol was removed after the gel had solidified, and the western glasses were dried with a napkin. A comb was placed between the western glasses and a stacking gel prepared according to recipe, shown in Table 28.

Table 28: Components of stacking gel.

Components (for 2 ml)	
Protogel (ml)	0.25
ddH_2O (ml)	1.25
Protogel stacking buffer pH:6.8 (ml)	0.5

10% APS (Õl)	12.5
TEMED (Õl)	2.5

The comb was removed after the stacking gel polymerized, and the running system was assembled. After filling the system with 1X running buffer, 20 Õg of each sample was loaded into each well of the gel, beginning with the protein ladder in the first well. The samples were run at 90V for approximately 20-30 minutes before being passed to the separating gel. The voltage was then increased to 120V, and the gel was run until the protein ladder bands were properly separated. Following the running process, the stacking part of the gel was thrown away, and a sandwich system consisting of sponge, filter paper, separating part of the gel, nitrocellulose membrane, filter paper, and sponge, respectively was set. This sandwich was placed in the tank in a 1X transfer buffer. The transfer was completed in 90 minutes at 350 mA. After the transfer was completed, the membrane was stained with Ponceau S to determine whether the transfer was successful.

After wet-transfer, 0.20 Õm nitrocellulose membranes were blocked using 5% skim milk in 1X Tris-Buffered Saline (TBS) for 1h at room temperature. Then, the membrane was rinsed 3 times with 1X TBS-T. Next, membranes were incubated with specific primary antibodies in 1% BSA in 1X TBS-T at appropriate dilutions overnight at 4 C. ATG9A, Cleaved Caspase 3 and Cleaved PARP primary antibodies were incubated overnight at 4ÜC + 2h room temperature. Membranes were incubated with secondary antibodies for 1 h at room temperature. Images were taken using the Odyssey CLx imaging system (LI-COR).

3.4.14. Immunofluorescence Staining

Cells were seeded on coverslips (12mm) in 24-well plates as 24,000 cells/ well as duplicates. After 24 hours, EBSS (1X) was added and incubated for 2 hours on the cells in autophagy-related experiments. EBSS in autophagy experiments or complete medium was removed and cells were fixed with 3.7% formaldehyde in PBS for 10 minutes. After cells were rinsed with PBS three times, cells were incubated with permeabilization solution for 5 minutes on the shaker. Permeabilization solution was prepared as 0.5% Triton X-100 in 1X PBS. For blocking, 5% BSA in 1X PBS was used and cells were blocked for 1 hour at room temperature. The primary antibody was probed for 1 hour at room temperature. The secondary antibody was incubated for 1 hour at room temperature after three 1X PBS washings. DAPI counterstaining was performed for 1 minute. Cells were mounted on cover glass after washing with distilled water. Confocal microscopy (Zeiss LSM880) was used for imaging. Fluorescence images were analyzed using ImageJ software. Antibodies and their dilution rates are as follows; ATG9A (13509S, Cell Signaling Technology) 1:500; LC3 (14600-1-AP, Proteintech) 1:500; ɔH2AX (ab11174, Abcam); Mitotracker Red CMXRos (M7512, Invitrogen); TOMM20 (11802-1-AP, Proteintech, M2141-4F3, Sigma); Anti rabbit IgG (Alexa 568, ab175470, Abcam); Anti mouse IgG (Alexa 488, ab150105, Abcam).

3.4.15. Senescence-Associated Beta-Galactosidase (SA-β-Gal) Assay

In the SA-ɓ-Gal assay, 12,000 cells were seeded into 24-well culture plate. After 48 hours incubation at 37ŬC, cells were washed with 1X PBS and fixative solution was added on the cells and incubated for 5 minutes at room temperatures. After another washing step, SA-ɓ-Gal staining solution was added. After 12 hours of incubation in a CO2-free incubator at 37ŬC, blue color was fully developed and imaged under the light microscope. To find the percentages of blue-colored cells, number of blue-labeled cells over the total number of nuclei was counted in ten random microscope fields (magnification, 200X).

3.4.16. Cell Proliferation Assay (MTT Assay)

Cells were counted with a hemocytometer and 1000 cells were plated in 5 wells of the 96-well plate. 200 εl of RPMI was put in the 5 wells of the 96-well plate as a blank. After 2 days of incubation of cells at 37 ÁC, 10% MTT (5mg/ml) was added to the cells. Cells with MTT solution were incubated 4 hours at 37 ÁC. After 4 hours, medium was removed. 100 εl DMSO was added onto the cells and incubated for 30 minutes on the shaker. Then, absorbance was measured at 570 nm and 720 nm in each well by using MultiskanTM GO Microplate Spectrophotometer. This procedure was repeated on days 4, 6, and 8. Firstly, 720 nm absorbance values were subtracted from 570 nm absorbance values. Then, the blank value was subtracted from the resulting values. Percentages of absorbances according to day 0 were calculated.

3.4.17. BrdU Staining

The proliferation rate of *ATG9A* knockout cells was measured using bromodeoxyuridine (5-Bromo-2ŊDeoxyuridine, BrdU) labeling in comparison to gREN control cells. This was accomplished by plating 24,000 cells in triplicate on coverslips (12mm) in 24-well cell culture plates. Cells were cultured in a freshly prepared culture medium containing BrdU (30M) for 12 hours. The cells were fixed with 70% ice-cold ethanol for 10 minutes, then 2N HCI was added on the cells and incubated for 20 minutes. The coverslips were then incubated for 2 hours at room temperature with a mouse monoclonal anti-BrdU antibody. To remove excess primary antibodies, cells were washed three times with 1X PBS. The coverslips were then incubated for 1 hour with anti-mouse Alexa Fluor 488 (Abcam). Nuclear counterstaining was performed using DAPI by incubating 1 minute. Coverslips were mounted by using an appropriate mounting medium and imaged under a fluorescence microscope (n=10). To find the percentage of proliferative cells, the number of BrdU-labeled cells over the total number of nuclei that are stained with DAPI were counted in ten random microscope fields (magnification, 200X).

3.4.18. Cell Cycle Analysis

Cells were plated to a 6-well plate as 50,000 cells/well. Cells were cultured in an incubator at 37ĆC for three days. The cells were collected using trypsinization, then centrifuged. After that, cells were resuspended in 1 ml PBS, and fixed for 15 minutes on ice with 70% ice-cold ethanol. The fixed cells were pelleted by centrifugation at 1200 rpm for 15 minutes at 4ĆC before being resuspended in 70 εl of PI solution (2 g/ml propidium iodide, 0.1 mg/ml RNase A, and 0.05% Triton X-100 in PBS) and incubated for 40 minutes at 37ĆC. PI-cell mix was vortexed every 10 minutes for 40 minutes. The stained cells were then centrifuged for 5 minutes at 6000 rpm, resuspended in 100 εl PBS, and transferred in polystyrene tubes. Finally, cells were examined on the LSR Fortessa Flow Cytometer. The FlowJo program was used to determine the cell cycle profile.

3.4.19. Colony Formation Assay (2D Colony Formation)

In each well of the 6-well plate, 2000 cells were plated. Cells were cultured for 12 days. Then, the medium was removed, and the cells were washed with 1X PBS. Cells were fixed with %3.7 formaldehyde and washed with 1X PBS again after 20 minutes of incubation in formaldehyde. The cells were then stained with 0.1% crystal violet (0.1% crystal violet and 20 % ethanol in dH2O) for 45 minutes. Images were taken with the Odyssey CLx imaging system (LI-COR) after washing with dH20 and drying for 1 day. Adobe Photoshop was used for pseudo coloring. In N-acetyl-l-cysteine (NAC) experiments, the medium was replaced with the 10mM NAC/medium mix every 3 days for 12 days.

3.4.20. Soft Agar Assay (3D Colony Formation Assay)

0.5 g agar was dissolved in sterile 25 ml PBS by melting in the microwave oven to achieve a final concentration of 2%. This mixture was autoclaved. To obtain 0.5% agar, 2% agar and complete RPMI heated to 43ÁC were thoroughly mixed. 1 mL of soft agar was poured into each well of the 6-well plate. The mixture was solidified in the hood for 30 minutes at room temperature. To fully dissolve the remaining 2% agar, it was melted in the microwave oven for 20-30 seconds. At 43ÁC, 2% agar was placed in a water bath to cool for 1 minute. To achieve a final concentration of 1.4% agar, the appropriate volume of 1X PBS and 2% agar were mixed. Cells were trypsinized and concentrated to 1.000.000 cells/ml in RPMI. 10.000 cells in 10 εl was added into 1125 εl medium. 375 εl 1.4 % soft agar and 1135 εl medium/ cell were mixed and poured on top of the 0.5 % agar in 6 well plate. After 30 minutes of solidification, plate was then filled with 1 ml of RPMI and cultured in the incubator for 4 weeks by changing the medium twice a week. Images were taken with a light microscope (Olympus CKX41) at 100x magnification from five random fields per well, and colonies with diameters greater than 50 εm were counted.

3.4.21. Wound Healing Assay

Cells were plated on the 6-well plate at %70 confluency as a duplicate. After 24 hours, when cells were %90 confluent, defined areas were scratched with 200 ɑ̃ micropipette tip to obtain a gap without a cell. Medium that contains % 2 FBS and 1 % Penicillin/Streptomycin was added on the cells. Images of the gaps were taken after scratch (0 hour), 24 hours and 48 hours under the Olympus CKX41 inverted light microscope. 8 random pictures were taken per wound (1 well of the 6-well plate). Area of the gaps was analyzed on the ImageJ program with a specific wound healing plugin.

3.4.22. Transwell Invasion and Migration Assay

Transwell invasion chambers (permeable supports) were transferred into a 24-well plate. Each chamber was coated with 50 εl of matrigel matrix diluted 1:40 in serum-free medium and incubated for 2 hours at 37ÁC. 25.000 cells in 200 εl serum-free medium were loaded into the chamber's upper well, and 600 εl medium supplemented with 10% FBS was loaded into the chamber's lower well. The cells were incubated at 37ÁC for 48 hours. After 48 hours, the medium was removed, and the cells were washed with PBS twice. Then, cells were fixed with 3.7% formaldehyde for 2 minutes at room temperature. After two PBS washes, cells were permeabilized for 20 minutes in 100% methanol. Cells were washed with PBS twice before adding 700 εl 0.1% crystal violet to the wells. Cells were stained at room temperature for 15 minutes. Non-invasive cells were scraped off with cotton swabs after washing with PBS to clean the crystal violet. Invasive cells were counted in five different microscope fields under a light microscope (Olympus CKX41) randomly (magnification, 100 x). ImageJ was used to count the cells. 25.000 cells were seeded in matrigel-free transwells for the migration assay. The staining protocol was followed as in invasion assay after 48 hours.

3.4.23. Comet Assay

Firstly, 1 g agarose gel was weighed and dissolved in 100 mL distilled water. The mixture was melted in a microwave oven and 1% agarose gel was prepared. Thin slides were used in this experiment. Slides dipped into 1 % agarose gel and one side of the slides was cleaned. Agarose on one side of the slides was solidified. During this time, cells were trypsinized and harvested with RPMI. 20.000 cells were transferred to the microcentrifuge tube and centrifuged. Cells were resuspended in 1 mL 1X PBS. 400 εl cell mixture and 1.2 mL 1% agarose gel at 40ŬC were mixed. The mixture was poured on the agarose found on the slide immediately. For 2 minutes, the slides were let to solidify the agarose. After the agarose solidified, the slides were placed in the A1 Lysis buffer-containing dish and incubated in the dark overnight at 4ŃC. After removing the slides, they were immersed in the A2 rinse solution for 20 minutes at room temperature. This step was repeated twice to ensure that all salt and detergent were removed. Slides were placed in the tank, and electrophoresis was performed in solution A2 for 25 minutes at 40mA, 20V. The slides were taken out of the tank and rinsed with distilled water. 100 εl of a 10 εg/ml propidium iodide stock solution was poured directly onto the slide and incubated for 20 minutes. The slides were rinsed with distilled water. At least 50 comet images from each slide were examined. For analysis, the ImageJ-OpenComet tool was used (55).

3.4.24. FACS Analysis and Apoptotic Assay (Annexin V)

Using the Annexin V Apoptosis Detection kit, MPM cells were double stained with Annexin V and Propidium Iodide (PI). Cells were seeded with a 6-well plate as 100,000 cells/well. After 24 hours, cells were trypsinized and centrifuged. Then, cells were washed with PBS, centrifuged, and suspended in 36 εl of Annexin V binding buffer containing 4 εl PI and 2 εl Annexin V. After 15 minutes of incubation at room temperature, samples were mixed with 120 εl of Annexin V binding buffer and transferred to FACS tubes and kept on ice until Flow Cytometry analysis. FlowJo was used to analyze the data. In all FACS analyses, the four quadrants (Q1, Q2, Q3, and Q4) are marked. Q1 (positive for PI) was defined as necrotic cells. Q4 (negative for both Annexin V and PI) was defined as live cells. Q2 (positive for Annexin V) and Q3 (positive for both Annexin V and PI) were defined as early and late apoptotic cells, respectively.

3.4.25. DCFDA Staining

10,000 cells were plated into the 96 well plates (black and transparent) for the DCFDA (2Ŋ,7Ŋ-Dichlorofluorescin Diacetate) staining experiment and incubated at

370C. All medium in the wells was removed carefully with the help of vacuum. 100 εL DCFDA dye was added. 100 εL PBS was added into negative control (NC) groups. After 1 hour of incubation, DCFDA dye solution was removed with the help of vacuum. 100 εL medium without FBS was added (except positive control). 200 εl H2O2 was added into the positive control group. After 1 hour incubation, measurement was done with the Thermo ScientificÊ VarioskanÊ LUX multimode microplate reader at 495 nm and 527 nm. For this experiment black 96 well plates were used. The same protocol was performed for the transparent plate and images were taken with the help of fluorescent microscope (magnification, 100 x).

3.4.26. AUTODOT Staining

24,000 cells were plated on coverslips (12mm) in 24-well plates as duplicates. After 24 hours of incubation, cells were washed with PBS three times and fixed with 4 % formaldehyde for 15 minutes. After washing with PBS, cells were permeabilized with PBS-T for 10 minutes. Cells were treated with AUTODOT solution (1:1000 in 1X PBS) for 15 minutes at 37ÜC. After staining, blocking buffer (5% BSA, 0.1 mg RNAse in 1X PBS) was added onto the cells. After washing, cells were treated with 1 εg/ml PI (PI in 1X PBS) for 3 minutes. Cells were mounted on cover glass after washing with distilled water. Confocal microscopy was used for imaging.

3.4.27. RNA Sequencing Analysis

The bioinformatics analysis of the data obtained as a result of RNA sequencing was performed by Sude Erıκ, a graduate student in our laboratory. A multi-stage protocol was used to evaluate the RNA sequencing data. Quality checks of raw reads (.fastq files) produced by the sequencing platform were performed with FastQC. Adapter sequences were removed with the Cutadapt algorithm. The subread alignment algorithm was used to align the sequences to the reference genome. SAMtools functions are called to obtain basic statistics on alignment (56). The measurement of gene expression levels was carried out with the featureCounts algorithm. R scripts written by us, and the edgeR package were used to determine the differences in gene expression levels between groups. In the detection of genes with different expression levels, in addition to the p-value and false discovery rate (FDR), which expresses statistical significance, fold change or quantitative per million, which expresses the difference between the two compared conditions as directional (down-regulated or up-regulated). Measures such as the number of reads (CPM) were taken into account. The ggplot2 R package was used to visualize the results obtained (57). Functional annotations of genes whose expression changes significantly ($p<0.05$) and path term enrichment analyzes of Gene Ontology (GO) and Kyoto Encyclopedia of Genes and Genomes (KEGG) were performed with the ClusterProfiler package. All the graphs are created using the R programming language.

3.4.28. Gene Set Enrichment Analysis (GSEA)

Expression files (.gct) were generated by utilizing the counts per million (CPM) values derived from RNA-Seq for each individual sample. Permutation type was set to gene set since there were fewer than 7 samples per group. To create custom annotation sets, MSigDB XML Browser software was used and keywords for the search were selected based on known ATG9A functions from the literature. Keywords corresponding to each topic exported as gene set matrix files (.gmt) for input into GSEA. As for the GSEA, a list of DEGs with phenotype labels ñWTò vs. ñKOò was uploaded to the GSEA tool, and false discovery rates (FDR), nominal p-values (p), and normalized enrichment scores (NES) were computed after 1000 random permutations of the gene set. FDR < 0.25 and p < 0.05 were accepted as statistically significant. Key words used in analysis: Oxidative, Arrest, Mitochondrial, DNA damage, Apoptosis, Autophagy, Cell cycle, Cell division, Invasion, Migration, Proliferation, ROS, Survival, Senescence, p53, E2F, MYC.

3.4.29. Hanging Drop Spheroid Formation

Cells were seeded in 1000 cells in 10 εl, 2000 cells in 10 εl, 1000 cells in 20 εl, and 2000 cells in 20 εl conditions as hanging drops. After 48 hrs, cells were imaged under stereo microscope.

3.5. Study Plan and Calendar

September 2020-December 2020

Literature Search and Gene Selection

	ATG9A gRNA Cloning into pECPV vector and Validation Experiments
December 2020-December 2021	*ATG9A* gRNA Cloning into pLentiCRISPR v2 vector and Knockout Experiments
December 2021-May 2022	*ATG9A* Overexpression Cloning Overexpression Experiments
May 2022-November 2022	*ATG9A* Rescue Cloning and Rescue Experiments
November 2022-February 2023	NAC Experiments and RNA Sequencing
February 2023-June 2023	Tmem41B gRNA Cloning into pLentiCRISPR v2 and pECPV vectors and Knockout Experiments

3.6. Data Evaluation

The results were presented as the mean Ñ standard deviation (SD). Statistical analyses were performed using GraphPad Prism 8 software. Student's t-test and One-way ANOVA were employed to compare two independent groups, while multiple groups were compared using Two-way ANOVA. Significance was determined using the Benjamini, Krieger, and Yekutieli two-stage linear step-up approach. Significance levels were denoted as follows: p-value < 0.05: *, p-value < 0.01: **, and p-value < 0.001: ***.

3.7. Limitation of the Study

Single cell clones could not be obtained in knockout experiments because an inducible system could not be developed in our laboratory. On the other hand, the same infected clones could not be used for all experimental settings since after some time in culture, cells exhibiting *ATG9A* depletion begin to die. Variations between repeats are produced by polyclonal lines.

3.8. Ethics Committee Approval

This study was approved by the IBG local ethics committee with ethics protocol number 2021-018.

4. <u>RESULTS</u>

4.1. Selection of the *ATG9A* gene

Dr. Ece ¢akēoĵ lu carried out a genome-wide CRISPR/Cas9 screening with the aim of identifying critical vulnerabilities that contribute to MPM carcinogenesis. That study primarily focused on genes and signaling pathways associated with MPM cell survival and growth. In this CRISPR screen, H2052, H2452, and MeT-5A cell lines were infected with the Brunello gRNA pool library, allowing for the identification of genes based on their specific CRISPR gene scores. The PhD thesis with the identifier DEU.HSI.PhD-2016850041 provides a detailed account of the CRISPR/Cas9 screen experiments conducted by Dr. Ece ¢akēoĵ lu. For clarity and ease of understanding, Figure 15 illustrates the schematic representation of the CRISPR/Cas9 screen experiments.

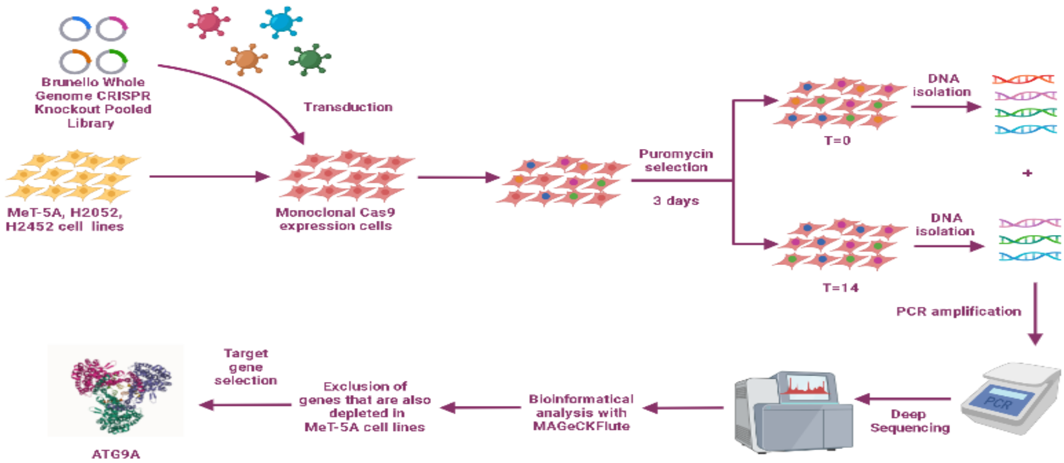

Figure 15: CRISPR/Cas9 screen diagram. It was created in BioRender.

Following the genome-wide CRISPR/Cas9 experiments, the results were assessed based on the following criteria:

1. Identification of genes that did not score in the non-tumorigenic MeT-5A cell line but exhibited a relatively higher depletion score in the cancer cell lines.
2. Assessment of the inverse correlation between the expression of identified genes and overall survival in MPM patients.
3. Selection of under-studied genes that have not been extensively investigated.

Initially, genes meeting the first criterion were compiledð those that displayed a high depletion score in cancer cell lines but did not score (or had a relatively lower depletion score) in the MeT-5A normal cell line. Subsequently, the association of these genes with MPM patient survival was examined using the UALCAN (http://ualcan.path.uab.edu/) (58) and GEPIA (http://gepia.cancer-pku.cn/) (59) tools, utilizing the TCGA MPM dataset. This analysis revealed that increased expression of certain genes in MPM was inversely correlated with patient survival. Next, the genes were evaluated according to the third criterion; being an under-studied gene. During this assessment, we noticed that three of the high-scoring genes were related to autophagy (*ATG9A, TMEM41B*, and *VPS37A*). Among these genes, ATG9A stood out as it displayed a higher depletion score in cancer cell lines compared to the non-tumorigenic cell line (Figure 16). Intriguingly, despite being relatively less studied, ATG9A has recently gained attention due to its role in autophagy and is recognized as a crucial gene in this process. Consequently, ATG9A was selected for further investigation.

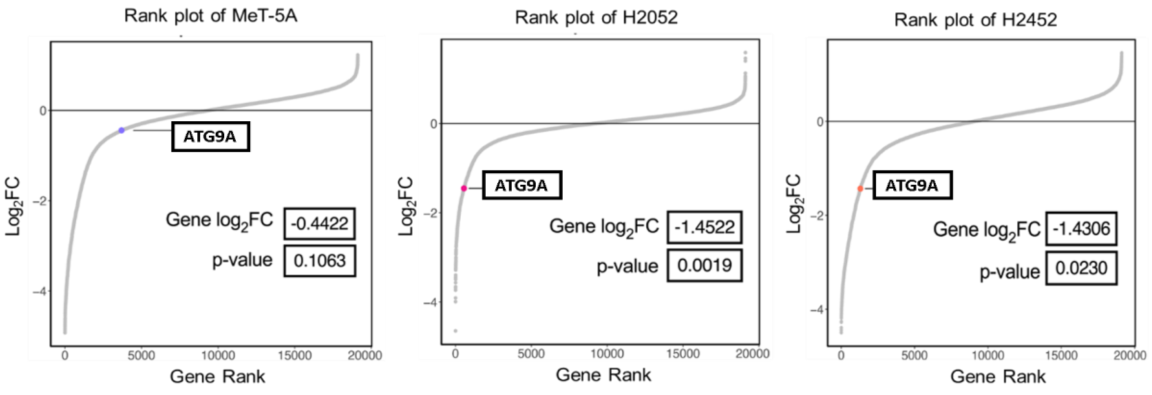

Figure 16: Waterfall results of MeT-5A, H2052 and H2452 cell lines. CRISPR gene scores and p-values for *ATG9A* are shown.

Upon closer examination of the gRNA scores, we found that, except for the gRNA 3, the other gRNAs did not yield a significant score for the MeT-5A cell line. In the H2052 cell line, the first three gRNAs displayed high depletion scores, whereas gRNA 4 did not provide a good score. Similarly, in H2452, three gRNAs exhibited depletion scores, but gRNA 4 had a very low depletion score (Table 29). Notably, gRNA 3 and gRNA 4 showed divergent outcomes. To address these discrepancies, our focus shifted towards evaluating the total CRISPR gene scores, rather than individual gRNA scores. Examining the total gene scores depicted in Figure 16 for the *ATG9A* gene, it was evident that the MeT-5A cell line displayed a substantially low score, while the cancer cell lines exhibited high depletion scores. Based on these findings, it can be concluded that the *ATG9A* gene aligns with the first criterion, indicating a significant depletion in cancer cells compared to the non-tumorigenic MeT-5A cell line.

Table 29: Log fold change values of *ATG9A* gRNA 1, gRNA 2, gRNA 3 and gRNA 4 in MeT-5A, H2052 and H2452 cell lines.

Cell Lines	**Log fold change of the *ATG9A* gRNAs used in the screen**			
	gRNA 1	gRNA 2	gRNA 3	gRNA 4
MeT-5A	-0.36	-0.52	-1.26	0.39
H2052	-1.43	-2.39	-1.47	0.34

H2452	-2.31	-2.04	-0.81	-0.11

When examining the association between *ATG9A* expression and MPM patient survival using the UALCAN tool and the TCGA MPM dataset, we observed that higher expression levels of the *ATG9A* gene were negatively correlated with mesothelioma survival. This relationship is illustrated in Figure 17, indicating that increased *ATG9A* expression is associated with poorer survival outcomes in patients with mesothelioma.

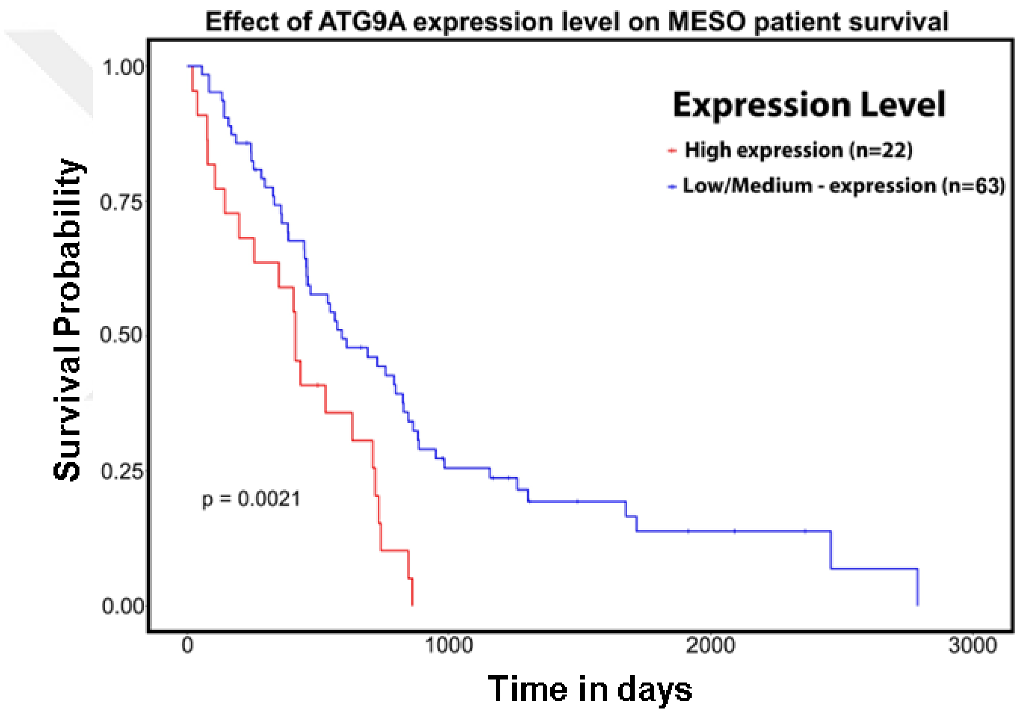

Figure 17: Kaplan-meier curve for *ATG9A* gene expression status in MPM. The TCGA MPM data set was retrieved from the UALCAN tool (58). This data set contained 22 high *ATG9A* expression patients and 63 low/medium *ATG9A* expression patients. p-value is calculated as 0.0021.

Considering the third criterion mentioned above: the function of the ATG9A gene has recently been discovered, albeit with limited information available in existing literature regarding its association with cancer. Following a comprehensive assessment of these three criteria, the *ATG9A* gene emerged as a promising candidate for future investigations at the molecular level. Notably, as indicated in Table 29, the application of all the gRNAs available in the Brunello library yielded suboptimal scores in cancer cells and resulted also in perturbations in MeT-5A cells. To address this inherent bias, gRNA 3 and gRNA 4, which were responsible for the observed deviations, were excluded from further analysis. Instead, two novel gRNAs were designed to target exon 8, a region deemed crucial for ATG9A's scramblase activity. These newly designed gRNAs were designated as new gRNA 3 and gRNA 4. Figure 18 provides a visual representation of the precise locations where all the gRNAs used in the future molecular studies target within the ATG9A transcript structure.

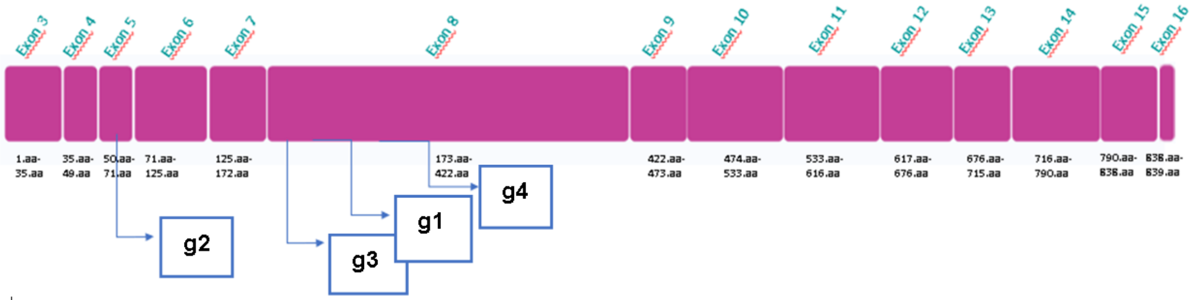

Figure 18: Target locations of four gRNAs. gRNA 2 targeted exon 5 of the *ATG9A* gene while gRNA 1, gRNA 3 and gRNA 4 targeted exon 8 of the *ATG9A* gene.

In the continuation of our preliminary work, a competition assay was performed to validate the findings of the CRISPR/Cas9 screen. To this end, four *ATG9A* gRNAs were individually cloned into the pECPV vector, which encodes the traceable Venus fluorescent protein (a YFP variant). As a negative control, we used a gRNA specific to the Renilla luciferase gene, which has no specific target in the human genome. Following the cloning of the gRNAs into the pECPV backbone, the vectors were co-transfected with two helper plasmids for virus packaging. Subsequently, MeT-5A, H2052 and H2452 cells were infected with the lentiviral particles, aiming for partial transduction. The competition assay was conducted in two parts: the first part involved gRNA 1 and gRNA 2 (Figure 19 A), and the second part involved gRNA 3 and gRNA 4 (Figure 19 B). The primary objective of the assay was to quantify the proportions of Venus-positive cells, which correspond to the infected cells, using flow cytometry every 3-5 days. Throughout the experiment, no significant changes in Venus positivity were observed in cells infected with the gRen negative control across all cell lines. However, a significant decrease in the percentages of Venus-positive cells was observed over time in H2052 and H2452 cells infected with *ATG9A* gRNA 1, gRNA 2, gRNA 3, and gRNA 4. Additionally, a slight decrease in the percentages of Venus-positive cells was observed in MeT-5A cells infected with all *ATG9A* gRNAs, although this decrease remained around 20% at maximum. In summary, these findings are consistent with the outcomes obtained from the CRISPR screen, indicating that depletion of *ATG9A* is closely linked to a strong impairment in MPM cell survival and proliferation.

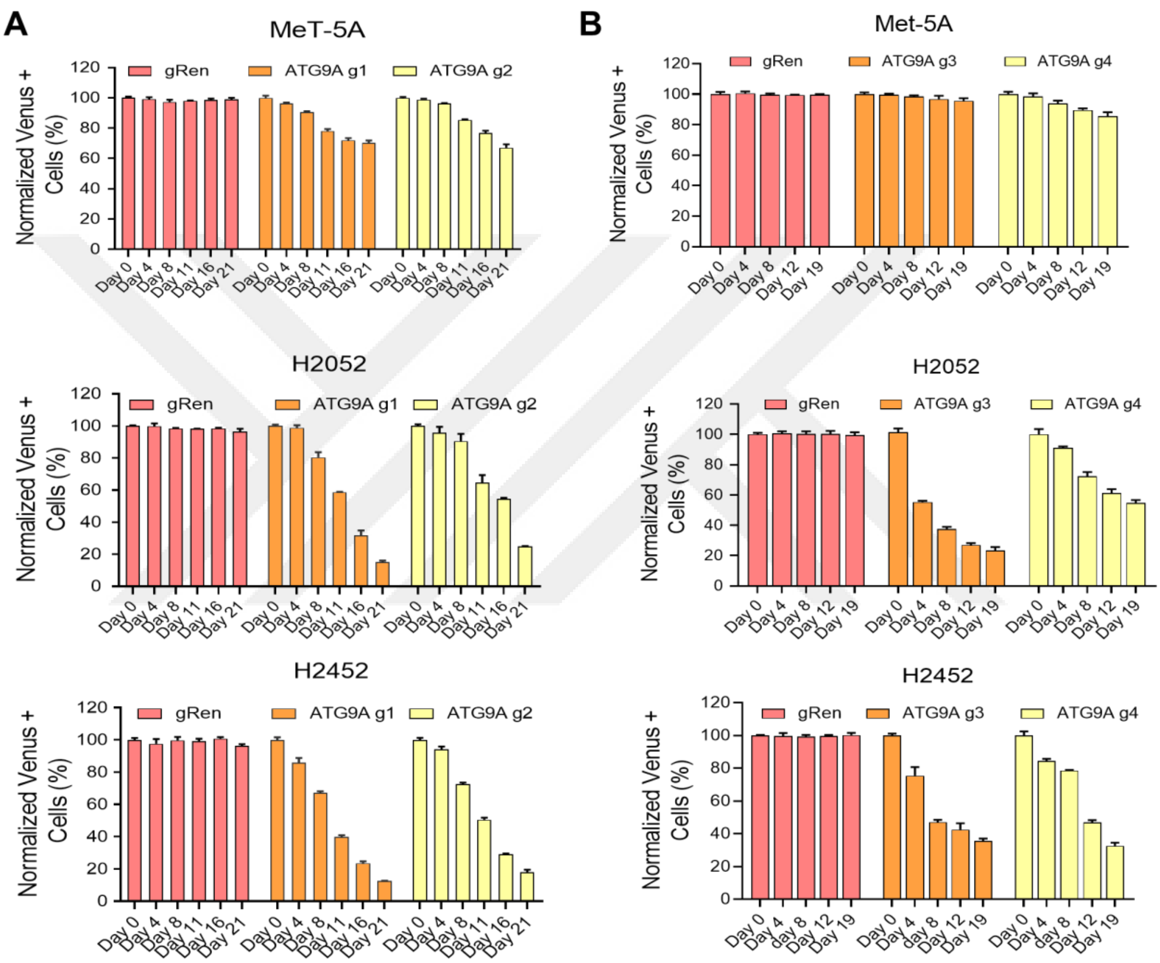

Figure 19: Competition assay in MPM cell lines targeted with *ATG9A* gRNAs (g1 through g4) or gRen. A) Normalized Venus-positive (+) cell percentages in gRNA 1 (g1) and gRNA 2 (g2) targeted cells. B) Normalized Venus-positive (+) cell percentages in gRNA 3 (g3) and gRNA 4 (g4) targeted cells. gRen was used as a negative control. Venus positive cell percentages of Day 0 samples were normalized to 100. The other days were normalized accordingly.

4.2. Generation of Polyclonal *ATG9A* Knockout Cells

Having validated the outcomes of the CRISPR screen and substantiated the influence of depleting the *ATG9A* gene on MPM cell survival, our research focus shifted to molecular studies investigating the impact of *ATG9A* gene silencing on MPM carcinogenesis. To execute this exploration, we individually cloned gRen and all *ATG9A* gRNAs into the lentiCRISPR v2 vector, followed by virus packaging and infection of MeT-5A, H2052, and H2452 cells. Following infection, cells were selected using puromycin, resulting in the creation of *ATG9A* knockout cells with a polyclonal nature. The level of *ATG9A* knockout was confirmed by western blot analysis (Figure 20). Notably, ATG9A is a 100 kDa protein. However, ubiquitinated or glycosylated versions of ATG9A may yield multiple bands in western blot analysis (3). The cell lysates were collected on the 12th day post infection.

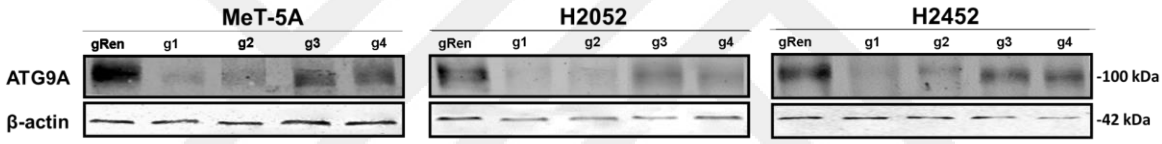

Figure 20: Validation of *ATG9A* depletion in MeT-5A, H2052 and H2452 cells by western blotting. ß-actin served as the internal control. *ATG9A* gRNA 1, gRNA 2, gRNA 3 and gRNA 4 had been referred to as g1, g2, g3 and g4 respectively.

4.3. *ATG9A* Depletion Reduces 2D Colony Formation Capacity of MPM Cells

To gain insights into the role of ATG9A on cellular proliferation and growth, we conducted an investigation utilizing a two-dimensional (2D) colony formation assay. Cell lines subjected to *ATG9A* perturbation and control cells (gRen infected) were employed in this study. Following an eight-day period post infection, we seeded 2000 cells (including those infected with gRen and all *ATG9A* gRNAs) into six-well plates. The experiment was conducted over a span of 11 days (Figure 21). The results of this assay revealed a substantial decrease in the 2D colony formation capacity of *ATG9A* deficient H2052 and H2452 cell lines, in comparison to the control cells (gRen). It is important to note that although MeT-5A cells also exhibited a response to *ATG9A* depletion, the magnitude of the effect was relatively modest in this non-tumorigenic cell line. These observations collectively suggest that *ATG9A* silencing selectively impairs the ability of cancer cells to form colonies in a 2D culture setting. Integrating the findings derived from both the colony formation assay and the western blot analysis, it becomes apparent that gRNA 1 and gRNA 2 exhibit greater efficacy in targeting *ATG9A* when compared with gRNA 3 and gRNA 4. Based on these observations, we have decided to prioritize and focus exclusively on gRNA 1 and gRNA 2 for future experiments.

A

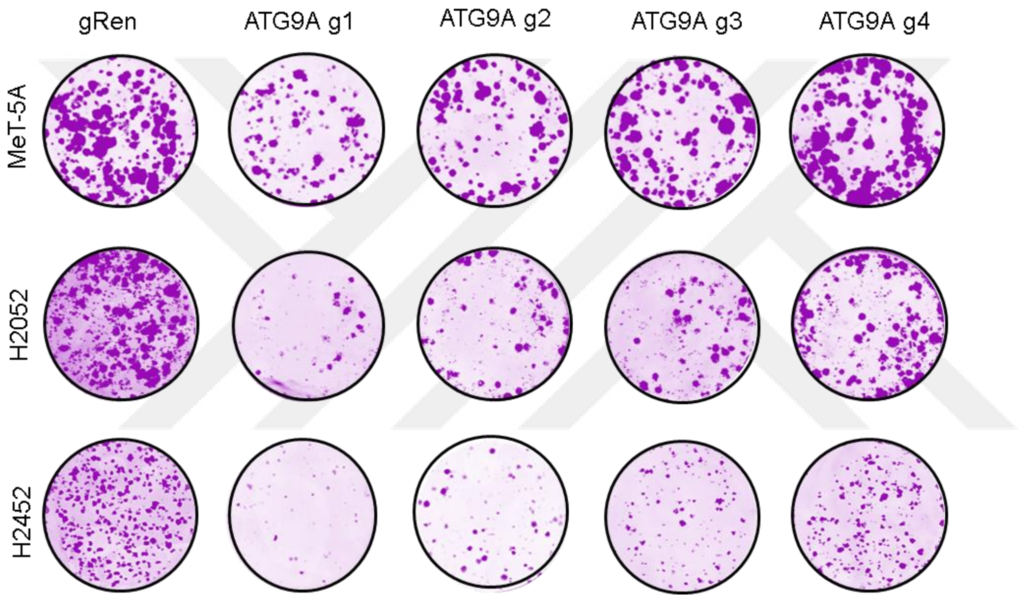

B

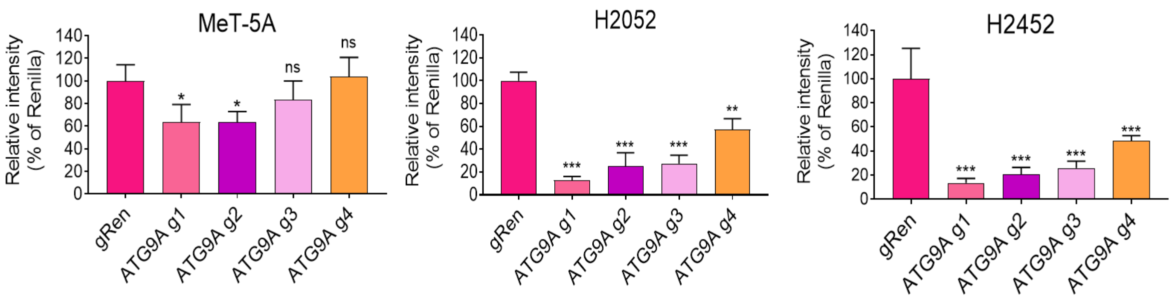

Figure 21: 2D colony formation upon *ATG9A* depletion in MeT-5A, H2052 and H2452 cells. A) Representative images acquired using the LI-COR scanner are shown. Cells were stained with crystal violet. The gray scale images were pseudo-colored using Adobe Photoshop software, with the color blue/purple representing the crystal violet stain. B) Renilla control (gRen) values for each cell line were normalized to 100, while

the values for other conditions were normalized relative to gRen. Graphs show mean Ñ standard deviation (SD), with n=3. Significance levels are denoted as follows: *p<0.05, **p<0.01, ***p<0.001, one-way ANOVA with multiple comparisons.

4.4. *ATG9A* Depletion Decreases 3D Anchorage-Independent Growth of MPM Cells

Building upon our findings from 2D cell culture, we then aimed to evaluate the impact of *ATG9A* depletion on the three-dimensional (3D) anchorage-independent growth ability of MPM cells. To interrogate this phenomenon, we performed a soft agar colony formation experiment. Briefly, we seeded the cells into 6-well cell culture plates coated with Noble agar, creating a supportive environment for anchorage-independent growth. Following standard cell culture protocols, the cells were allowed to proliferate and develop colonies over a period of 30 days. Subsequently, we conducted microscopic examination of the colonies, capturing images from five random areas. We utilized the ImageJ tool to measure the sizes of the colonies, specifically focusing on the number of colonies with a diameter exceeding 50 εm (60). Notably, MeT-5A cells failed to form 3D colonies in soft agar. As expected, we observed a notable finding in *ATG9A* gene perturbed cancer cells. Specifically, the colonies formed by these cells appeared smaller compared to the control group. In other words, silencing *ATG9A* appeared to attenuate the 3D colony formation capacity of cancer cells (Figure 22).

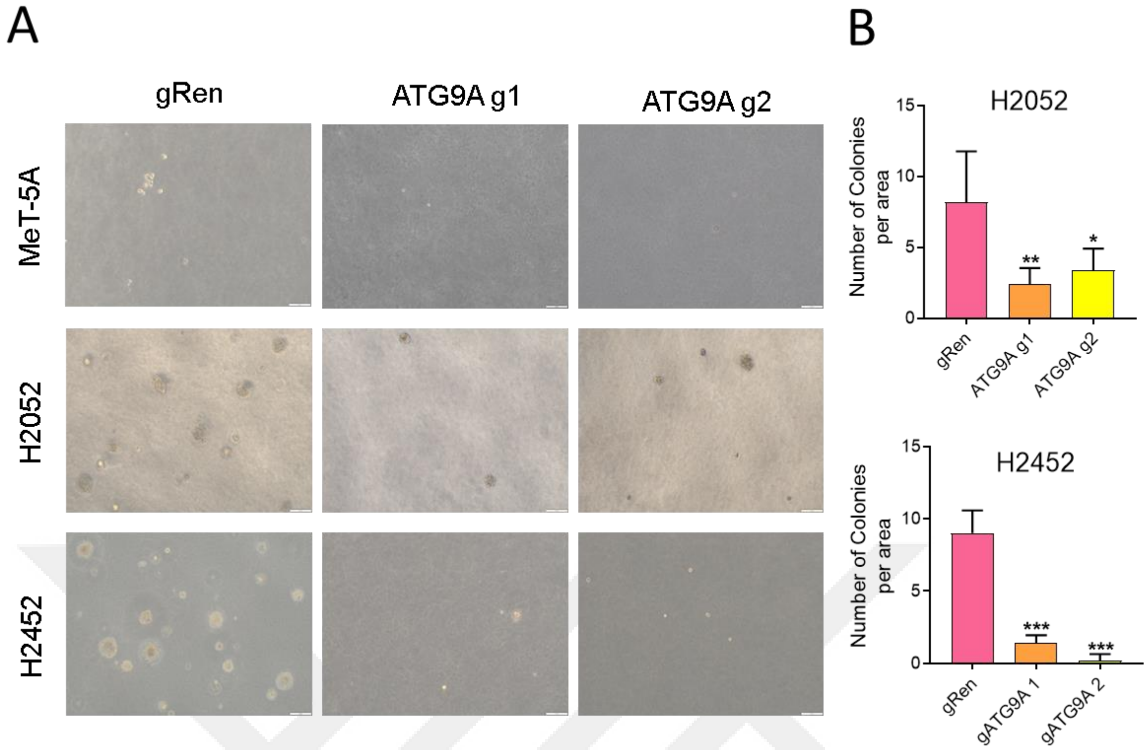

Figure 22: 3D anchorage-independent soft agar growth of *ATG9A* knockout MeT-5A, H2052, and H2452 cells. A) Representative images were generated by merging multiple layers of agar using Adobe Photoshop. Scale bar: 100 Õm. B) Number of colonies with a diameter greater than 50 εm were counted using the ImageJ program. All data are presented as mean Ñ SD, with n=5. Studentȏs t-test, * p<0.05, ** p<0.01, *** p<0.001.

In addition to the soft agar experiment, we conducted a spheroid formation assay to investigate the 3D anchorage-independent growth ability of MPM cells (Figure 23). For this assay, cells were seeded under four different conditions, varying in cell density and volume (1000 cells in 10 εl, 2000 cells in 10 εl, 1000 cells in 20 εl, and 2000 cells in 20 εl), to elucidate their propensity to form spheroids in hanging drop spheroid formation assay. Interestingly, the MeT-5A and H2452 cell lines failed to generate spheroids across all tested conditions. In contrast, the H2052 cells exhibited spheroid formation exclusively in the 2000 cells in 20 εl condition. Remarkably, upon *ATG9A* knockout, H2052 cells formed smaller spheroids compared to the control cells, and in some instances, failed to form spheroids altogether. These findings underscore the significant role of ATG9A in modulating the size and formation of spheroids in H2052

MPM cells, thereby shedding light on its regulatory influence on 3D anchorage-independent growth behaviour.

A

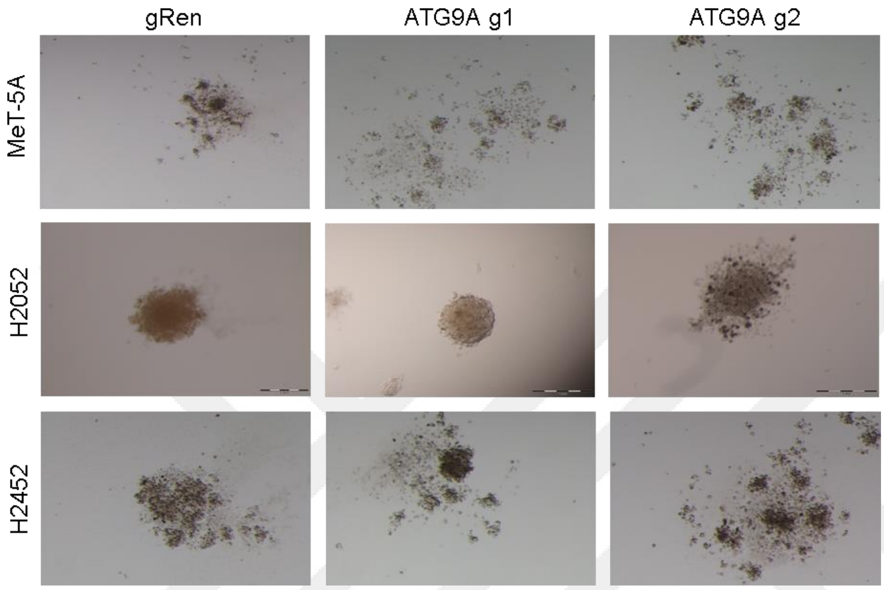

B

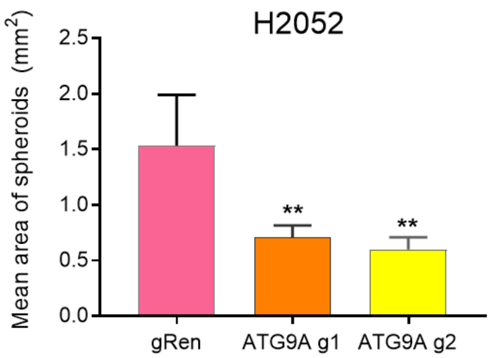

Figure 23: Spheroid formation assay of H2052, H2452 and MeT-5A cells lines. A) Representative images were captured from the 2000 cells in 20 εL condition. Scale bar, 1mm B) The area of the spheroids was measured using ImageJ software. The data are presented as mean Ñ SD, with n=7. Significance levels were determined using the Studentõs t-test and indicated as **p<0.01.

4.5. Knocking out *ATG9A* Gene Attenuates MPM Cell Proliferation and Growth

To demonstrate the impact of *ATG9A* gene depletion on the proliferation and growth of MPM cells, we specifically employed MTT and BrdU assays. Initially, we conducted an MTT assay by seeding cells on four different 96-well cell culture plates. Two days after seeding, the first spectrophotometric measurements were obtained. Subsequent measurements were taken at two-day intervals (Figure 24). The results indicated that the growth of *ATG9A* depleted cancer cells was significantly attenuated compared to the gRen infected control cells. Furthermore, there was no significant change in the growth of *ATG9A* deficient MeT-5A cells.

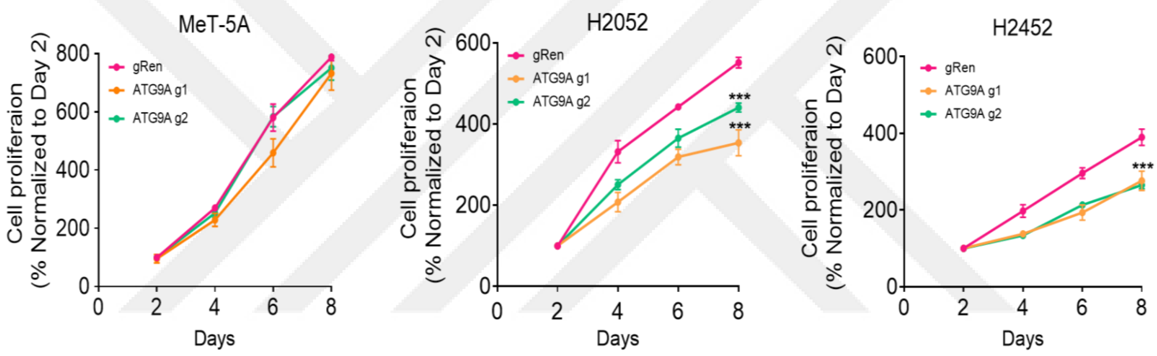

Figure 24: Time-dependent cellular growth in *ATG9A* knockout cells. The initial results were obtained two days after seeding and were normalized to a value of 100. Subsequent results from other time points were normalized relative to the average value obtained on the second day. The data are presented as mean Ñ SD, with a sample size of n=5. Statistical analysis was performed using the Student's t-test, with significance depicted as ***p<0.001.

Next, we examined the proliferation capacity of *ATG9A* knockout cells following the BrdU incorporation assay. The cells were seeded onto 24-well plates and one day later, they were labeled with BrdU reagent. After 12 hours, we assessed the incorporation of BrdU into DNA as an indicator of DNA replication. BrdU is a thymidine analog that replaces thymidine during DNA synthesis and can be detected using immunohistochemical methods (61). It serves as a marker for DNA replication and enables the enumeration of mitotic cells. Upon analyzing the results, we observed a notable decrease in the number of green-stained proliferating cells in *ATG9A* silenced cells compared to the total number of cells stained with DAPI, a DNA-specific dye, in all cell lines examined. As expected, this decrease was less evident in the non-tumorigenic cell line, MeT-5A, suggesting a relatively milder effect on proliferation in this context (Figure 25).

A

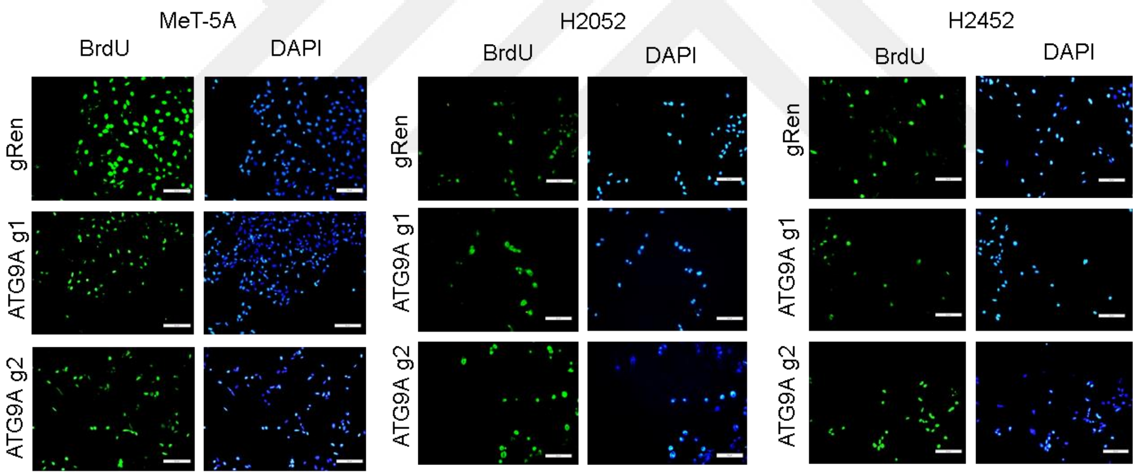

B

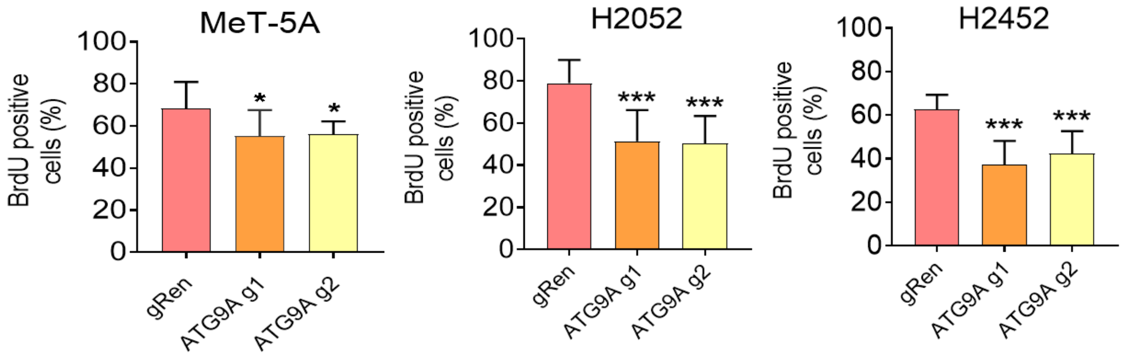

Figure 25: Cellular proliferation in *ATG9A* knockout clones. A) Representative images of BrdU (green) and DAPI (blue) staining are shown. DAPI was used as a nuclear counterstain, providing visual contrast. Scale bar, 50 Õm B) For quantitative analysis, we randomly selected 10 areas in each condition and counted the cells labeled with DAPI and/or BrdU. The ratio of BrdU-labeled cells to DAPI-stained cells was calculated as the percentage (%) of BrdU-positive cells. The data are presented as mean Ñ SD, with n=10. Statistical analysis was conducted using One-way ANOVA and significance levels are expressed as *p<0.05, ***p<0.001.

4.6. Impaired Proliferation in *ATG9A* Knockout MPM Cells Can Be Rescued by Ectopic Expression of *ATG9A*

As alluded to earlier, the depletion of *ATG9A* gene in MPM cancer cells led to a significant deceleration in proliferation and growth, highlighting its involvement in these cellular processes. To ascertain the specificity of this effect, we conducted a rescue experiment. In this study, we employed an *ATG9A* overexpression vector (i.e., pMXs-puro-RFP-ATG9A) for rescue purposes, while an empty vector with the ATG9A coding sequence deleted served as the negative control (NC). First, we genetically perturbed the *ATG9A* gene using gRNA 1 and gRNA 2, while gRen infected cells were employed as controls. Then, the resulting clones were infected with virus particles carrying either the *ATG9A* overexpression vector (rescue clones) or the NC vector (negative control clones). Following puromycin selection, successful rescue of the *ATG9A* gene in the cancer cell lines was verified through western blot analysis (Figure 26). Notably, the pMXs-puro-RFP-ATG9A vector encodes an RFP-ATG9A fusion protein, resulting in a higher molecular weight of approximately 130 kDa, compared to the native 100 kDa ATG9A protein.

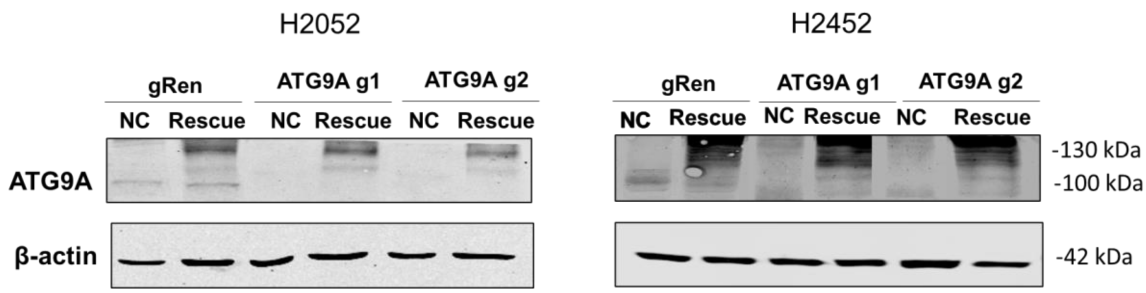

Figure 26: Ectopic overexpression of *ATG9A* rescues protein expression in *ATG9A* knockout cells. Western blot results of rescue and negative control clones. An ATG9A specific antibody was used. ϐ-actin was used as loading control.

Subsequent to the establishment of the rescue clones, we proceeded to conduct a 2D colony formation assay. Strikingly, upon rescuing *ATG9A* expression, we observed that the rescue clones exhibited a strong restoration in their proliferation capacity (Figure 27).

A

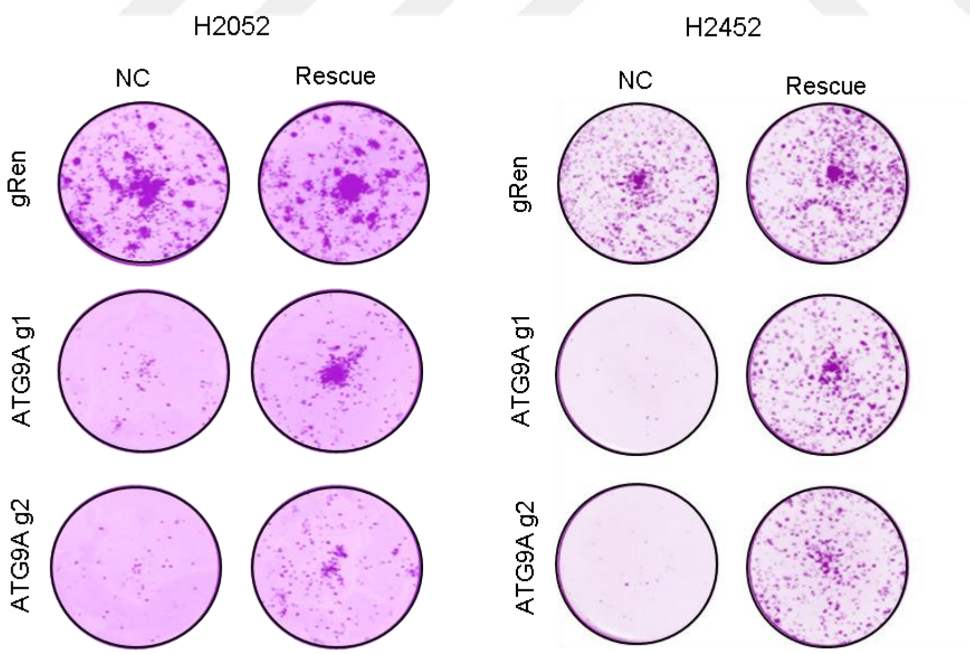

B

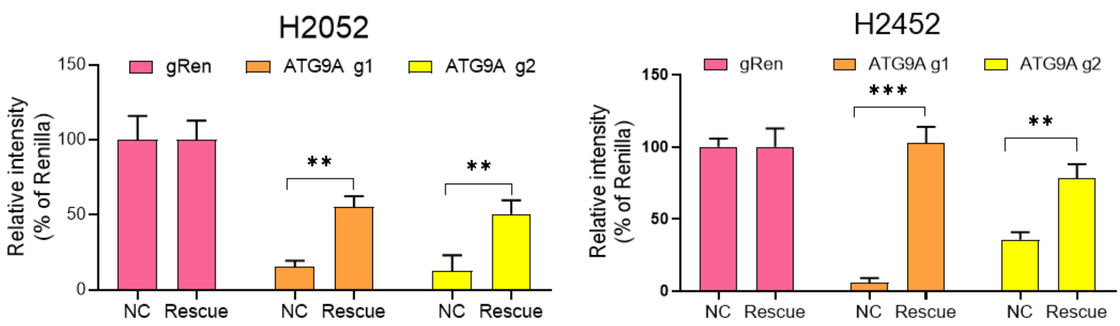

Figure 27: 2D colony formation results of rescue and NC clones. A) Representative images were selected from three replicates. Cells were stained with crystal violet. Pseudocoloring was made to resemble the color of crystal violet. B) Intensities of each condition were measured using ImageJ software. Intensity of Renilla control was normalized to 100. Others were normalized according to Renilla control. Mean Ñ SD, n=3, **p<0.01, ***p<0.001, One way ANOVA.

Collectively, the successful restoration of normal growth dynamics upon *ATG9A* gene rescue provides compelling evidence supporting the specific role of *ATG9A* depletion in the observed deceleration of proliferation and growth in MPM cancer cells.

4.7. *ATG9A* Knockout Impairs Cell Proliferation and Growth via Multiple Mechanisms

4.7.1. ATG9A Gene Silencing Causes G2 Cell Cycle Arrest

Elucidating the underlying mechanisms governing cell proliferation and growth is essential for advancing our understanding of cellular dynamics regulated by ATG9A. To address this, we aimed to investigate the effects of *ATG9A* gene knockout on cell cycle progression. Through comprehensive cell cycle assays, we observed a significant increase in the G2 phase arrest across multiple cell lines following *ATG9A* gene knockout. Particularly, H2052 cells demonstrated an increase in G2 phase population from approximately 8% to 14%, accompanied by a reciprocal decrease in the S phase. Additionally, in H2452 cells, an increase in G2 phase from 26% to 34% was observed, concomitant with a decrease in the G1 phase (Figure 28). Conversely, while MeT-5A cells exhibited an increase in G2 phase from 19% to 24%, this alteration was not associated with a decrease in S phase cells.

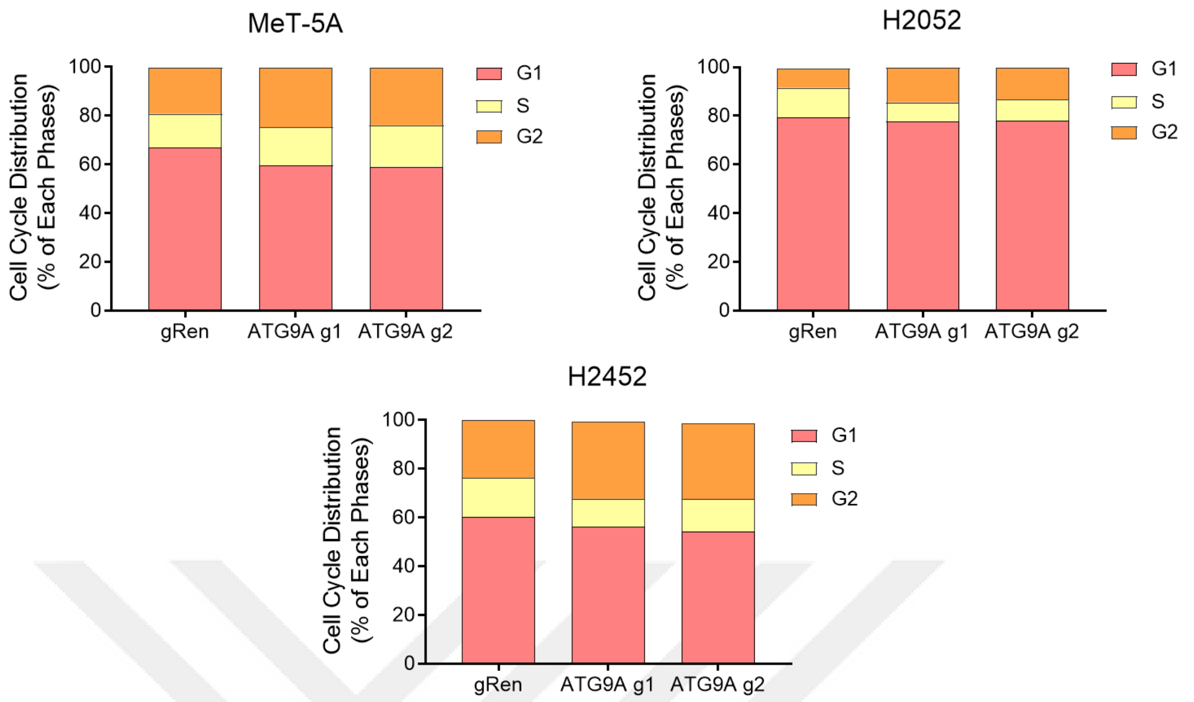

Figure 28: *ATG9A* depletion leads to G2 phase arrest, with a reciprocal decrease in S phase population in MPM cells. Representative graphs are shown. Columns represent the mean from three biological replicates.

4.7.2. ATG9A Gene Silencing is Associated with an Increase in Cellular Senescence

Following the identification of G2 cell cycle arrest in *ATG9A* deleted cells, we sought to explore whether these cells enter a state of cellular senescence. Cellular senescence represents an irreversible cell cycle arrest and can be detected using the senescence-associated ɓ-galactosidase assay (SA-ɓ-Gal) (62). The assay involves the use of X-gal substrate, which generates a blue color upon enzymatic reaction in senescent cells. In this experiment, we aimed to evaluate the occurrence of cellular senescence in *ATG9A* depleted cells using the SA-ɓ-Gal staining technique. To this end, cells were plated in 12-well plates and stained with SA-ɓ-Gal staining solution for 12 hours. The SA-ɓ-Gal staining results revealed a significant increase in the number of blue-colored cells in *ATG9A* knockout cells compared to gRen control cells. This observation suggests an elevated occurrence of cellular senescence following *ATG9A* knockout. Intriguingly, the increase in cellular senescence was particularly prominent in cancer cell lines when compared to the MeT-5A cell line (Figure 29).

A

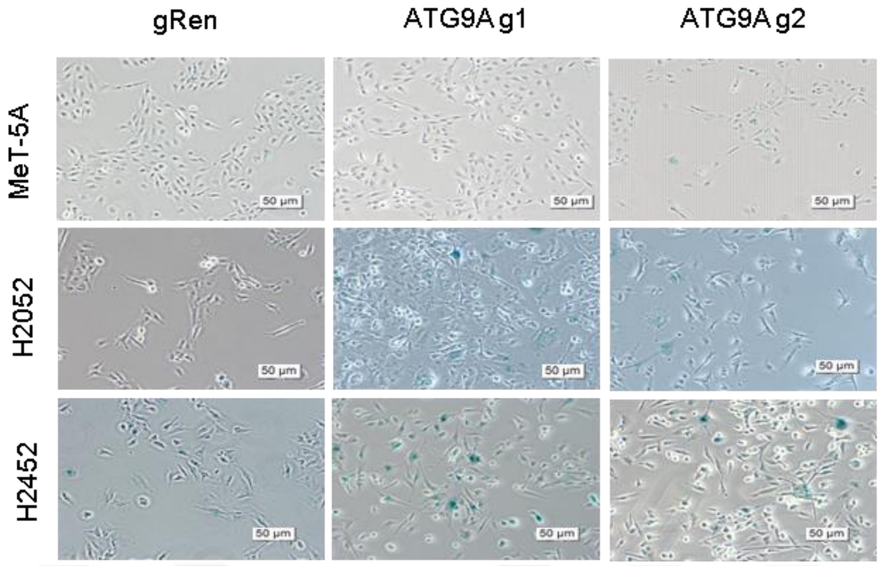

B

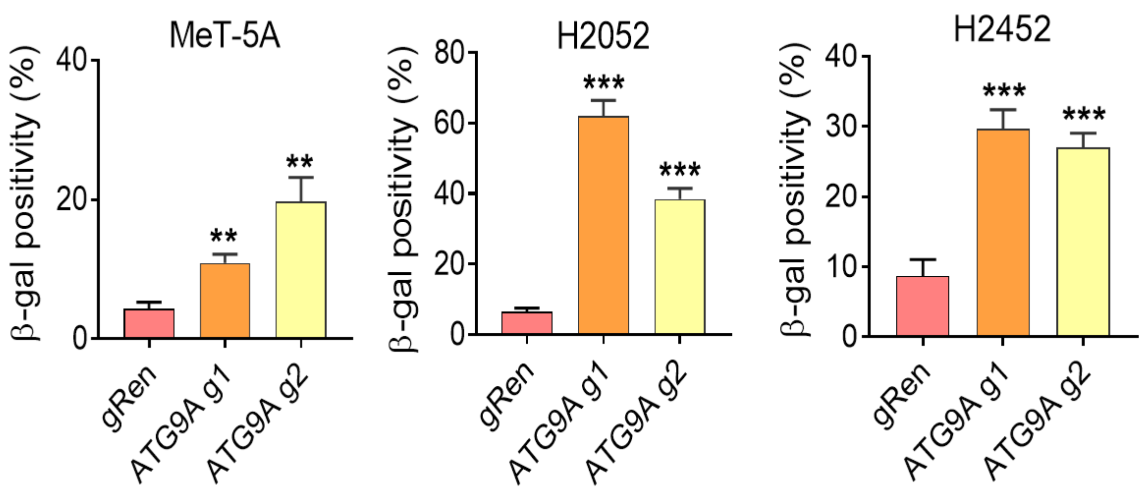

Figure 29: *ATG9A* deficient cells undergo cellular senescence. A) Representative images are shown. The images were captured at a 20X magnification, and the scale bar represents 50 εm. B) The quantification of SA-ɓ-gal positivity was determined by calculating the ratio of stained cells to the total cell number. The data is presented as mean ÑSD, with n=5. Statistical analysis was conducted using a one-way analysis of variance (ANOVA), and the significance levels were denoted as **p<0.01 and ***p<0.001.

4.8. *ATG9A* Knockout Induces Programmed Cell Death

Cell proliferation and apoptosis are typically regarded as antagonistic processes in cellular dynamics. However, intriguingly, under specific circumstances involving distinct stimuli or cellular conditions, they can occur simultaneously (63). Remarkably, in the context of *ATG9A* deleted cells, characterized by diminished proliferative and growth capabilities, the manifestation of an apoptotic phenotype became apparent, particularly after extended culture periods of up to two weeks. To experimentally investigate the presence of apoptosis, we conducted studies employing the Annexin V/Propidium iodide (PI) assay, a widely used technique to assess cell apoptosis and distinguish between early apoptotic, late apoptotic, and necrotic cells (64). Additionally, we performed a western blot analysis targeting cleaved Caspase 3 and cleaved PARP, well-established molecular markers for apoptosis. Specifically, Caspase 3 is an essential executor caspase involved in the proteolytic cascade during apoptosis, while PARP plays a role in DNA repair and maintenance of genomic integrity (65,66). The results of the Annexin V/PI staining demonstrated that *ATG9A* knockout led to an increase in apoptosis in MPM cell lines. Intriguingly, however, the MeT-5A cell line exhibited consistent apoptosis rates across all gRNAs infected (Figure 30). Further supporting these findings, the western blot analysis revealed increased band intensities of cleaved Caspase 3 and cleaved PARP in *ATG9A* depleted H2052 and H2452 cells compared to the gRen control cells. In striking contrast, no significant changes were observed in the MeT-5A cell line (Figure 31).

A

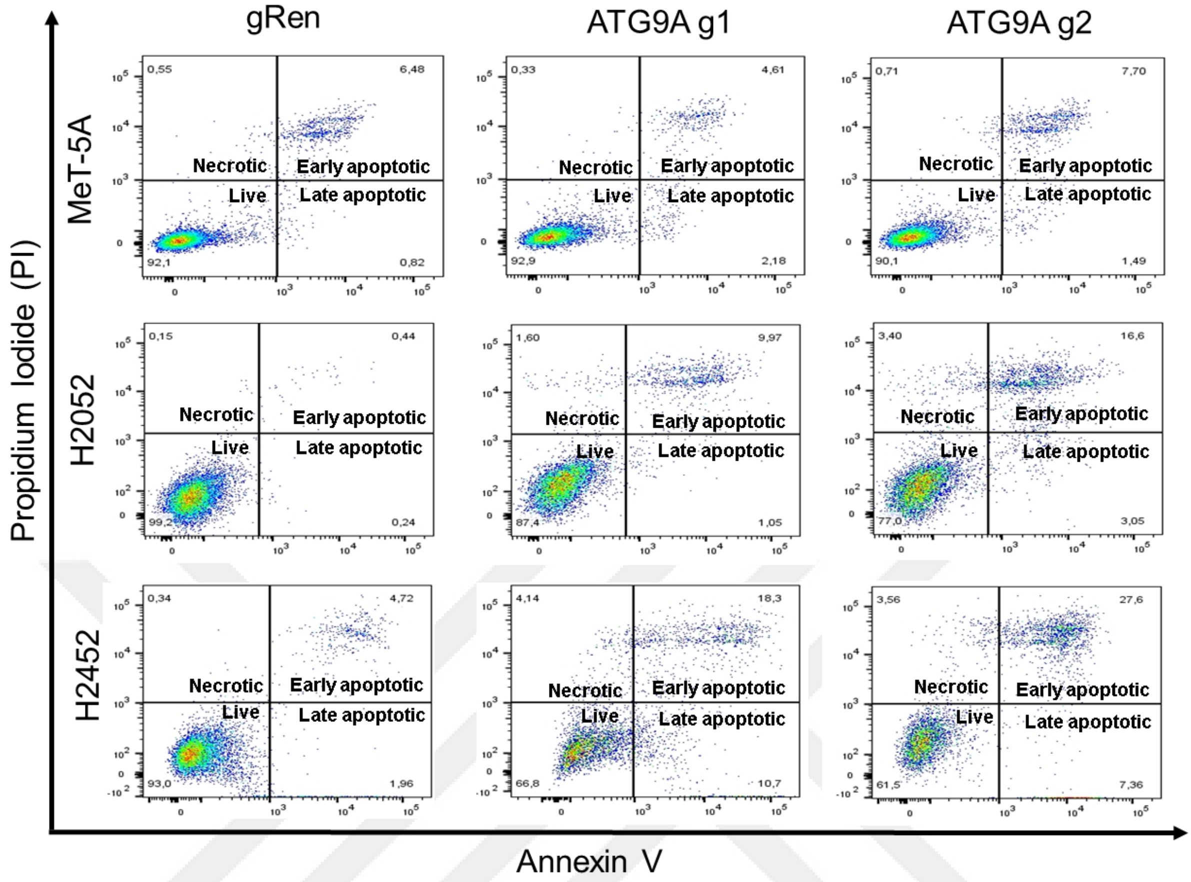
gRen
ATG9A g1
ATG9A g2
MeT-5A
H2052
H2452
Propidium Iodide (PI)
Annexin V
Necrotic
Early apoptotic
Live
Late apoptotic
0,55
6,48
92,1
0,82
0,33
4,61
92,9
2,18
0,71
7,70
90,1
1,49
0,15
0,44
99,2
0,24
1,60
9,97
87,4
1,05
3,40
16,6
77,0
3,05
0,34
4,72
93,0
1,96
4,14
18,3
66,8
10,7
3,56
27,6
61,5
7,36

B

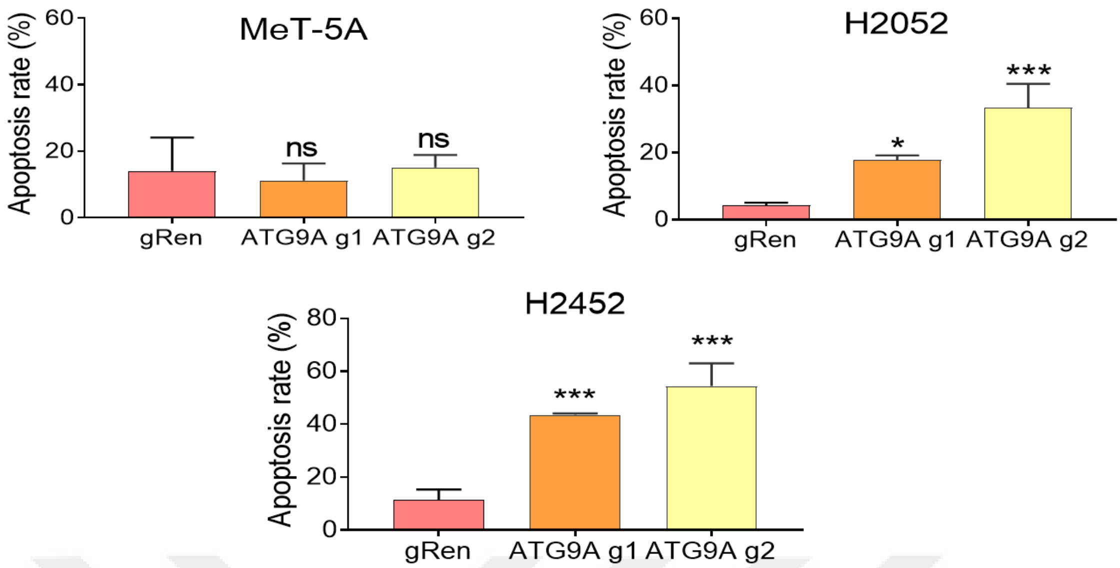

Figure 30: *ATG9A* knockout induces apoptosis in MPM cell lines. Representative plots from three independent Annexin V/PI staining assays are presented. The plots are divided into four quadrants, each labeled to indicate live, necrotic, early apoptotic, and late apoptotic cells. Apoptosis rates were calculated by summing the rates of early and late apoptosis. The data is presented as mean ÑSD, with n=3. Statistical analysis was conducted using a one-way ANOVA, and significance levels are shown as *p<0.05 and ***p<0.001. "ns" indicates no significant difference.

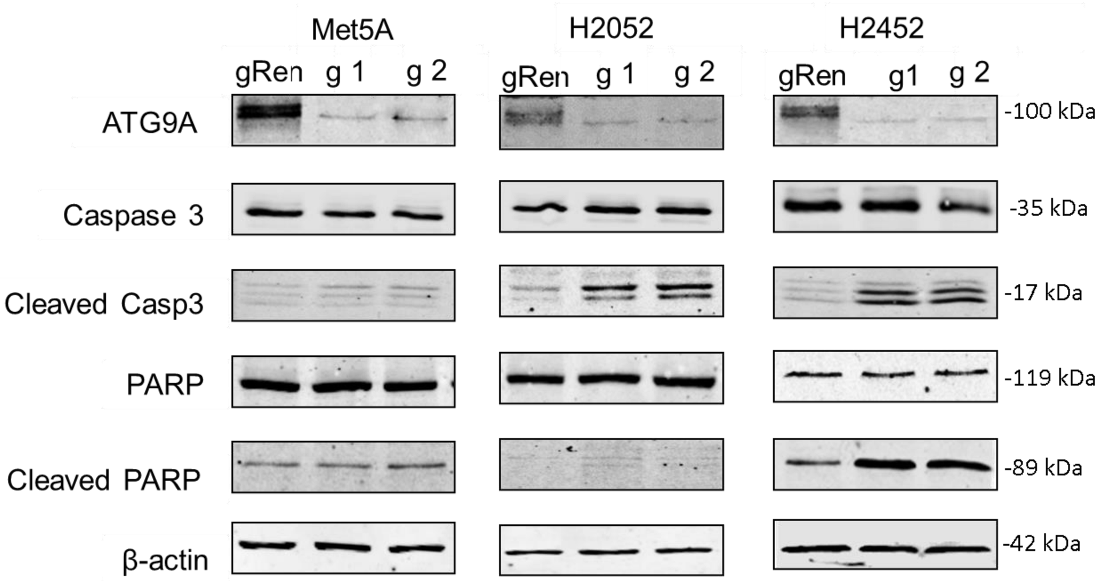

Figure 31: *ATG9A* knockout increases the cleavage of Caspase 3 and PARP in MPM cell lines. Antibodies against Caspase 3, cleaved Caspase 3, PARP, cleaved PARP, and ATG9A were used. **β**-actin was used to ensure accurate normalization of the protein levels.

4.9. Apoptotic Cell Death in *ATG9A* Knockout Cells is Associated with ROS Accumulation and DNA Damage

4.9.1. ATG9A Gene Silencing Causes DNA Damage

Apoptotic cell death is a highly regulated process essential for the removal of damaged or unwanted cells. Various stimuli, including DNA damage, cellular stress, and oxidative stress, can trigger apoptosis (67). In the context of DNA damage, apoptosis serves as a protective mechanism, preventing the survival and propagation of cells harboring severe DNA lesions (68). Given our previous findings linking *ATG9A* gene depletion to increased cell death, we sought to investigate the molecular mechanism underlying the observed increase in cell death upon *ATG9A* gene depletion. To achieve this, we initially conducted immunofluorescence staining using a specific marker, ɔH2AX, which is a widely accepted marker of DNA lesions. Double-strand breaks induce phosphorylation of the serine 139 residue at the C-terminal of Histone H2AX, leading to its conversion into ɔH2AX (69). Our results revealed enhanced ɔH2AX staining in *ATG9A* depleted cells, suggesting that *ATG9A* ablation induces DNA damage in cancer cell lines. Conversely, no discernible staining was observed under any conditions in the MeT-5A cell line, serving as a negative control (Figure 32).

A

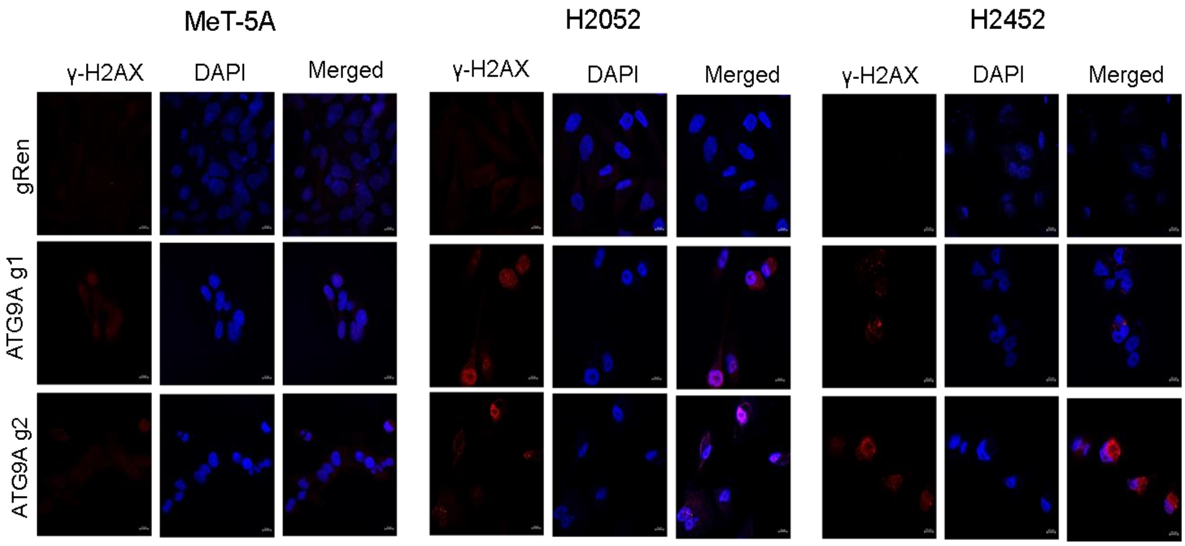

B

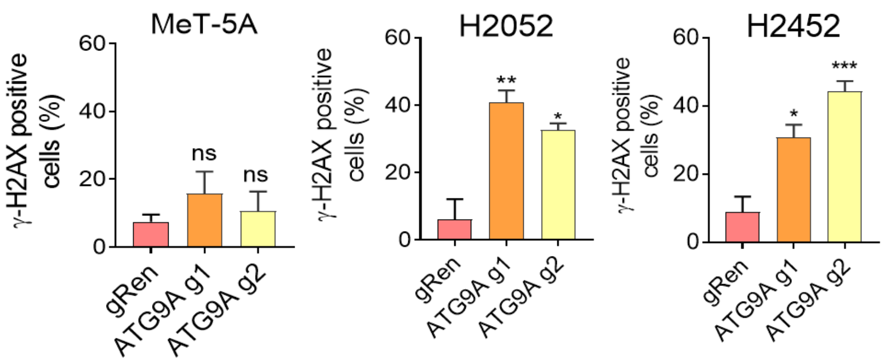

Figure 32: *ATG9A* knockout induces ɔH2AX accumulation in MPM cell lines. A) The stainings of ɔH2AX (red) and DAPI (blue) were visualized under a confocal microscope at a magnification of 63x. Scale bar, 10 Õm B) The number of ɔH2AX-positive and DAPI stained cells was quantified using ImageJ software. The total cell number was determined based on DAPI staining. The percentage of stained cells in the total cell number was calculated. The results are presented as the mean Ñ SD, with n=10. Statistical significance was determined using a One-way ANOVA test, and significance levels were indicated as *p<0.05, **p<0.01, and ***p<0.001. "ns" indicates no significant difference.

To provide further evidence for our findings, we conducted an alkaline comet assay, a variation of the comet assay specifically designed to detect and quantify DNA single-strand breaks (70). This assay is based on the principle that single-strand breaks can be visualized when exposed to alkaline conditions, as they cause the DNA fragments to migrate away from the cell nucleus. In this assay, we embedded the cells in agarose gel on a microscope slide and subjected them to gel electrophoresis under alkaline conditions. Under such conditions, the DNA fragments with single-strand breaks or alkali-labile sites migrated more extensively from the nucleus compared to intact DNA. This migration resulted in the characteristic comet-like appearance, with the DNA fragments forming the "tail" extending away from the "comet head", which represents the undamaged DNA still retained in the nucleus. Upon analyzing our results, we observed intact DNA under all conditions of the MeT-5A cells, indicating the absence of significant DNA damage. Unlike MeT-5A cells, we found varying degrees of DNA damage in *ATG9A* depleted H2052 and H2452 cells (Figure 33 A). The comet tail length increased from 5% in gRen control to 40-50% in *ATG9A* knockouts in H2052 cell. The comet tail length in H2452 cell increased from 3% in gRen control to 20-30%

in *ATG9A* silenced cells. MeT-5A remained at 30% in all conditions, there was no change between control and *ATG9A* silenced cells (Figure 33 B). These results support our previous findings that *ATG9A* gene deletion is associated with DNA damage in MPM cell lines. The alkaline comet assay specifically detected and quantified the single strand breaks that occurred as a result of *ATG9A* ablation.

A

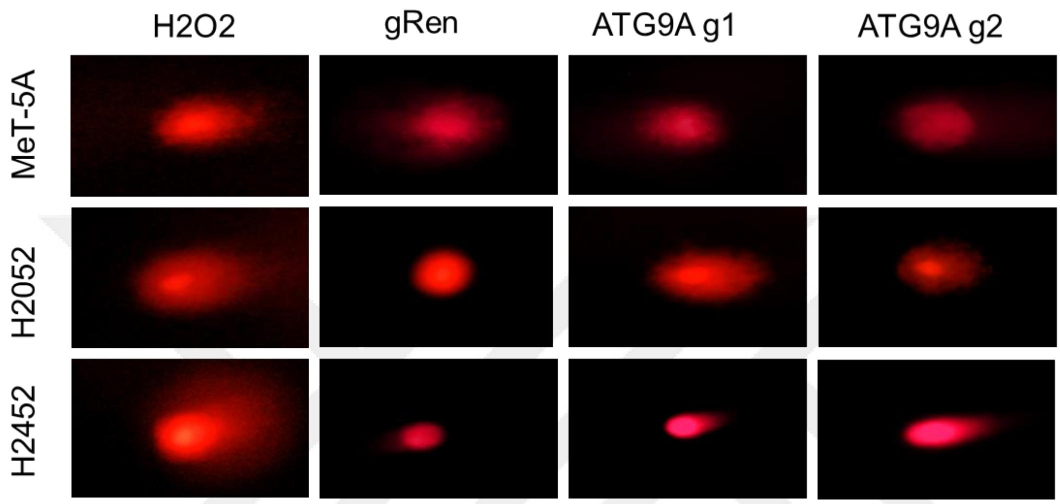

B

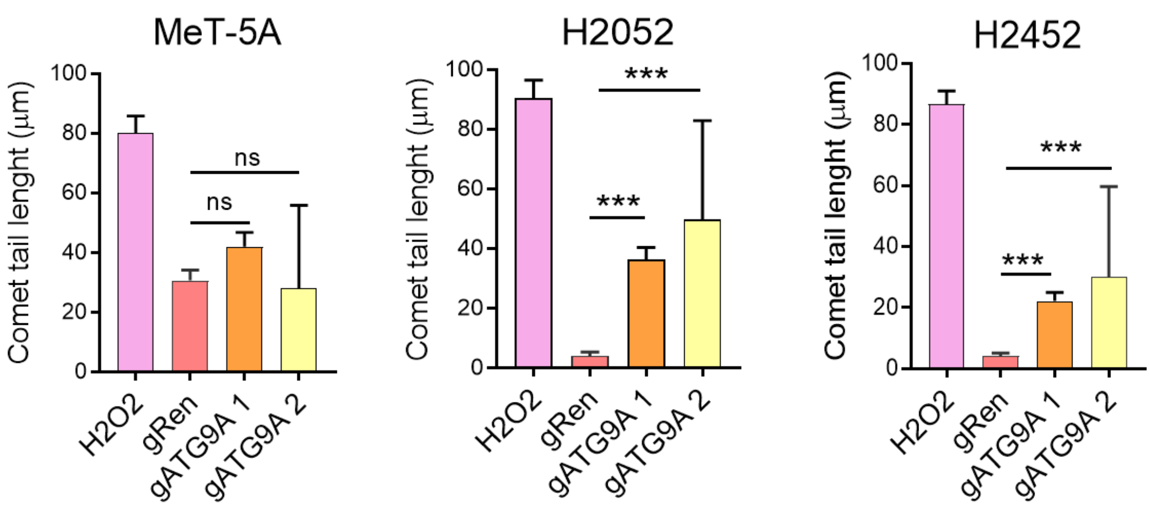

Figure 33: Alkaline comet assay in MeT-5A, H2052 and H2452 cell lines. A) DNA was stained with propidium iodide and fluorescence microscope images were captured at 10X magnification. Hydrogen peroxide (H2O2, 50 ÕM) was used as a positive control to induce oxidative DNA lesions. B) Comet tail lengths (Õm) were measured using the ImageJ OpenComet plugin. The data is presented as mean Ñ SD, with a sample size

(n) of 50. Statistical analysis was conducted using a two-way ANOVA, followed by multiple comparisons. The significance level is ***p<0.001. "ns" stands for no significant difference.

4.9.2. ATG9A Gene Depletion Leads to ROS Accumulation

The close relationship between DNA damage and reactive oxygen species (ROS) is well-established. ROS, which encompass free radicals and other reactive molecules, have the potential to induce various types of DNA damage. This can occur through direct chemical reactions with DNA or indirectly by influencing cellular processes involved in maintaining DNA integrity (71). To quantify the levels of ROS, a chemical called DCFDA was employed. When introduced into the cell, this compound undergoes oxidation by ROS, resulting in the production of a green fluorescent substance known as DCF (dichlorofluorescin). Through this approach, the quantity of ROS accumulation can be measured using either a fluorescent microscope or a spectrofluorimetric assay (72). In line with this information, we demonstrated a strong increase in the amount of ROS levels in *ATG9A* deleted cancer cells using both fluorescent microscopy (Figure 34A) and spectrofluorimetric assay (Figure 34B). Importantly, no difference was reported between the control and *ATG9A* ablated cells in MeT-5A (Figure 34).

A

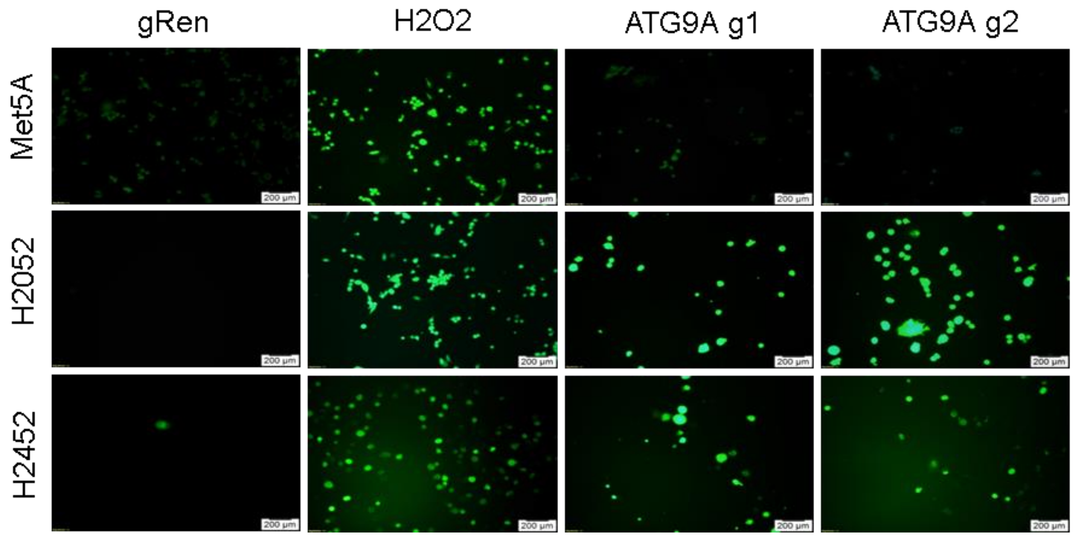

B

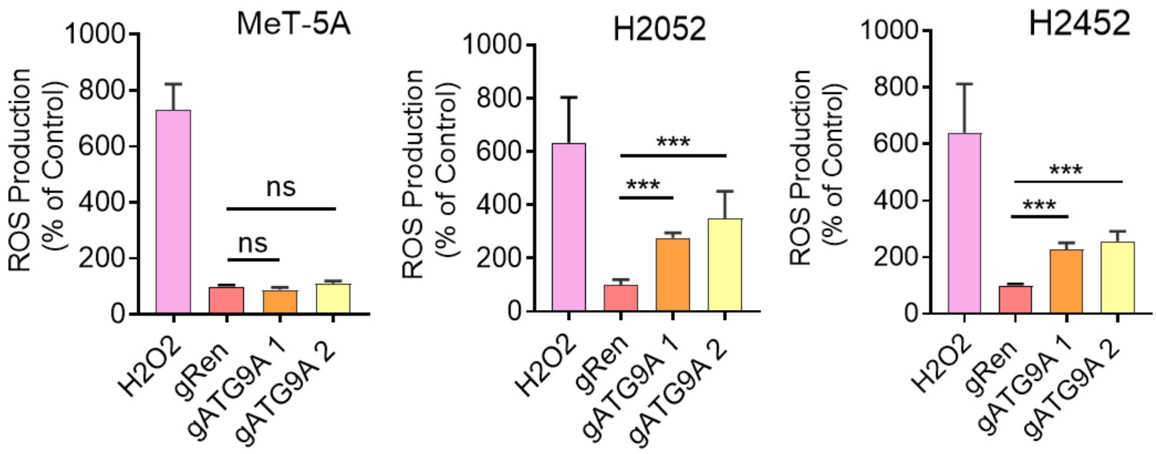

Figure 34: DCFDA assay in MeT-5A, H2052 and H2452 cells. A) Representative images are shown. Hydrogen peroxide (H2O2) was employed as a ROS inducer at a concentration of 50 ÕM. B) The ROS levels in gRen samples were normalized to 100 across all cell lines. The ROS levels in other cells were adjusted proportionally to gRen. The data is shown as mean Ñ SD, with n=3 replicates. Statistical significance was calculated by two-way ANOVA, with multiple comparisons. Significance values are shown by ***p<0.001. "ns" indicates no significant difference.

NADPH oxidases (NOX) represent a family of enzymes that play a crucial role in the generation of reactive oxygen species (ROS) as an integral part of their physiological function. These NOX enzymes facilitate the transfer of electrons across cellular membranes, harnessing NADPH as a vital source of reducing equivalents. This electron transfer process culminates in the generation of superoxide radicals, subsequently leading to the production of other ROS species. NOX isoforms, notably NOX1, NOX2 (also known as gp91phox), and NOX4, have demonstrated the ability to promote various cancer-related processes (73). In the context of assessing relative gene expression levels of ROS markers, via qRT-PCR, our data revealed an upregulation in the relative expression levels of NOX1 and NOX4 in *ATG9A* knockout cells when compared to the gRen control cells (Figure 35).

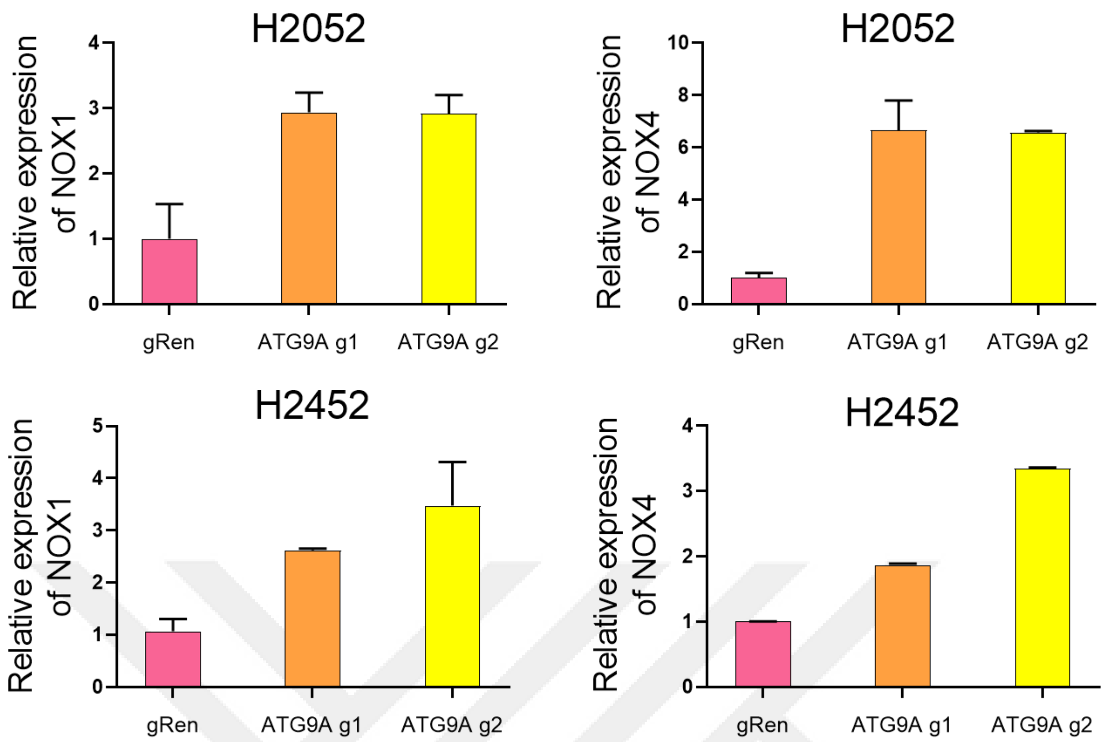

Figure 35: Transcript levels of NOX1 and NOX4 enzymes in *ATG9A* sufficient and deficient H2052 and H2452 cells.

Following the observation of elevated levels of ROS, we proceeded to investigate the potential restoration of the phenotype associated with *ATG9A* silencing by inhibiting the rise in ROS levels. In this framework, we conducted a 2D colony formation experiment utilizing N-Acetyl-L-cysteine (NAC), a compound known for its ability to scavenge ROS (74). Remarkably, our findings demonstrated that the addition of 10 mM NAC to the cell culture medium effectively rescued the 2D colony formation ability in cancer cells depleted of *ATG9A* (Figure 36).

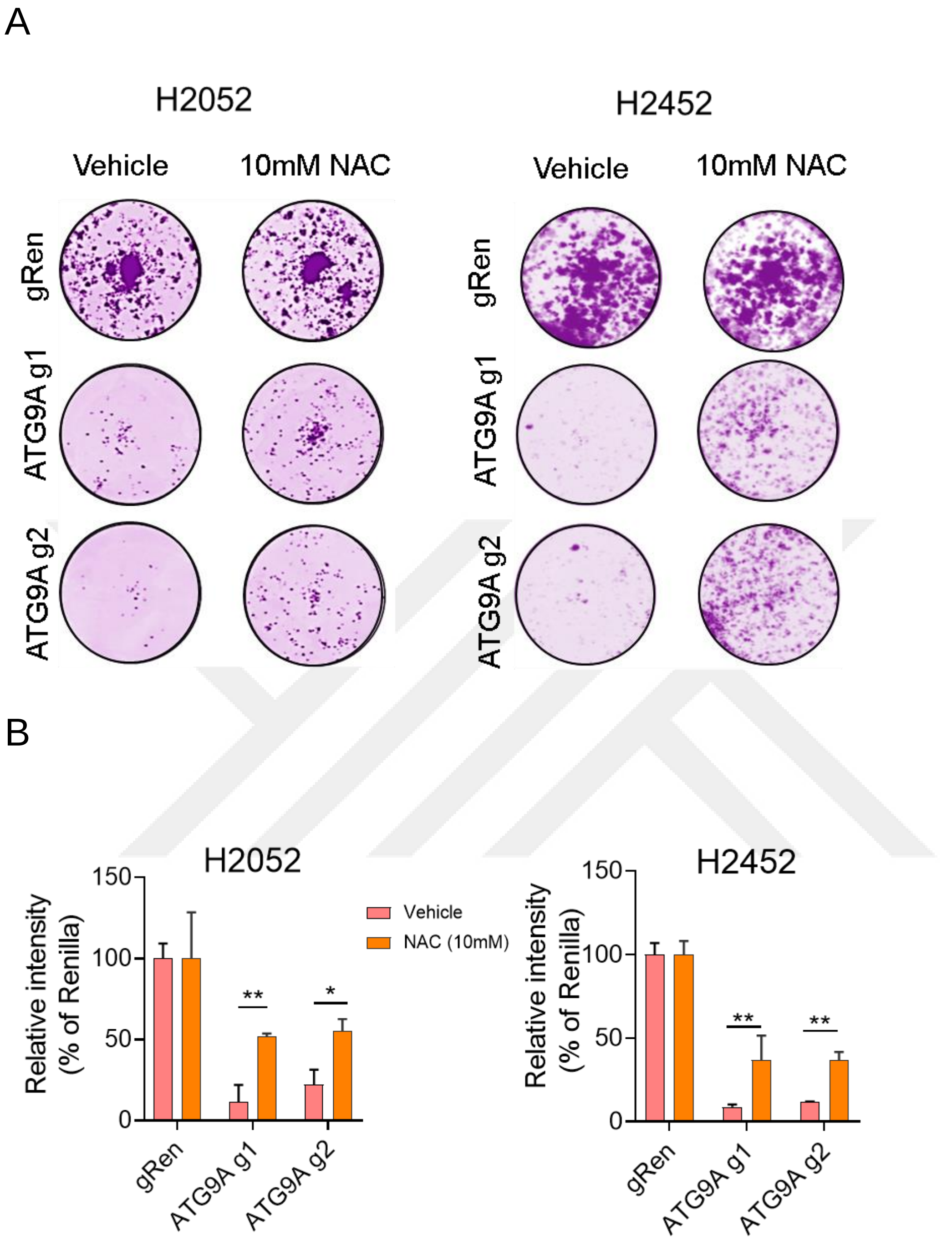

Figure 36: 2D colony formation phenotype in Vehicle (DMSO) or NAC (10 mM) treated *ATG9A* knockout H2052 and H2452 cells. A) Representative images from three replicates are shown. B) gRen control served as a reference and was normalized to 100 in both cell lines. The intensities of other conditions were normalized relative to the control. Statistical analysis was performed using a two-way ANOVA test. The data are shown as mean Ñ SD, with n=3. Significant differences are indicated using asterisks: *p<0.05, **p<0.01.

4.10. *ATG9A* Gene Silencing Disrupts Autophagy

Understanding the precise functions and regulatory mechanisms of ATG9A and autophagy is of great interest in the context of MPM cell biology. As we observed an increase in apoptosis and cellular senescence in *ATG9A* knockout H2052 and H2452 cell lines, we sought to investigate whether *ATG9A* depletion would affect autophagy. To assess this, we first examined the expression levels of the LC3 receptor, a critical player in autophagy, in both normal and starvation conditions using western blot analysis (Figure 37). Normally, LC3 I levels are higher under normal conditions and convert to LC3 II when autophagy is induced (75). As anticipated, we found that LC3 I was elevated in the gRen control and *ATG9A* knockout MeT-5A cells under normal conditions, while LC3 II was increased in the EBSS starvation condition. In H2052 and H2452 cell lines, LC3 I levels were higher in the gRen control under normal conditions, while LC3 II increased in the EBSS condition. Interestingly, in *ATG9A* knockout H2052 and H2452 cells, both LC3 I and LC3 II levels were elevated under both normal and starvation conditions.

To investigate whether this increase was associated with the accumulation of LC3 I and LC3 II in lysosomes due to impaired autophagy, we assessed the expression of p62, involved in LC3 I to LC3 II conversion and expected to decrease during normal autophagy, and Beclin 1 protein, expected to increase during autophagy (76). In the EBSS condition of *ATG9A* knockout H2052 and H2452 cells, we observed an increase in p62 protein levels, contrary to the expected decrease in normal autophagy. Additionally, the expression of Beclin 1 protein, anticipated to increase during autophagy, was decreased suggesting that the autophagy pathway is disrupted based on the observed differences in the functioning of autophagy proteins.

To further investigate the functionality of the autophagy process, we examined the formation of LC3 puncta using immunofluorescence staining. In normal conditions, the LC3 receptor forms few small puncta, whereas the number of puncta increases upon induction of autophagy. Accumulation of larger LC3 puncta indicates disruption of autophagy (77). Consistent with expectations, we observed small puncta formation in all gRNAs infected MeT-5A cells and in the gRen control of H2052 and H2452 cell lines, with an increased number of puncta in the EBSS starvation condition for these cell groups. Notably, we found that the *ATG9A* knockout H2052 and H2452 cell lines exhibited larger puncta compared to normal conditions (Figure 38). Enlarged box images have been provided to visualize the size of LC3 puncta more clearly.

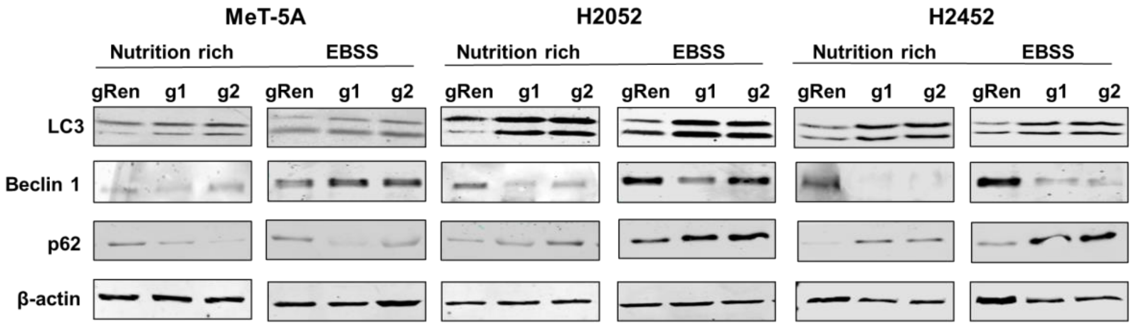

Figure 37: Expression levels of LC3, Beclin 1 and p62 proteins following *ATG9A* depletion in normal and starvation cell culture conditions. ɓ-actin was used as an internal control.

A

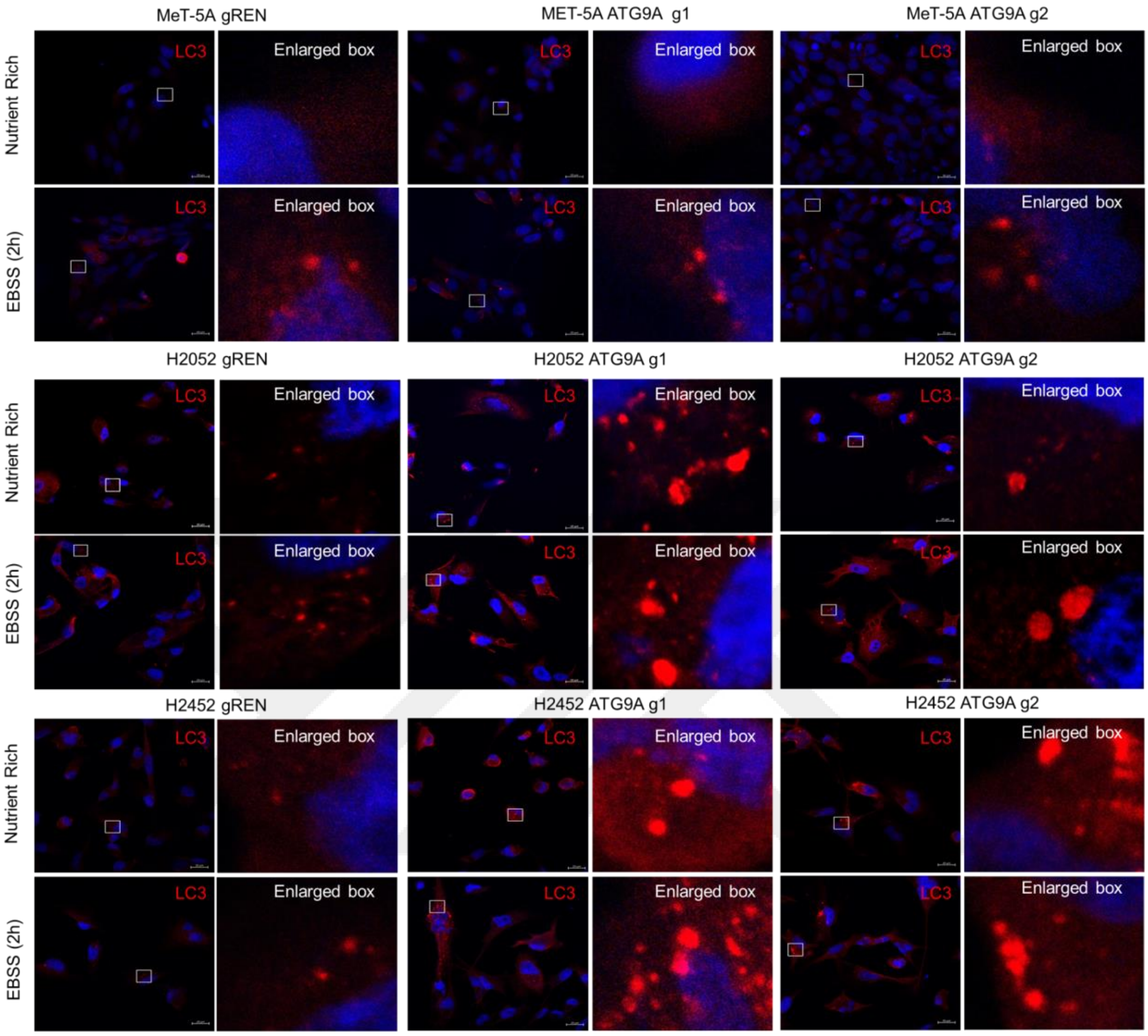

MeT-5A gREN
MET-5A ATG9A g1
MeT-5A ATG9A g2
Nutrient Rich
EBSS (2h)
LC3
Enlarged box
H2052 gREN
H2052 ATG9A g1
H2052 ATG9A g2
H2452 gREN
H2452 ATG9A g1
H2452 ATG9A g2

B

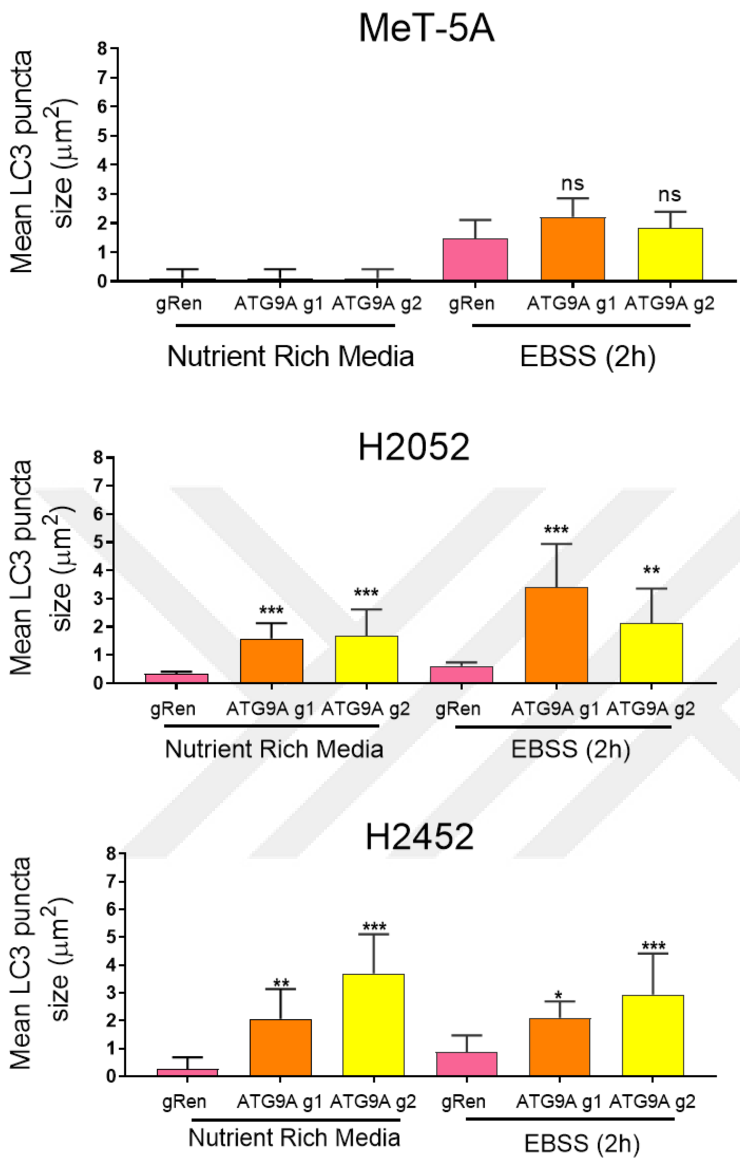

Figure 38: Immunofluorescent staining and quantification of LC3 puncta in *ATG9A* knockout or control cells under normal and starvation culture conditions (EBSS, 2h). A) Representative images are shown. LC3 (red) and DAPI (blue) stainings are obtained with a confocal microscope (magnification 40x). Scale bar, 20 Õm. The enlarged box images were formed by Zen software through the conversion of the squares drawn in the Zen program into the larger images of them. B) The mean size (Õm2) of LC3 puncta was calculated using ImageJ software. Data is presented as mean Ñ SD, with n=10. Statistical analysis was conducted using a one-way ANOVA, followed by multiple comparison tests. Significance levels are *p<0.05, **p<0.01, and ***p<0.001. "ns" indicates no significant difference.

4.11. *ATG9A* Ablation Causes Loss of Cancer Aggressive Phenotypes

4.11.1. ATG9A Knockout Reduces Cellular Motility

ATG9A has been implicated in the formation of lamellipodia, which are dynamic structures composed of actin filaments, which play a critical role in promoting cell migration. Studies have shown that depletion or inhibition of ATG9A can impair the speed and directionality of cell migration of various cell types, including cancer cells and neuronal cells (78). To investigate the potential influence of ATG9A on cancer aggressive phenotypes, we conducted a wound healing assay to assess cellular motility. In this experiment, cells were seeded in 6-well plates and allowed to reach 80% confluency. Subsequently, a wound was created using a 200 εL pipette tip, media with % 2 FBS was added, and images were captured immediately after the scratch was made (0 hr), as well as at 24 hrs and 48 hrs using a light microscope. Our results revealed that depletion of the *ATG9A* gene led to a reduction in cellular motility. Specifically, the ability of cancer cells to migrate and close the wound was significantly impaired upon *ATG9A* depletion. However, *ATG9A* depletion did not exhibit any significant effect on the cellular motility of mesothelial MeT-5A cells, indicating a context-dependent role of ATG9A in regulating cell motility (Figure 39).

A

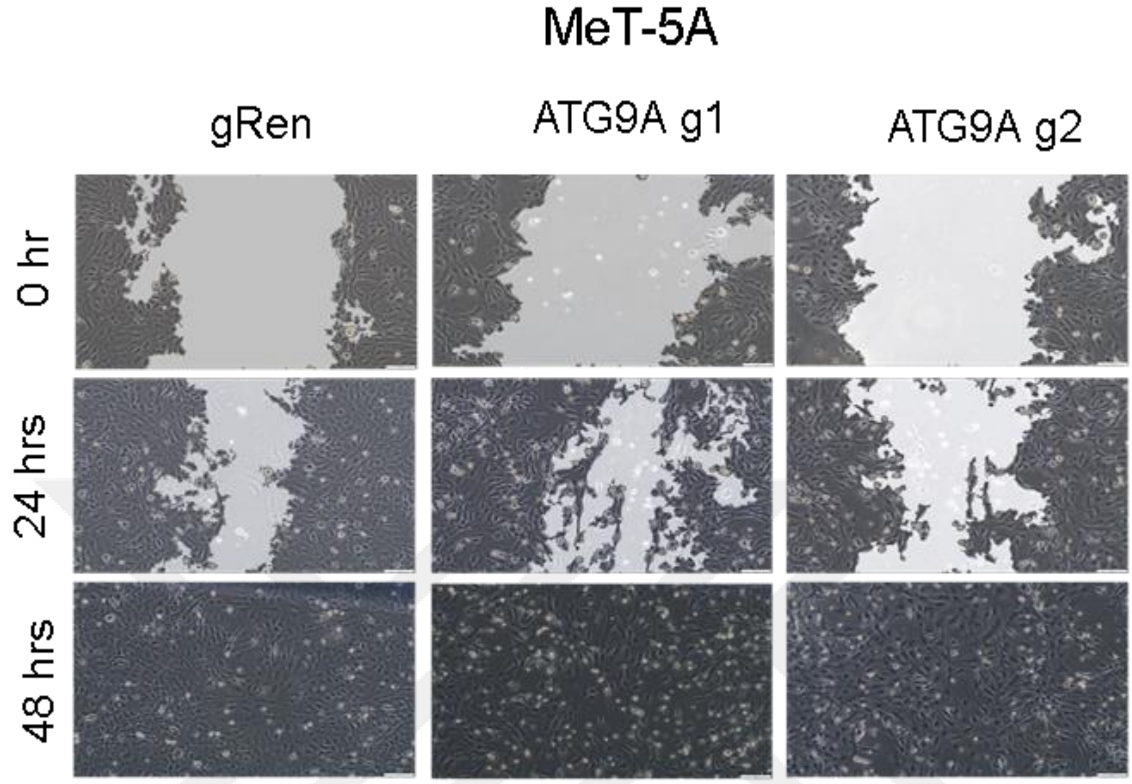

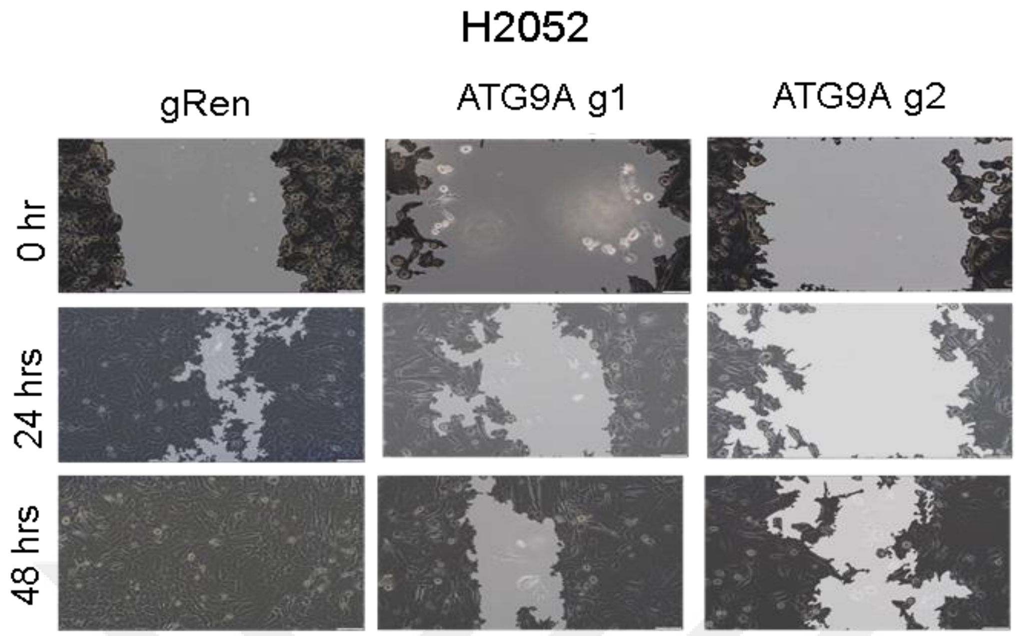
H2052
gRen
ATG9A g1
ATG9A g2
0 hr
24 hrs
48 hrs

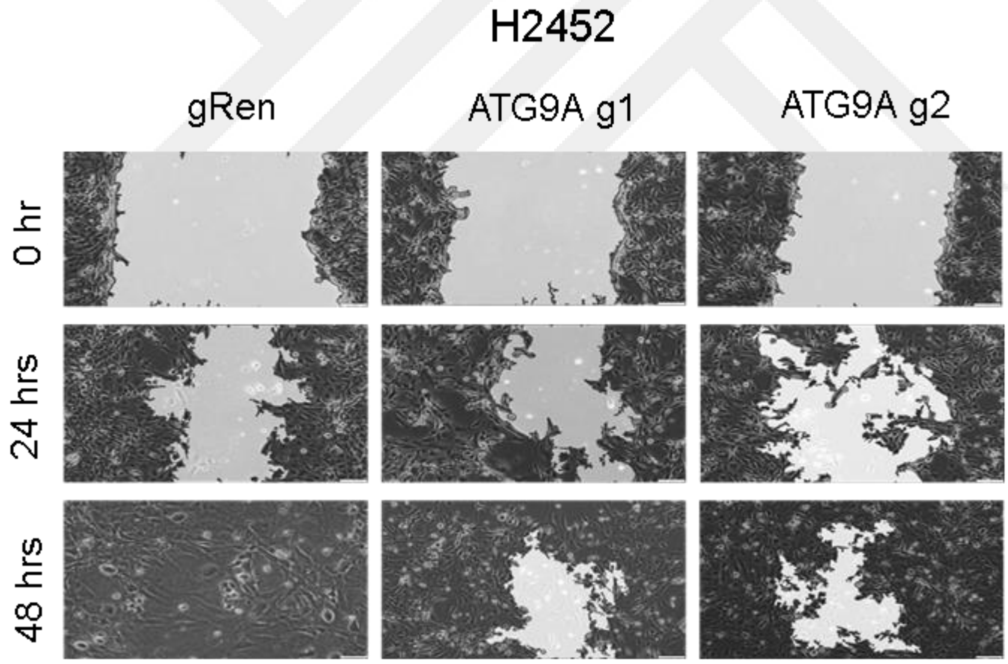
H2452
gRen
ATG9A g1
ATG9A g2
0 hr
24 hrs
48 hrs

B

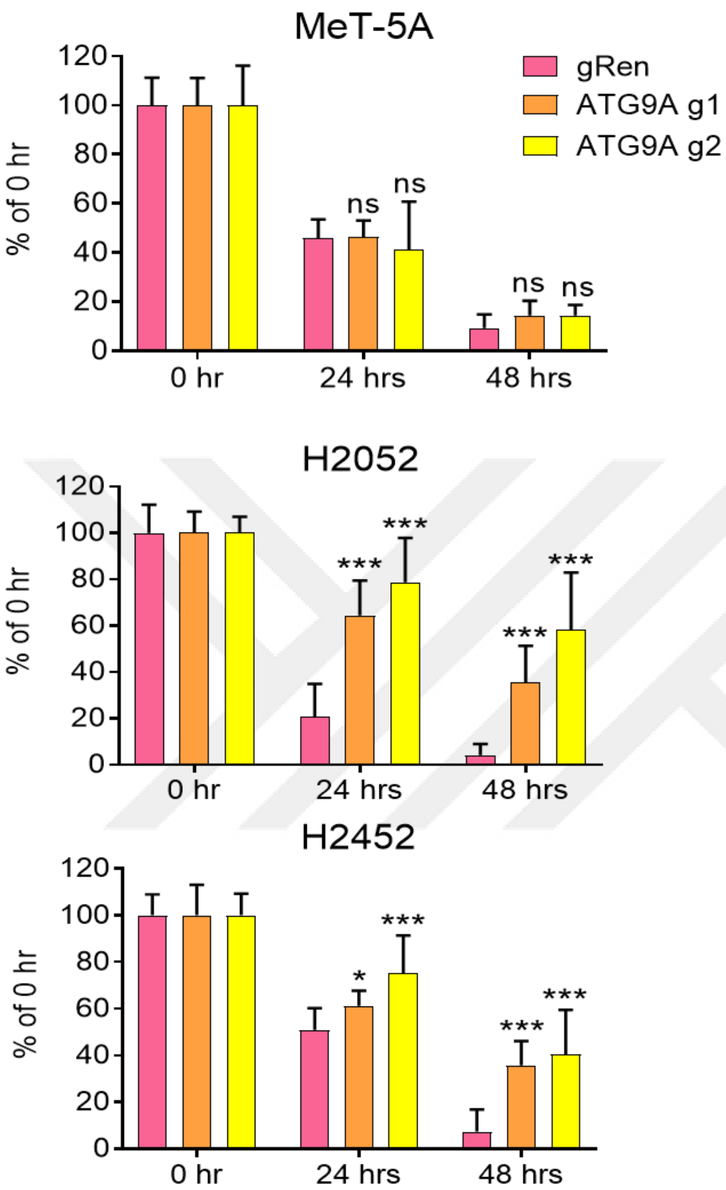

Figure 39: *ATG9A* ablation attenuates cellular motility in H2052 and H2452 cells. A) Representative images are selected from three replicates. B) Wound areas were measured using ImageJ software/MR_Wound_Healing plugin (79). Wound area was calculated relative to percentage of day 0. Magnification (10X), scale bar, 100 εm. Mean Ñ SD, n=5, *p<0.05, ***p<0.001, ns: not significant, Two-way ANOVA, multiple comparison.

4.11.2. ATG9A Knockout Reduces the Migration Capacity of MPM Cells

After characterizing the impact of ATG9A on cellular motility in the wound healing assay, our objective was to evaluate its influence on cell migration in a controlled experimental setting, specifically employing the Boyden chamber assay (80). This assay entails seeding cells in the upper compartment of the Boyden chamber and permitting their migration through a porous membrane towards a chemoattractant present in the lower compartment. Following a 48-hour incubation period, migrated cells were subjected to crystal violet staining and subsequent imaging using a light microscope. Our observations unveiled a significant reduction in the migration capacity of cancer cells deficient in the *ATG9A* gene compared to the gRen control group (Figure 40). These findings provide additional evidence supporting the critical role of ATG9A in facilitating cell migration.

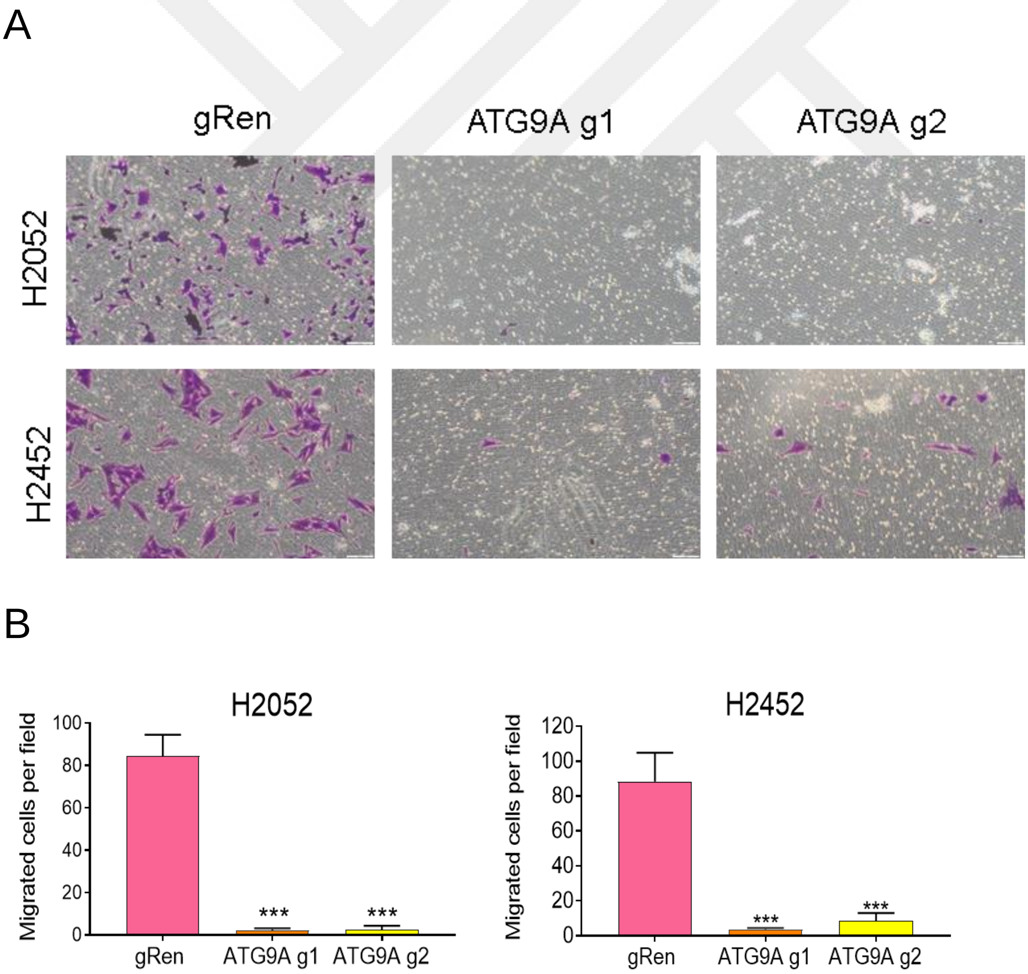

Figure 40: ATG9A is required for the migration ability of H2052 and H2452 cells. The Boyden Chamber Assay was conducted in duplicate. A) Representative images,

captured at 10X magnification with light microscope, are presented. Scale bar: 100 εm. B) The quantification of migrated cells was performed by manually counting cells in five randomly selected areas. Mean ÑSD, n=5, ***p<0.001, One way ANOVA.

4.11.3. ATG9A Knockout Reduces the Invasion Capacity of MPM Cells

Next, we investigated the potential role of ATG9A in the invasion capability of H2052 and H2452 cells. To realize this purpose, we utilized the Boyden chamber assay with a matrigel coating. The purpose of using matrigel is to simulate the extracellular matrix (ECM) environment, allowing us to study the cells' ability to invade through this barrier. After seeding the cells in the upper chamber, we allowed a 48 hrs incubation period, after which we stained the cells and captured their images using a light microscope. Our results demonstrated that depletion of *ATG9A* resulted in a significant reduction in the invasive capacity of the cancer cells (Figure 41).

A

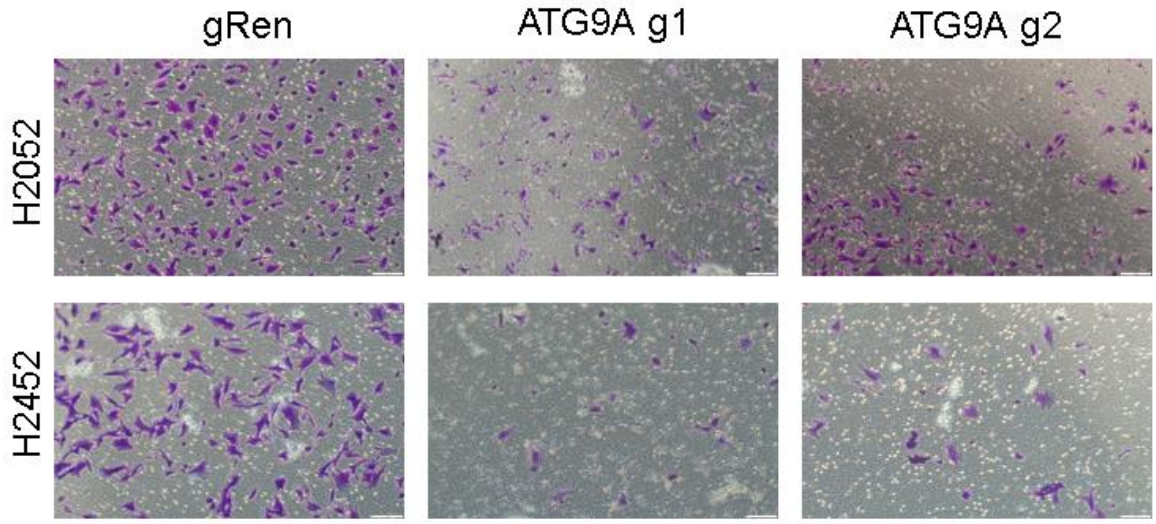

B

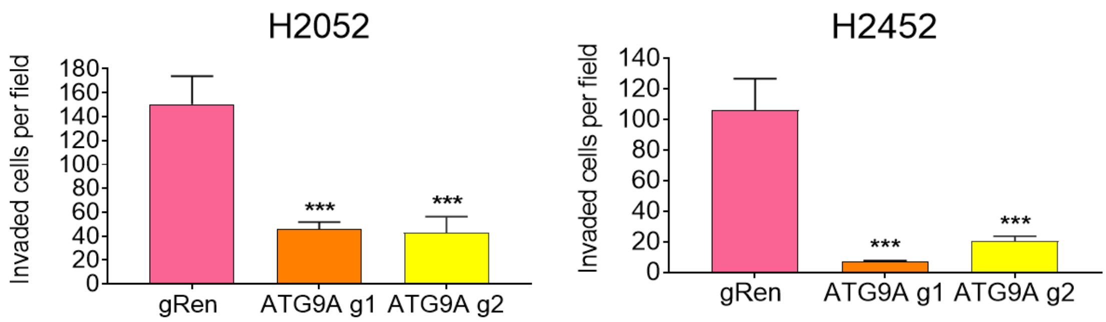

Figure 41: ATG9A is required for the matrigel invasion ability of H2052 and H2452 cells. The Boyden Chamber Assay was conducted in duplicate. A) Representative images, captured at 10X magnification with light microscope, are presented. Scale bar: 100 εm. B) The quantification of migrated cells was performed by manually counting cells in five randomly selected areas. Mean ÑSD, n=5, ***p<0.001, One way ANOVA.

Taken together, the reduced wound healing, migration, and invasion capacity observed upon *ATG9A* deficiency in all these assays supports its involvement in promoting cancer cell motility in MPM and highlights its potential as a target for modulating aggressive cancer phenotypes associated with disease progression.

4.12. Investigation of the Mechanism Underlying the Phenotypes Occurring in the Absence of *ATG9A* via Non-canonical Functions of ATG9A

4.12.1. The Absence of ATG9A Impedes Lipid Mobilization and Leads to Increase in Lipid Droplet Number

In our previous investigations, we have established that ATG9A, a protein crucial for phagophore expansion, plays a pivotal role in autophagy. It has been demonstrated that the absence of *ATG9A* impairs the autophagic process. However, ATG9A also exhibits a non-canonical function as highlighted in a study by Bonifacino and colleagues. This research revealed that ATG9A localizes in close proximity to mitochondria and facilitates the transportation of fatty acids from lipid droplets to the mitochondria. These transported fatty acids actively participate in mitochondrial respiration (53). To investigate this non-canonical function and examine the close localization of ATG9A and mitochondria, we conducted colocalization staining experiments. Specifically, we focused on the interaction between ATG9A and TOMM20, a key component of the mitochondrial outer membrane translocase complex (81). These experiments were performed under two conditions: starvation medium, where cellular lipid mobilization is required, and normal conditions. Our immunofluorescence findings revealed a close proximity between ATG9A and mitochondria (TOMM20), which became more pronounced in the starvation medium. (Figure 42). This suggests a potential role for ATG9A in facilitating the transport of fatty acids from lipid droplets to mitochondria under conditions of increased energy demand.

A

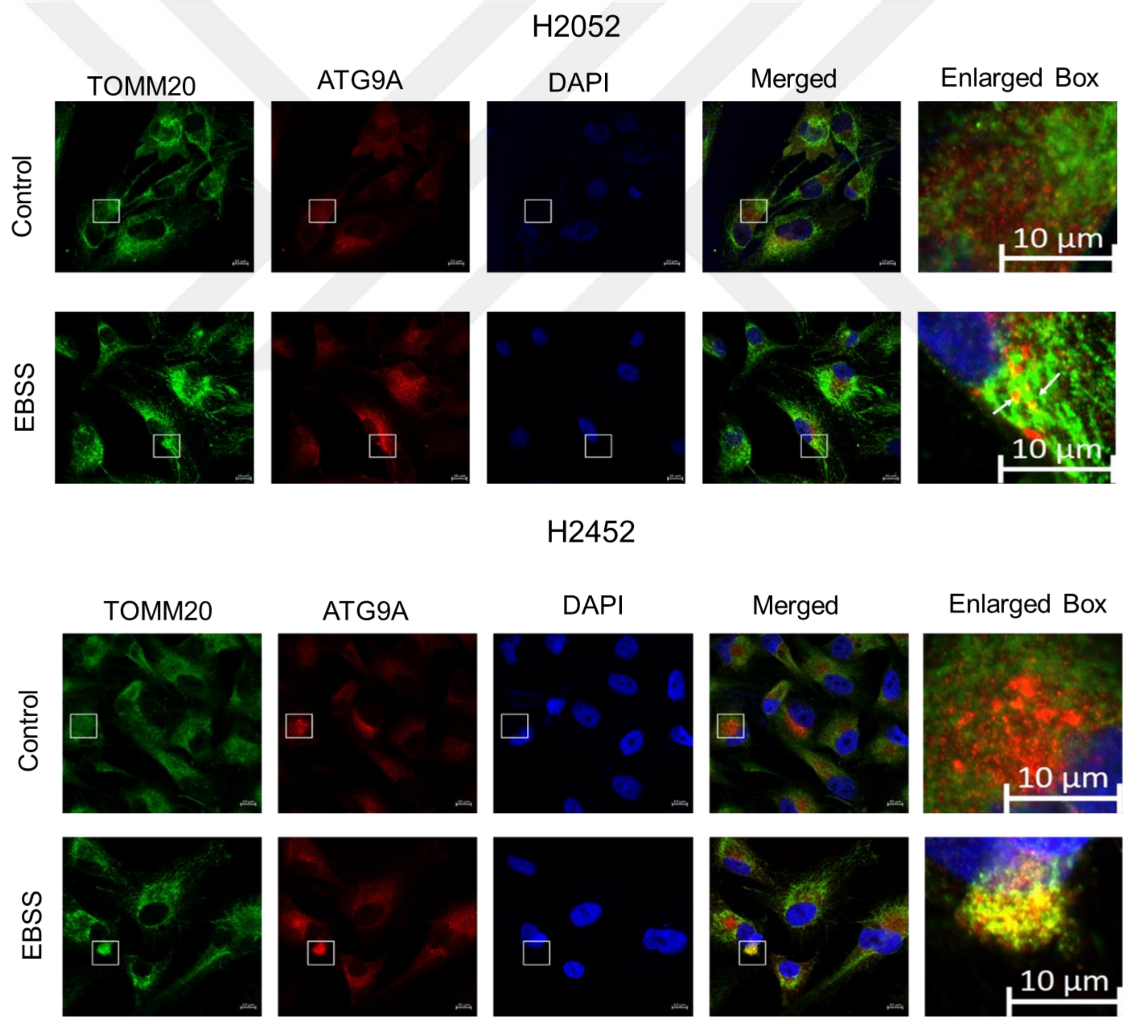

B

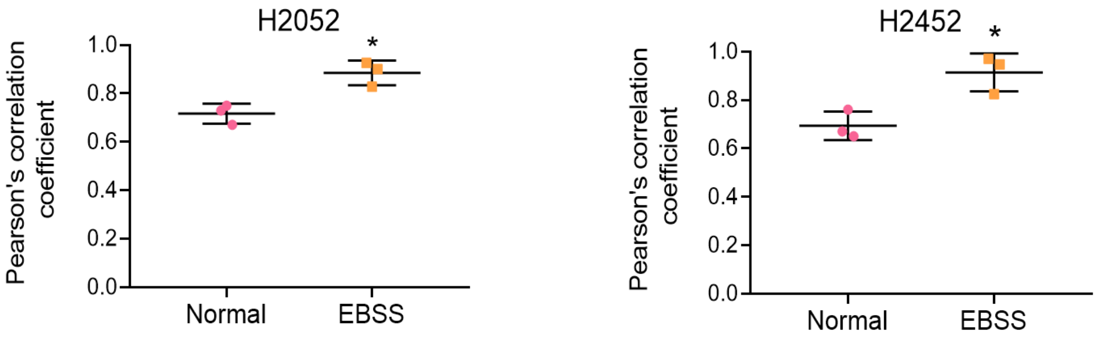

Figure 42: Immunofluorescent staining of H2052 and H2452 cell lines against TOMM20 and ATG9A proteins. A) Confocal microscopy images of TOMM20, ATG9A, and DAPI stainings were captured at a magnification of 63X. Scale bar: 10 Õm. Enlarged regions of interest were generated using the Zeiss Zen microscopy software. B) The Pearson's correlation coefficient was calculated using ImageJ/Fiji software to determine the degree of correlation between TOMM20 and ATG9A staining intensities and colocalizations. A correlation coefficient of 1 indicates a perfect positive correlation or a direct relationship between the two proteins.

Subsequently, we employed AUTODOT staining, a specific chemical dye that selectively binds to intracellular lipid droplets and enables their visualization under a fluorescence microscope (82). Our results demonstrated that gRen infected cells exhibited a significantly low number of lipid droplets, with some cells lacking observable droplets entirely. Conversely, in *ATG9A* ablated cancer cells, we observed an increased number of lipid droplets (Figure 43). This suggests that *ATG9A* depletion contributes to an accumulation of lipid droplets within the cells, potentially implicating ATG9A in the regulation of lipid metabolism or storage pathways in MPM cell lines.

A

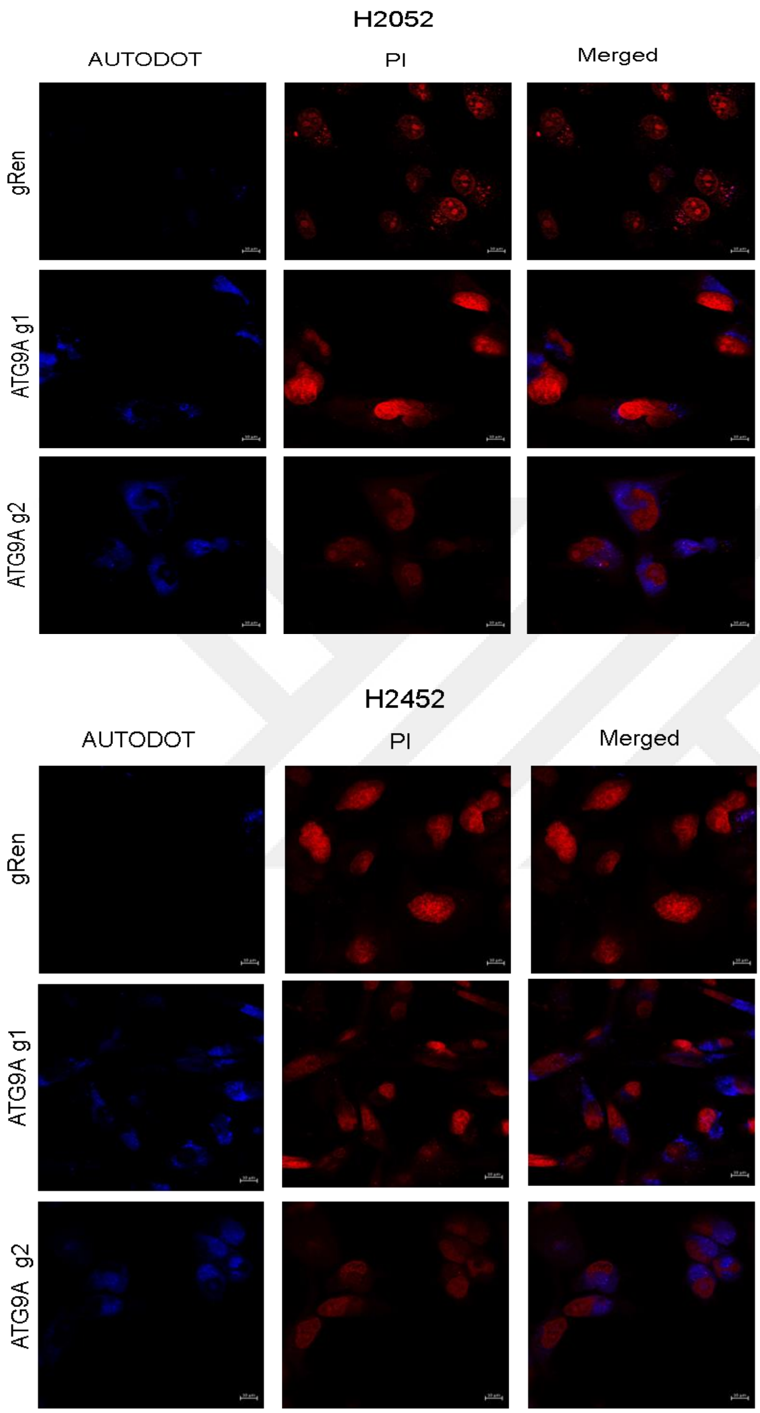
H2052
AUTODOT
PI
Merged
gRen
ATG9A g1
ATG9A g2
H2452
AUTODOT
PI
Merged
gRen
ATG9A g1
ATG9A g2

B

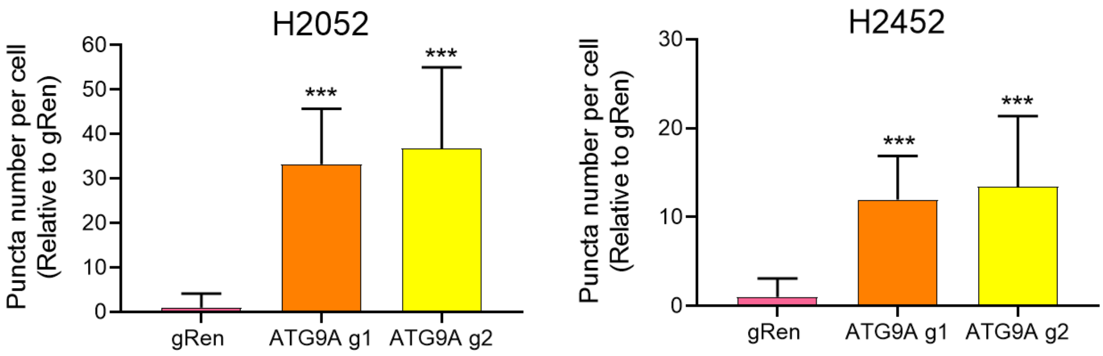

Figure 43: AUTODOT staining in both *ATG9A* sufficient and *ATG9A* deficient H2052 and H2452 cells. A) Representative images are shown. Images were acquired using a confocal microscope (magnification 63X). Scale bar: 10 Õm. Propidium iodide was used to counterstain the nucleus. B) The number of puncta (lipid droplets) per cell was quantified using ImageJ software. The data are presented as mean Ñ SD, with n=10. Statistical analysis was performed using one-way ANOVA, and ***p<0.001 indicates a significant difference.

4.12.2. Absence of ATG9A Has Detrimental Effects on Mitochondrial Structure and Impairs Mitophagy in MPM Cells

One of the non-canonical functions attributed to ATG9A is its involvement in initiating the process of mitophagy in conjunction with Optineurin (OPTN). It has been established that the OPTN-ATG9A complex is capable of initiating de novo synthesis of autophagic membranes on ubiquitin-coated damaged mitochondria (52). Building upon this knowledge, our initial objective was to investigate whether the deletion of *ATG9A* leads to mitochondrial damage. To assess mitochondrial structure, we employed MitoTracker staining, which allows for visualization of the mitochondrial morphology (83). Each cell has its own mitochondrial structure consisting of filaments. Although the appearance of the filaments varies from cell to cell, the length and structure of the networks can give an idea about whether the structure of mitochondria has deteriorated. For example, clumps of filaments mean that the structure of the mitochondria is disrupted. Following immunofluorescence staining, we observed significant alterations in the structural characteristics of the mitochondria (Figure 44). To gain a more comprehensive understanding, we further examined the outer mitochondrial membrane by staining with the TOMM20 antibody and conducted detailed analysis using the ImageJ/MiNa plugin. The Mitochondrial Network Analysis (MiNa) plugin allows for a detailed examination and quantification of mitochondrial morphology and dynamics, such as mean network size, mean branch length, and mitochondrial footprint, providing valuable insights into mitochondrial structure and function (84). Our results demonstrated a decrease in mean network size, mean branch length, and mitochondrial footprint in cancer cells lacking the *ATG9A* gene (Figure 45). These findings collectively indicate that the absence of *ATG9A* compromises the structural integrity of mitochondria.

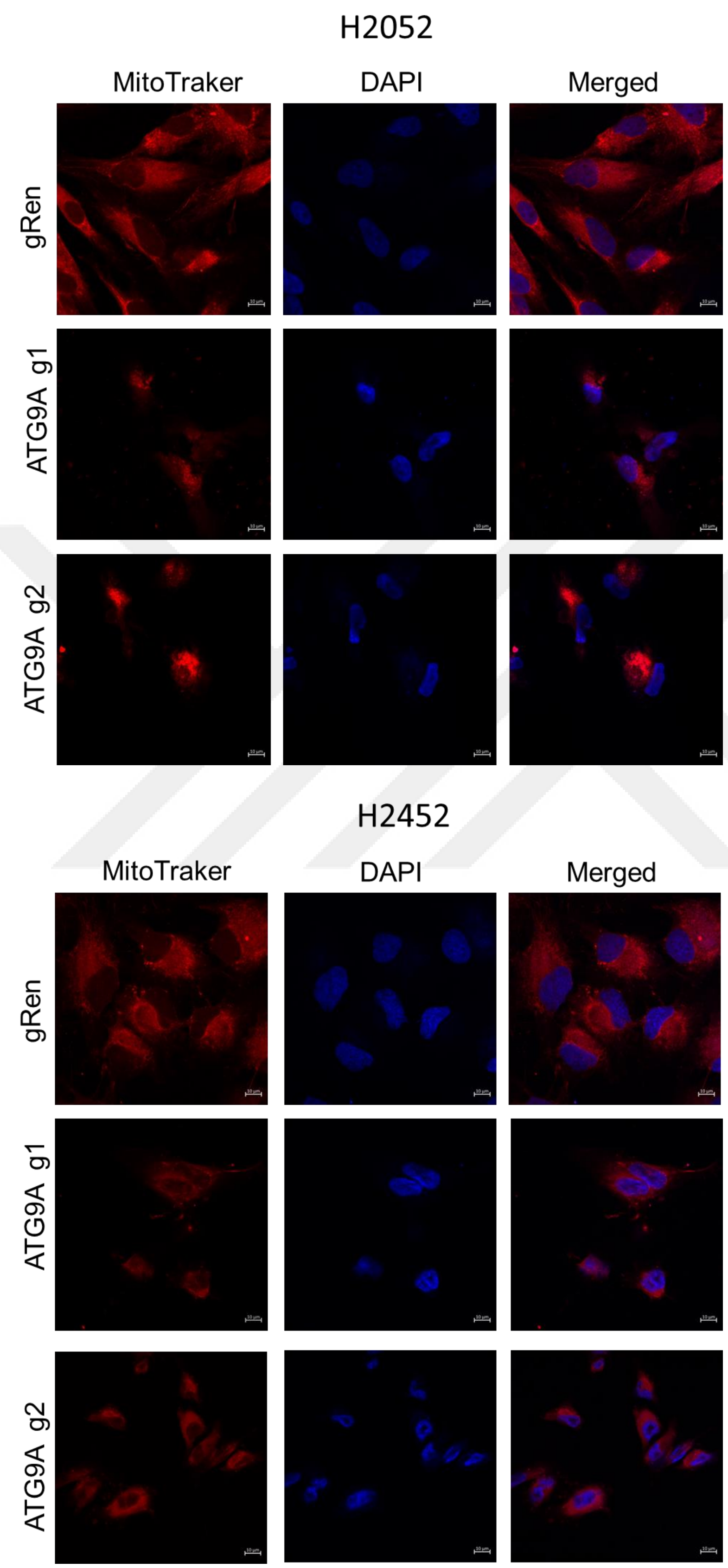

Figure 44: MitoTracker stainings in both *ATG9A* sufficient and *ATG9A* deficient H2052

and H2452 cells. DAPI was used as a counterstain for visualization of the cell nucleus. High-resolution images were captured under a confocal microscope with a magnification of 63X. Scale bar, 10 Õm.

A

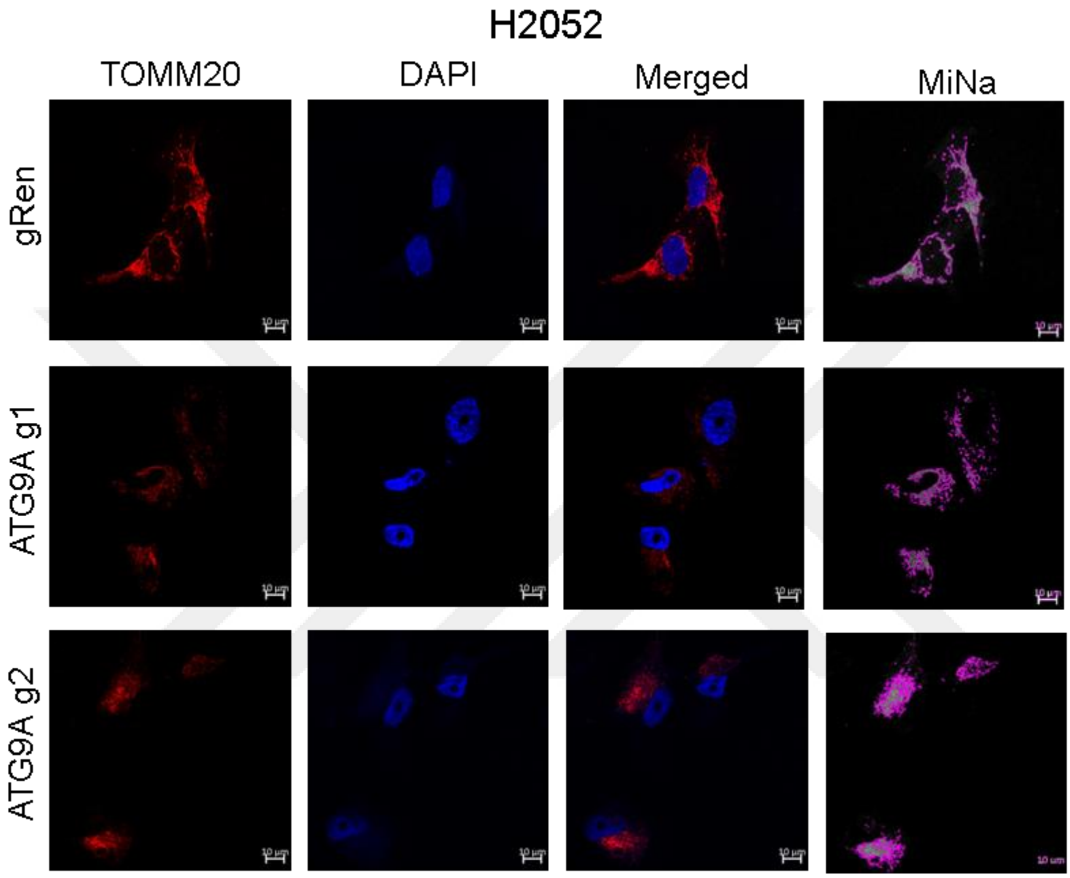

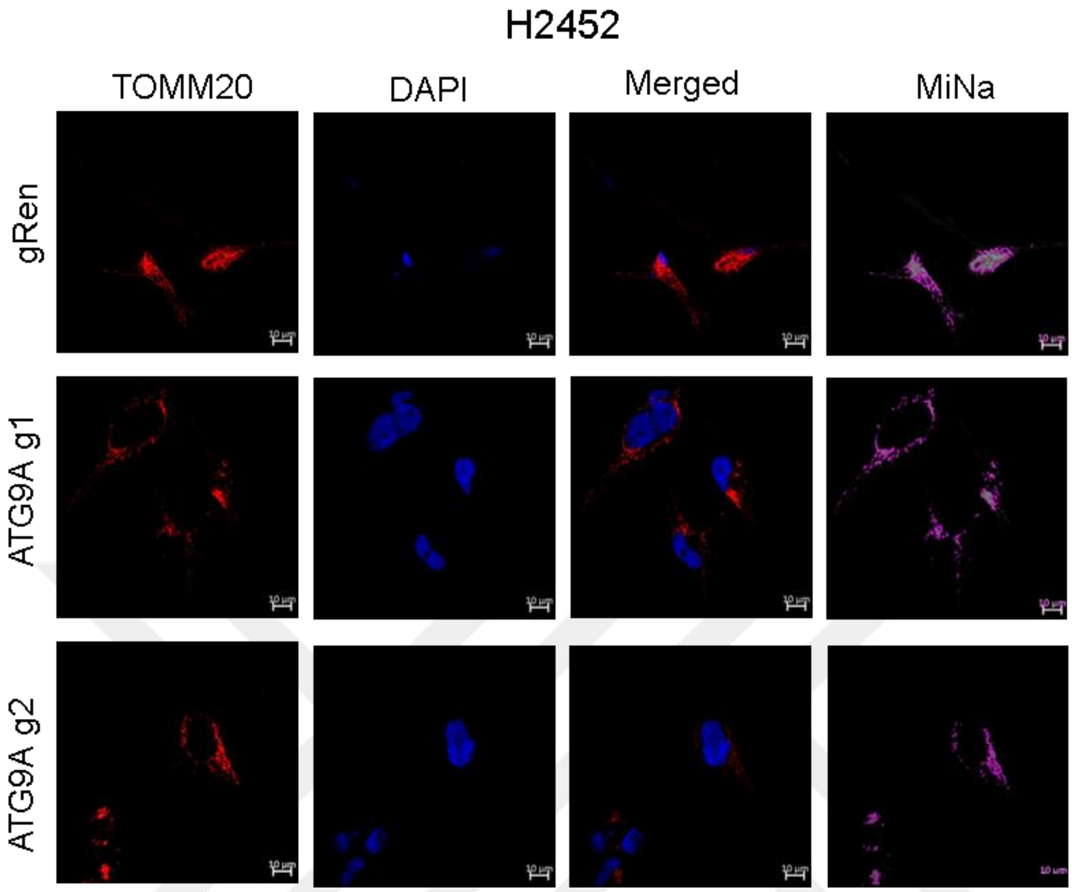

B

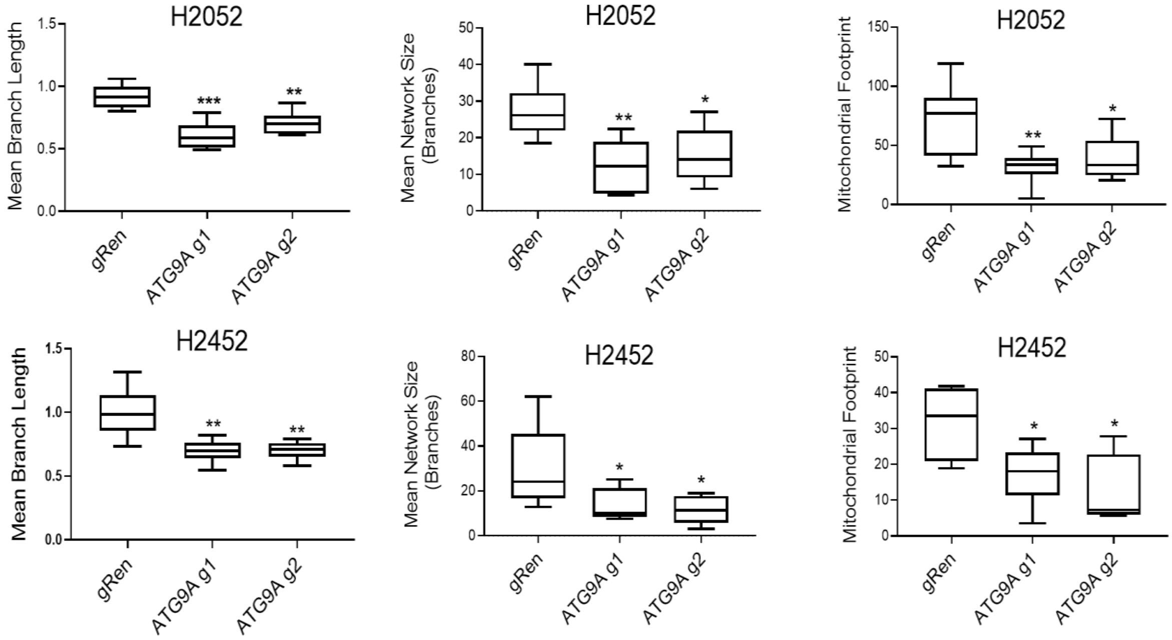

Figure 45: Immunofluorescent staining of TOMM20 in both *ATG9A* intact and *ATG9A*

deleted H2052 and H2452 cells. A) Images were acquired under a confocal microscope (Magnification, 63X). Counterstaining was achieved using DAPI to visualize the cell nuclei. Scale bar, 10Õm B) Quantification of mean branch length, mean network size, and mitochondrial footprint was carried out using the ImageJ/MiNa plugin. The data were presented as mean Ñ SD, with n=10. Statistical analysis was performed using one-way ANOVA, and significance levels were indicated as *p<0.05, **p<0.01, ***p<0.001.

To gain deeper insights into the involvement of ATG9A in initiating mitophagy via the OPTN axis, we employed the mt-mKeima plasmid-based mitophagy assay (85). This assay is a valuable tool for studying the process of mitophagy, particularly the selective degradation of mitochondria within lysosomes. The assay utilizes a pH-sensitive fluorescent protein called mKeima, which exhibits distinct emission spectra depending on the pH of the environment. The mKeima plasmid is transiently transfected into cells of interest, and upon expression, the mKeima protein localizes to the mitochondria. When mitochondria undergo mitophagy and fuse with lysosomes, the acidic pH within the lysosomes triggers a shift in the mKeima emission spectrum. Specifically, at a higher pH (cytoplasmic pH: 7), mKeima emits light in one wavelength range, while at a lower pH (lysosomal pH: 4.5), it emits light in a different wavelength range. By monitoring the emission spectra of mKeima using fluorescence microscopy or flow cytometry, researchers can distinguish between mitochondria present in the cytoplasm and those within lysosomes. This enables the quantification of mitophagy rates and the assessment of changes in mitophagy under various experimental conditions, such as genetic manipulations or exposure to mitophagy-inducing stimuli. Through this experimental approach, we demonstrated a notable reduction in the rate of mitophagy in *ATG9A* deleted cells, when compared to the gRen control group. Conversely, the mitophagy rate increased in the positive control cultured in EBSS medium (Figure 46).

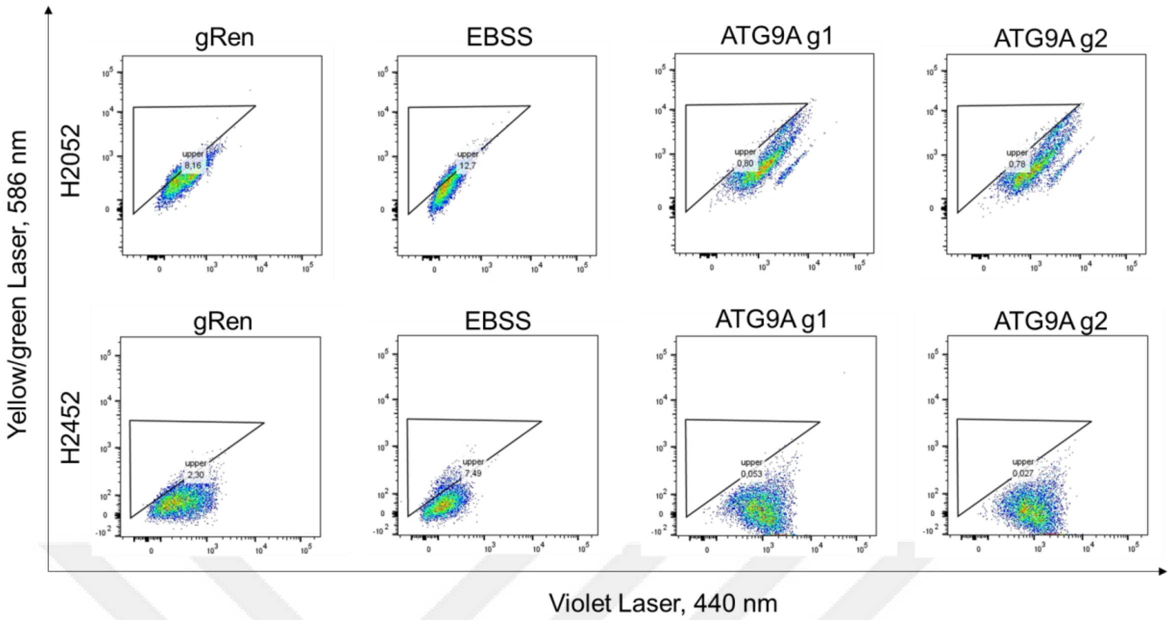

Figure 46: mKeima expression in gRen control and *ATG9A* deficient H2052 and H2452 cells. Cells were transiently transfected with the mt-mKeima plasmid and subjected to flow cytometry analysis. Yellow green laser was used for pH 4.5 (lysosome) and violet laser was used for pH 7 (cytosol). Results were analyzed in FlowJo software. As positive control, cells were treated with EBSS for 24 hours before the analysis. Upper results represent mitochondria that transfer from cytosol to lysosome. Results of H2052 were 8.16, 12.7, 0.90 and 0.78 respectively. Results of H2452 were 2.30, 7.49, 0.053 and 0.027 respectively.

4.13. Genome Wide Transcriptomics via RNA Sequencing Identifies Differentially Expressed Genes and Phenotypic Changes in *ATG9A* Deficient Cells

RNA sequencing (RNA-seq) can be instrumental in understanding gene function. To gain insights into the function of ATG9A in MPM cells, we performed genome wide transcriptomics analysis in cells both sufficient and deficient for *ATG9A* expression. To achieve *ATG9A* deficiency, we utilized the CRISPR/Cas9 system with gRNA 1 to knockout the *ATG9A* gene in H2052 and H2452 cells. Control cells were infected with Renilla luciferase targeting gRNA as a reference. We isolated total RNA samples, in duplicate, from these cells and sent them for sequencing at Macrogen. The resulting RNA-seq data were subjected to bioinformatics analysis by Sude Erıκ, a graduate student in our laboratory. To assess the overall similarity and clustering of the samples based on their transcriptomic profiles, we conducted principal component analysis (PCA). PCA enables visualization of sample clusters and patterns in the data.

Remarkably, we observed distinct clusters between the *ATG9A* knockout (ATG9A KO) and gRen (Renilla) control samples in both cell lines. This indicates a significant difference in the gene expression patterns between the two groups. Particularly, the variance between the ATG9A KO and Renilla control samples accounted for approximately 99-97% of the overall variance in gene expression, while approximately 3% of the variance was observed within each group (Renilla and ATG9A KO samples) (Figure 47). These findings suggest that the knockout of *ATG9A* has a significant impact on the transcriptional landscape of MPM cells.

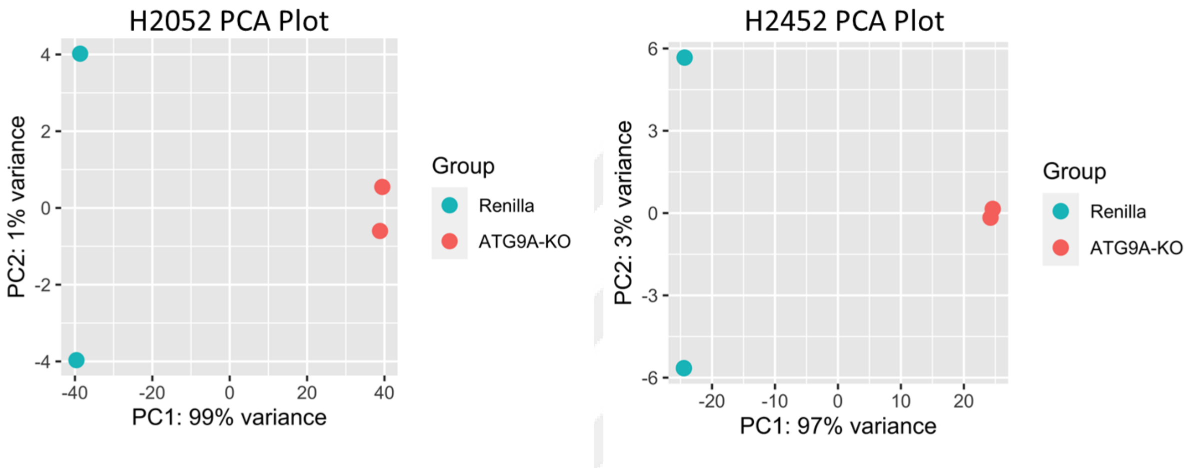

Figure 47: Principal component analysis (PCA) of *ATG9A* sufficient and *ATG9A* deficient H2052 and H2452 cells. The plots depict the outcomes obtained from duplicate samples. Within the H2052 cell line, a substantial 99% variance was observed between the Renilla control and ATG9A knockout (KO) samples. Conversely, a minor 1% variance was noticed among the replicates within this cell line. Similarly, in the H2452 cell line, a significant 97% variance was observed between the Renilla control and ATG9A KO samples, whereas a modest 3% variance was noted among the replicates.

Furthermore, when examining the heatmap results, it became evident that the gene expression patterns of the replicates for the Renilla control samples in each cell line were highly similar to one another. However, notable discrepancies in gene expression patterns were observed between the *ATG9A* deficient samples and the Renilla control samples (Figure 48).

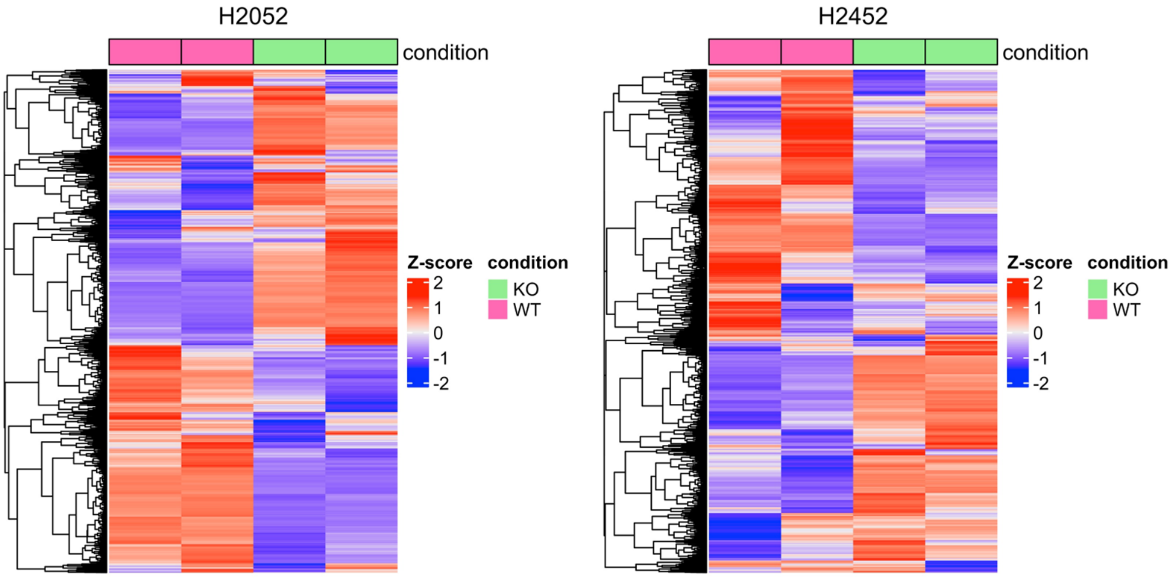

Figure 48: Heatmap results of the RNA-seq analysis of *ATG9A* sufficient and *ATG9A* deficient H2052 and H2452 cells.

Next, we conducted an analysis using volcano plots to further investigate the gene expression changes. The results revealed a substantial number of genes that exhibited either an increase or decrease in their expression levels in *ATG9A* deleted cells compared to the Renilla control cells. In the H2052 cell line, there are 2837 genes with a log fold change of -1 or lower and a significant p-value. Additionally, there are 3262 with a log fold change of 1 or higher and a significant p-value. In the H2452 cell line, there are 741 genes with a log fold change of -1 or lower and a significant p-value, as well as 1275 genes with a log fold change of 1 or higher and a significant p-value.

This indicates a significant alteration in the expression patterns of numerous genes in ATG9A knockout cells when compared to the Renilla control (Figure 49).

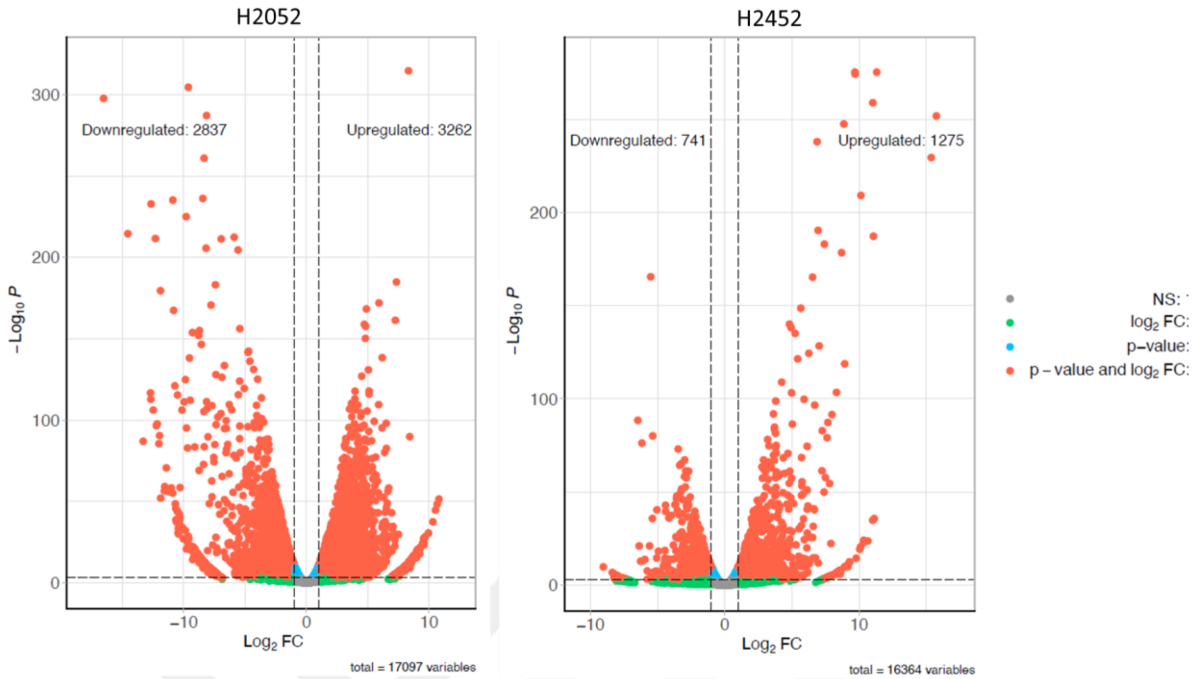

Figure 49: Volcano plot analysis of *ATG9A* silenced cancer cells compared to Renilla control. While the x axis shows the log fold change values, y axis shows the -Log10P (FDR) values.

It was found that a large overlap between H2052 and H2452 cell lines at two thresholds, as shown by the Venn Diagram of differentially expressed genes (DEGs), at Log2FoldChange > 1 or < -1(Figure 50 A), at FDR < 0.05 and Log2FoldChange > 1 or < -1 (Figure 50 B). If we focus on Figure 50 B, about 20% of the upregulated genes are common in the H2052 cell line, and 40% of the upregulated genes are common in the H2452. Similarly, 15% of downregulated genes are common in H2052 and 46% of downregulated genes are common in H2452.

Finally, as an example, the common downregulated and upregulated lists were combined and converted to a list containing absolute values. This list was sorted according to FDR, 20 DEGs were selected as examples from the first 150 genes, and fold changes were plotted within two cell lines (Figure 50 C). All DEGs share similar up- or down-regulation trends in both groups, although they show different fold changes. It has been noticed that most of the DEGs, which are in the first 150, are related to senescence associated secretary phenotypes (SASPs).

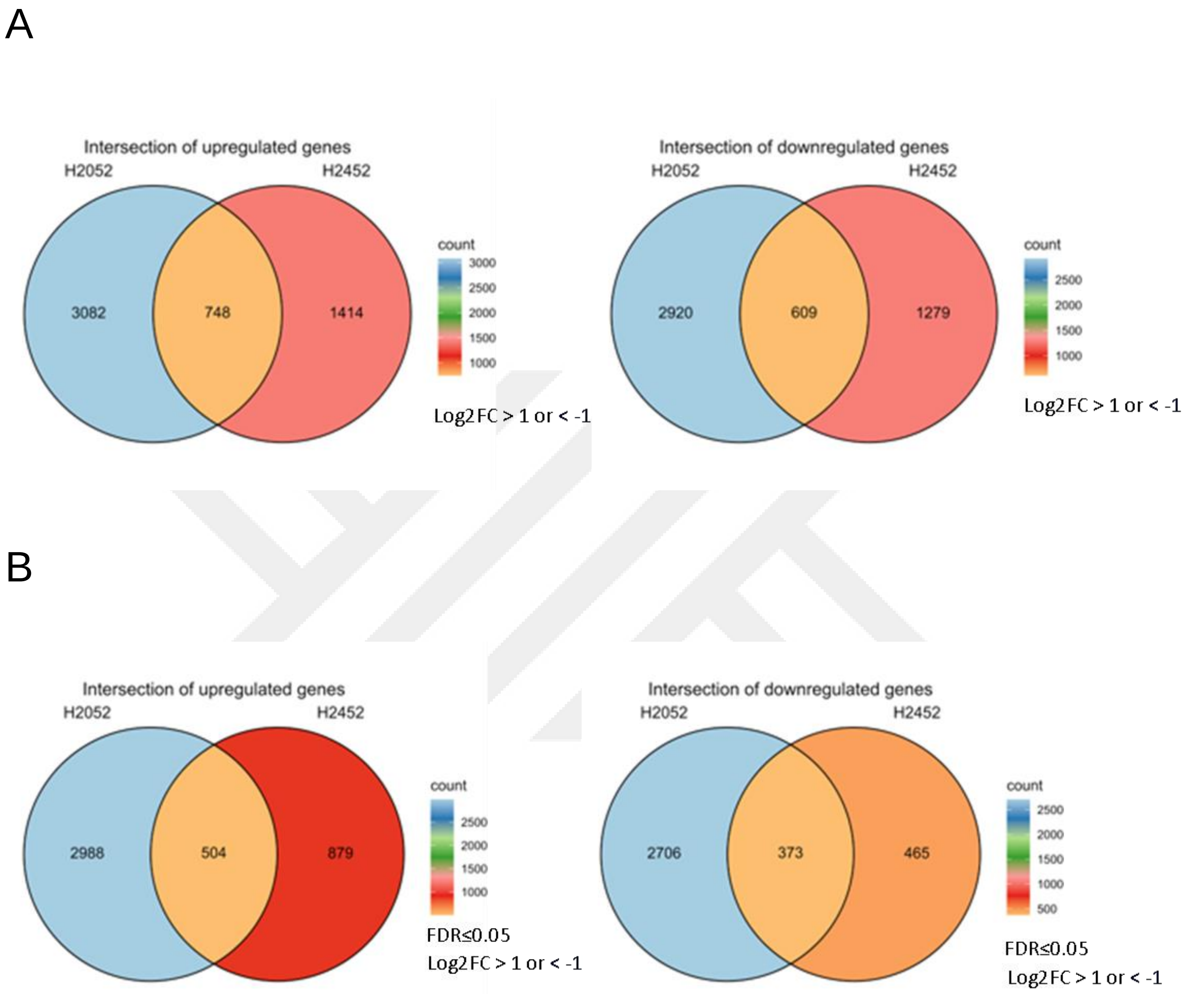
A
Intersection of upregulated genes
H2052
H2452
3082
748
1414
count
3000
2500
2000
1500
1000
Log2FC > 1 or < -1
Intersection of downregulated genes
H2052
H2452
2920
609
1279
count
2500
2000
1500
1000
Log2FC > 1 or < -1
B
Intersection of upregulated genes
H2052
H2452
2988
504
879
count
2500
2000
1500
1000
FDR≤0.05
Log2FC > 1 or < -1
Intersection of downregulated genes
H2052
H2452
2706
373
465
count
2500
2000
1500
1000
500
FDR≤0.05
Log2FC > 1 or < -1

C

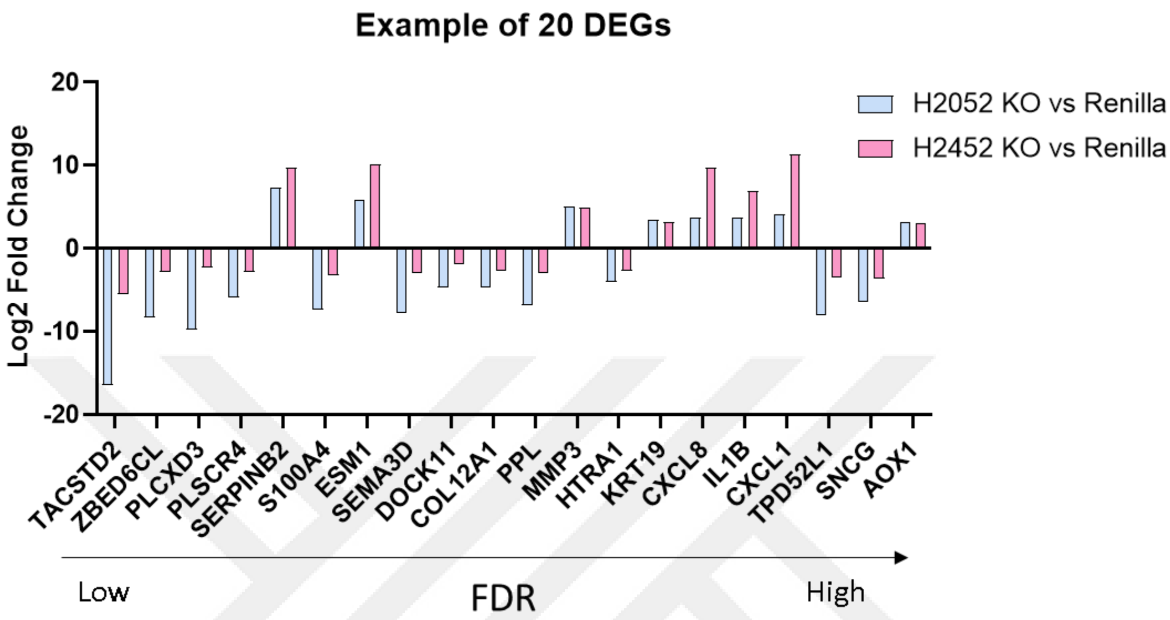

Figure 50: Common differential expression genes of RNA-seq data in both cell lines. A, B) Venn diagrams showing the DEGs identified from the H2052 KO versus Renilla and H2452 versus Renilla groups at Log2FoldChange > 1 or < -1(A), at FDR < 0.05 and Log2FoldChange > 1 or < -1(B). C) Example of 20 DEGs from common absolute list. The horizontal arrow indicates that FDR value increases from left to right.

After that, we made gene ontology analysis by using RNA sequencing results to reduce complexity and highlight biological processes (Figure 51). When we examined the results, we found that the same GO terms were present in both cell lines but with different enrichment values. We also observed some GO results that were consistent with previous phenotypes, such as "negative regulation of cell motility" and "negative regulation of cell population proliferation."

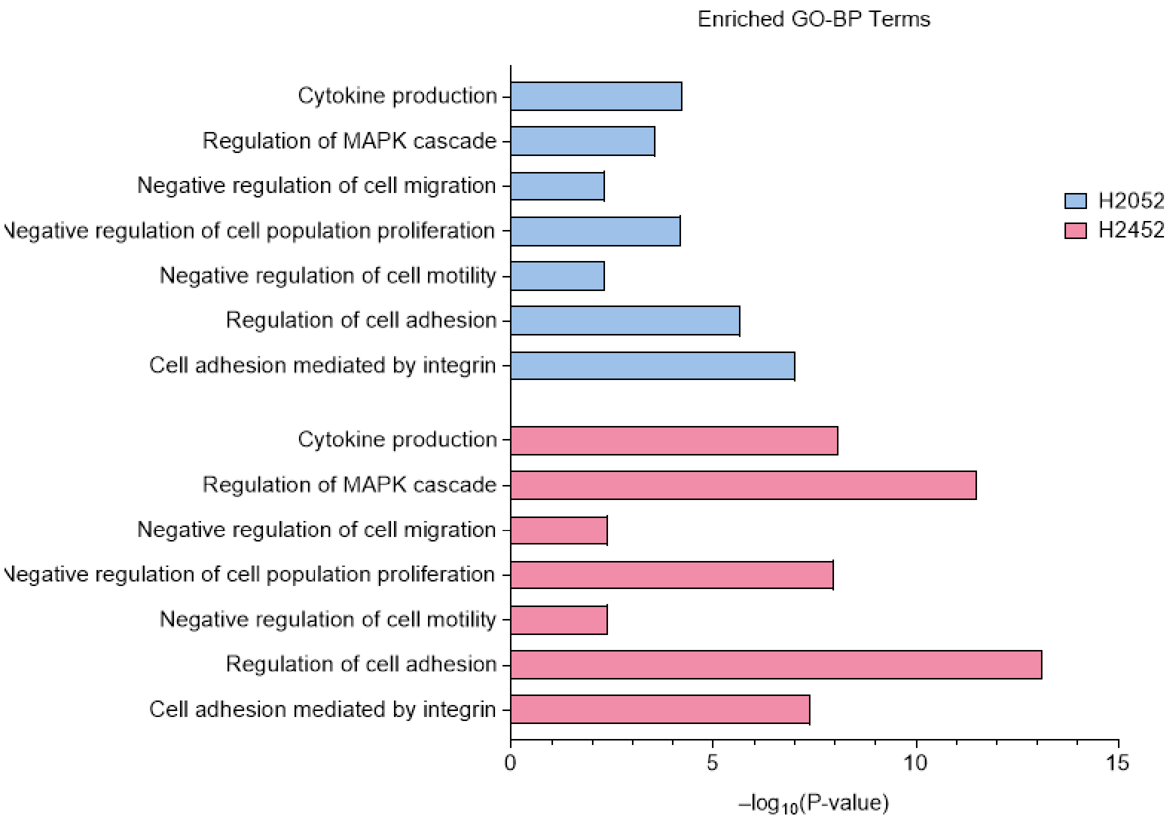

Figure 51: Gene ontology results in H2052 and H2452 cell lines.

Gene set enrichment analysis (GSEA) is a robust technique used to link a specific phenotype with a cluster of genes or proteins. GSEA assigns individual weights to each gene/protein within the provided list based on a selected metric, typically using quantitative expression data. Upon reviewing our findings, we discovered that the gene patterns in the two cell lines showed similarity and concentrated on the phenotypes observed in previous experiments. While there were some variations between the cell lines, they generally exhibited the anticipated phenotypes. One of these phenotypes was apoptosis and when *ATG9A* was silenced in both cell lines, we observed a concentration of genes associated with apoptosis. Another notable phenotype was increased senescence. Moreover, our RNA sequencing analysis revealed more anticipated phenotypes in the H2452 cell line compared to H2052 (Figure 52).

H2052

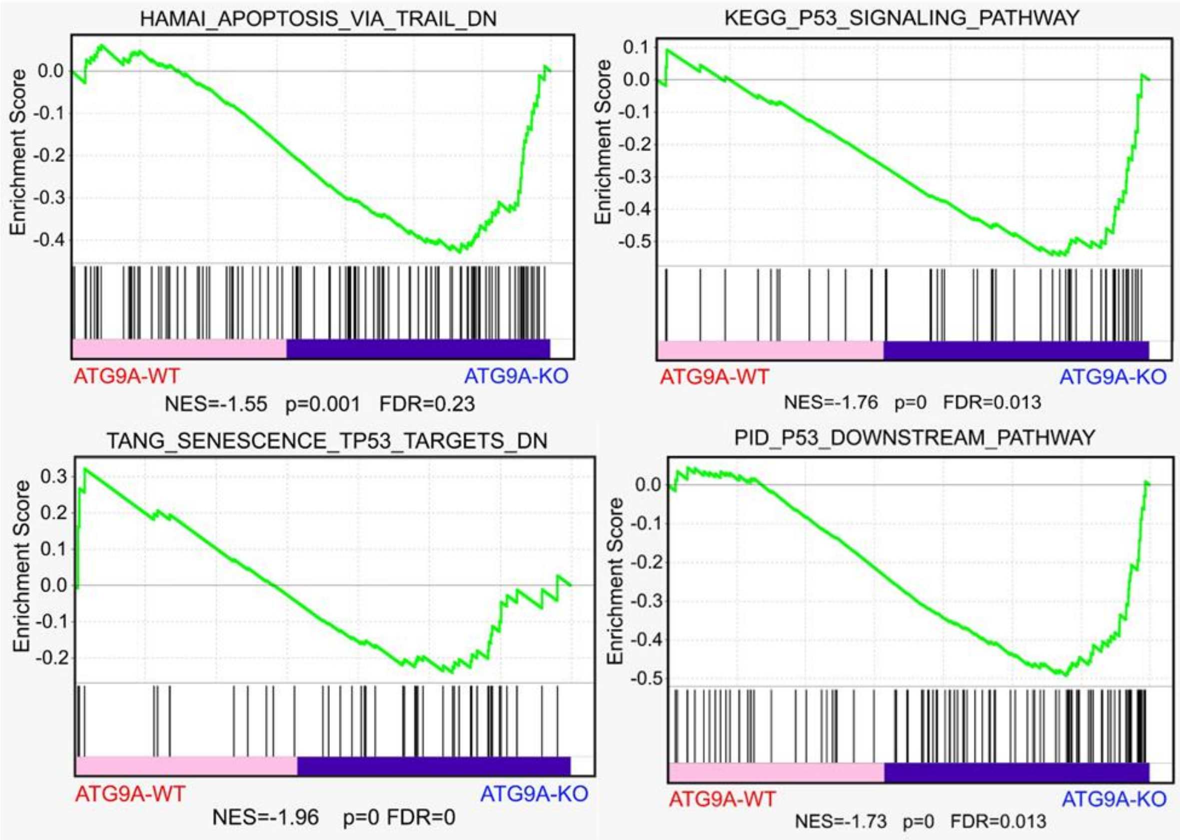
HAMAI_APOPTOSIS_VIA_TRAIL_DN
Enrichment Score
ATG9A-WT
ATG9A-KO
NES=-1.55 p=0.001 FDR=0.23
KEGG_P53_SIGNALING_PATHWAY
Enrichment Score
ATG9A-WT
ATG9A-KO
NES=-1.76 p=0 FDR=0.013
TANG_SENESCENCE_TP53_TARGETS_DN
Enrichment Score
ATG9A-WT
ATG9A-KO
NES=-1.96 p=0 FDR=0
PID_P53_DOWNSTREAM_PATHWAY
Enrichment Score
ATG9A-WT
ATG9A-KO
NES=-1.73 p=0 FDR=0.013

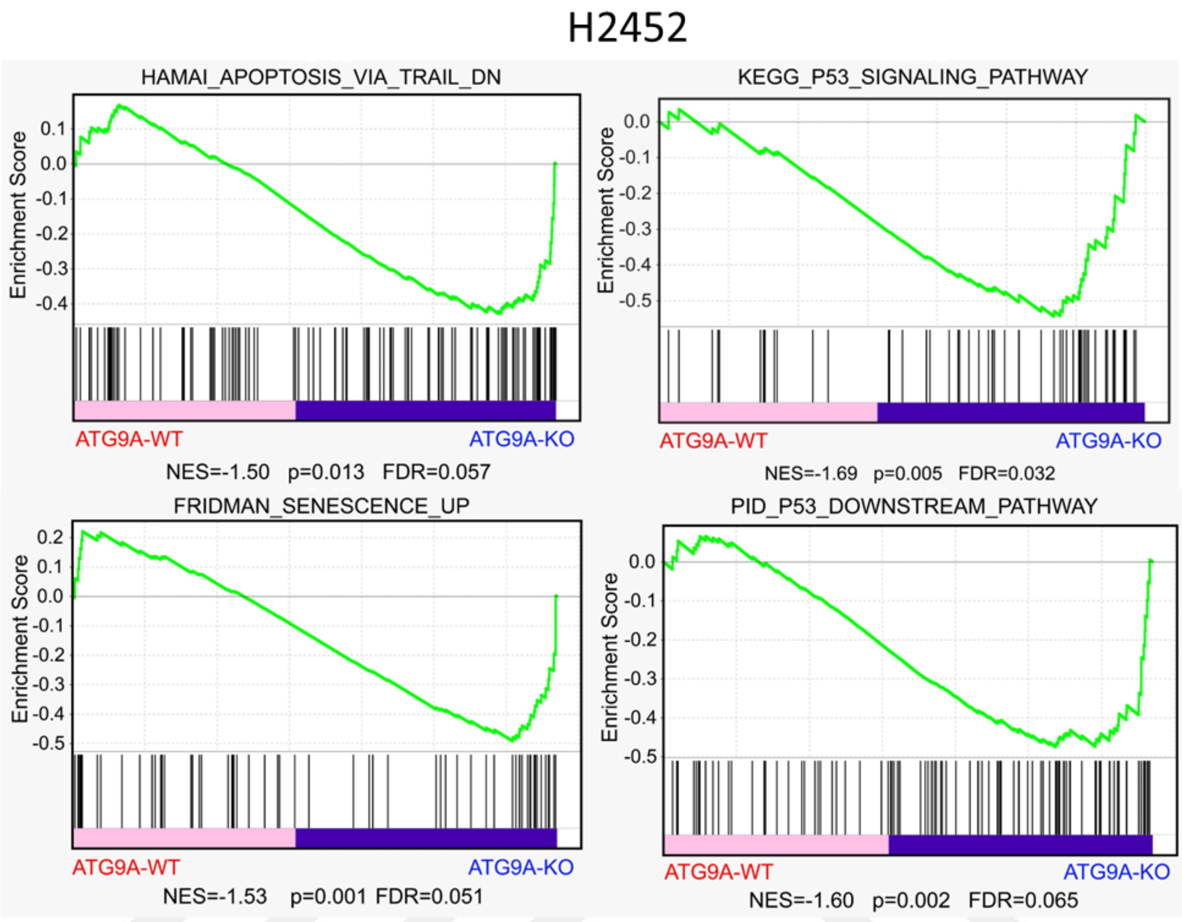

Figure 52: Gene set enrichment analysis of *ATG9A* silenced cancer cells.

4.14. *ATG9A* Overexpression Does Not Confer Increased Cell Proliferation and Growth

After observing the phenotypes that occur when the *ATG9A* gene was silenced, we sought to explore the phenotype that occurs when the *ATG9A* gene expression was increased. We infected the MeT-5A, H2052 and H2452 cell lines with the *ATG9A* overexpression vector (OV clones). For the empty vector formation, the ATG9A gene sequence was cut from the *ATG9A* overexpression vector. In addition to overexpression vector, cells were also infected with empty vector (empty clones). Then, we checked the expression level by western blot analysis to see if the overexpression was successful. As a result, we observed expression of the fusion protein ATG9A with the RFP fluorescent protein in *ATG9A* overexpressed cell lines (Figure 53).

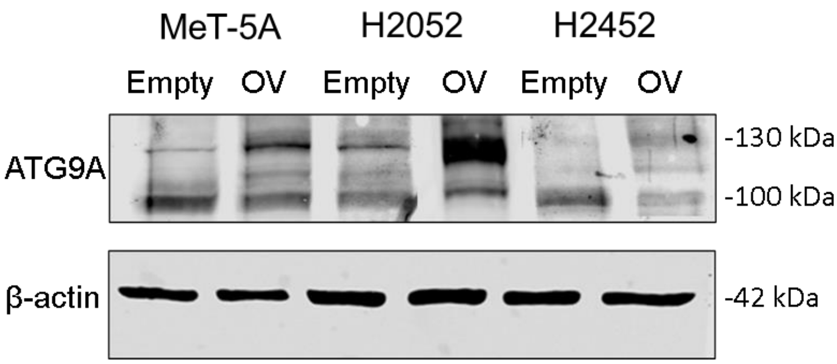

Figure 53: Western blot results of *ATG9A* overexpressed MeT-5A, H2052 and H2452 cells. Lysates were collected post infection day 5. **β**-actin was used as internal control.

Next, we performed an MTT assay to show whether *ATG9A* overexpression has an effect on cell proliferation. In the results, we observed that the proliferation rate did not change in all cell lines (Figure 54).

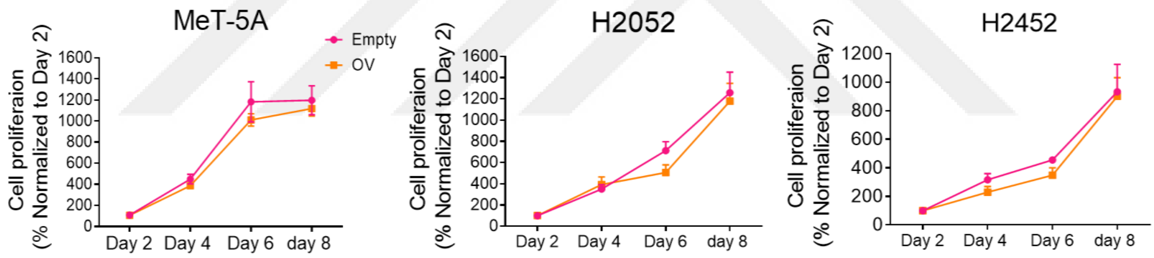

Figure 54: MTT assay results of the *ATG9A* overexpressed cells lines. The first results were obtained two days after seeding and normalized to 100. The results from the other days were normalized to the average of the 2nd day.

We performed a colony formation experiment to see if overexpression had an effect on the 2D colony formation capacity. We found that 2D colony formation capacity was not affected (Figure 55). As a result of all these experiments, we noted that *ATG9A* overexpression had no effect on MeT-5A, H2052 and H2452 cell lines.

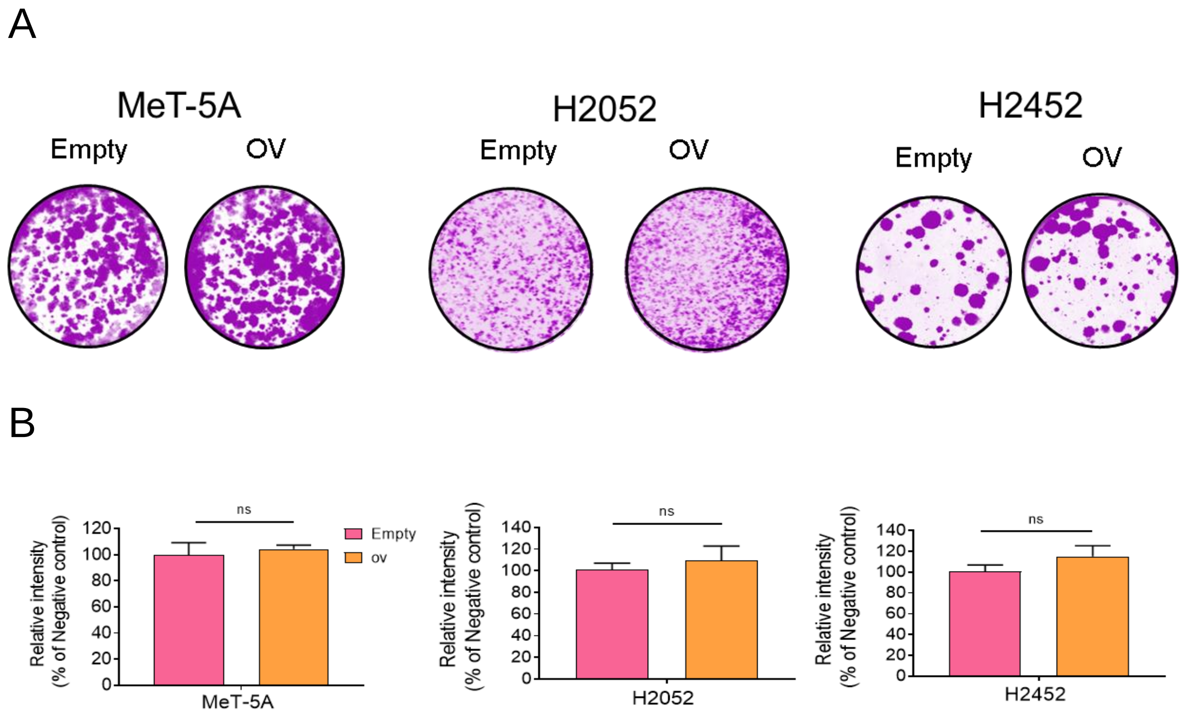

Figure 55: 2D colony formation assay of empty and *ATG9A* overexpression vector infected MeT-5A, H2052 and H2452 cells. The experiment was performed in 3 replicates. A) Representative images were shown. B) Empty control intensities were normalized to 100 and other intensities were normalized accordingly. Mean ŇSD, n=3, *p<0.05, ns: not significant, One-way ANOVA.

4.15. *TMEM41B* Depletion Results in Similar Phenotypes to *ATG9A* Knockout

4.15.1. Depletion of TMEM41B Attenuates Cell Survival and 2D Colony Formation Capacity of MPM Cells

Our investigations, so far, have underscored the significance of ATG9A in not only autophagic processes but also non-autophagic cellular mechanisms, such as the mobilization of lipids from lipid droplets to mitochondria. Recently, TMEM41B, an ER multispanning transmembrane protein with scramblase activity involved in trans-bilayer shuttling of phospholipids, has emerged as a novel regulator of autophagy. Experimental evidence indicates that depletion of *TMEM41B* in H4 astrocytoma cells leads to impaired autophagosome biogenesis. This impairment is associated with the presence of enlarged lipid droplets and a decrease in the mobilization and ɓ-oxidation of fatty acids (86). Considering the critical roles played by autophagy, and lipid mobilization in the survival of MPM cells, our findings suggest that TMEM41B may have a potential role in these processes. Indeed, our CRISPR screen analysis identified *TMEM41B* as a gene with a high depletion score (Figure 56), further highlighting its significance in MPM cell survival.

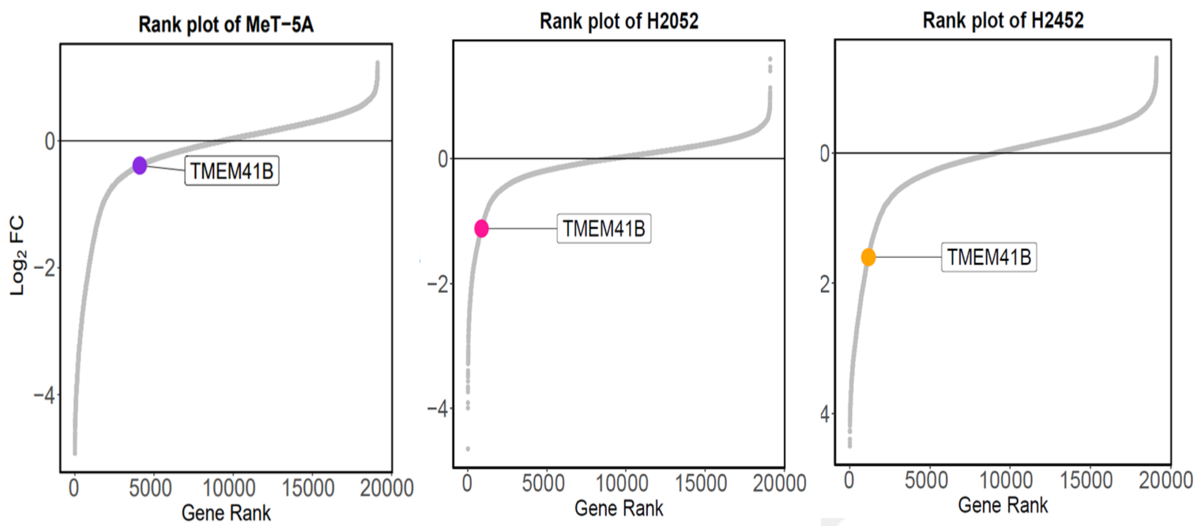

Figure 56: CRISPR gene scores for *TMEM41B* gene in MeT-5A, H2052, and H2452 cell lines.

To validate the results obtained from the CRISPR/Cas9 screen, a competition assay was conducted. Two *TMEM41B* guide RNAs (gRNA 1 and gRNA 2) with high scores from the screen were cloned into the pECPV vector, and the competition assay was performed. The assay involved comparing the effect of *TMEM41B* silencing on Venus positive cell percentages in both MeT-5A cells (non-cancerous) and MPM cell lines. The analysis revealed that depletion of *TMEM41B* resulted in a modest decrease of approximately 20% in the Venus-positive cell percentages in MeT-5A cells after a follow-up period of 21 days. Strikingly, in contrast, a remarkable reduction of up to 70% in the Venus-positive cell population was observed in H2052 and H2452 cells upon *TMEM41B* deletion (Figure 57).

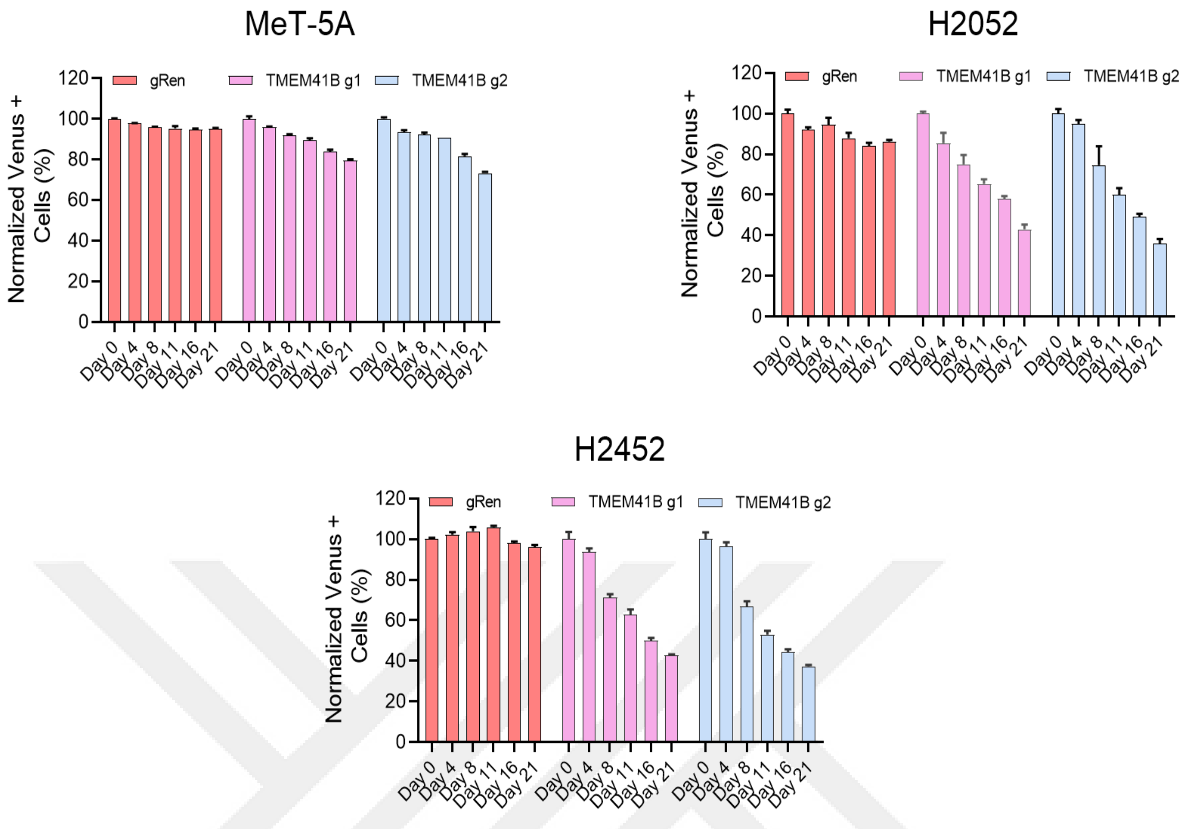

Figure 57: Competition assay results of *TMEM41B* gRNAs and Renilla control in MeT-5A, H2052 and H2452 cell lines. Normalized Venus-positive (+) cell percentages in gRNA (g1) and gRNA 2 (g2) targeted cells. gRen was used as a negative control. Venus positive cell percentages of Day 0 samples were normalized to 100. Results of other days were normalized accordingly.

Following this assay, the same *TMEM41B* gRNAs were cloned into the lentiCRISPR V2 vector. To confirm the successful perturbation of the *TMEM41B* gene, we conducted western blot analysis. Remarkably, the samples subjected to TMEM41B western blotting exhibited a strong reduction in band intensity, providing validation of the CRISPR/Cas9-targeting of this gene (Figure 58).

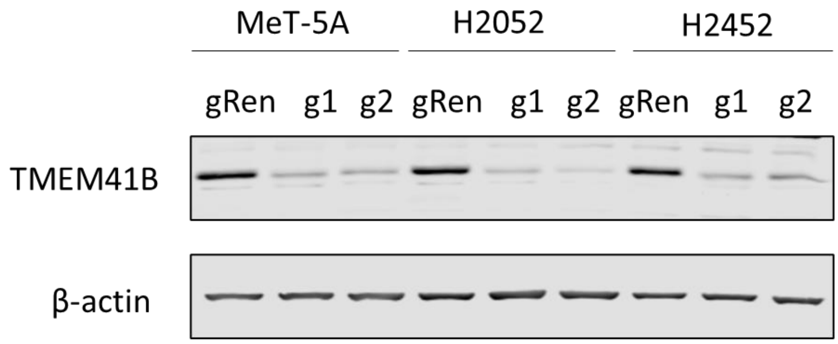

Figure 58: Validation of CRISPR/Cas9-mediated *TMEM41B* deletion in MeT-5A, H2052 and H2452 cells by western blot analysis.

Next, we proceeded to conduct a colony formation assay by plating 2,000 cells into each well of 6 well plates. After 11 days, the emerging colonies were stained and analyzed. The findings revealed that the impact of *TMEM41B* deletion on MeT-5A cells was limited, with a maximum effect of 15% observed. In contrast, *TMEM41B* deficient cancer cells exhibited a substantial reduction of up to 70% in their 2D colony-forming capacity, indicating a significant role of TMEM41B in promoting colony formation in cancer cells (Figure 59).

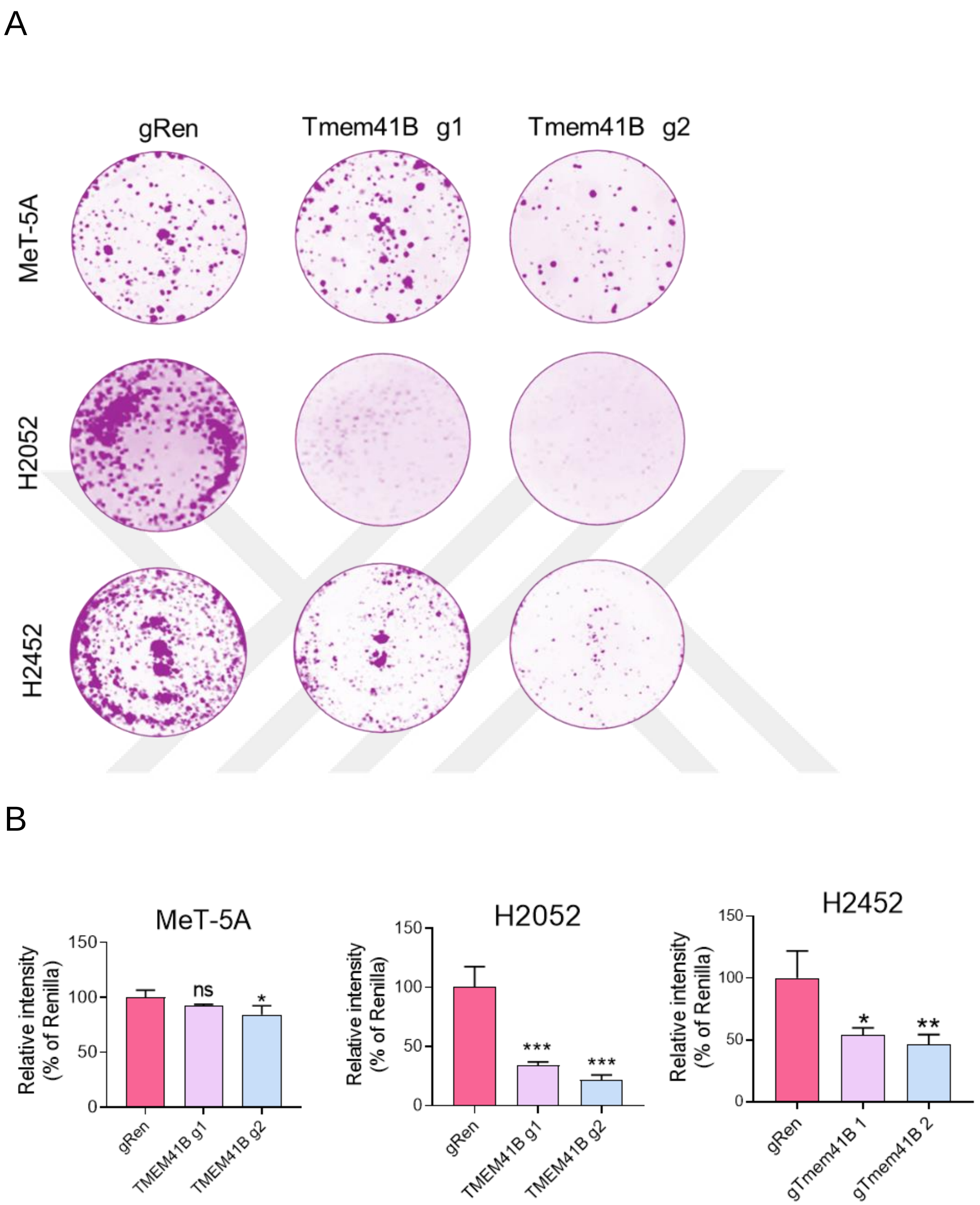

Figure 59: 2D colony formation assay of gRen and *TMEM41B* gRNAs infected MeT-5A, H2052 and H2452 cells. A) Representative images from three replicates are shown. B) gRen control served as a reference and was normalized to 100 in all cell lines. The intensities of other conditions were normalized relative to the control. Statistical analysis was performed using a One-way ANOVA test. The data are shown as mean ÑSD, with n=3. Significant differences are indicated using asterisks: *p<0.05, **p<0.01, ***p<0.001, ns: non-significant.

4.15.2. Absence of TMEM41B Inhibits Lipid Mobilization and Increases Lipid Droplet Number in MPM Cells

After observing the impact of *TMEM41B* gene depletion on the survival and 2D colony formation capacity of cancer cells, we proceeded to investigate its potential role in lipid mobilization ð a non-canonical function that we hypothesized to be crucial in MPM cells. To evaluate this, we employed AUTODOT staining. Critically, our findings revealed that while lipid accumulation was not observed in Renilla control cells, the number of lipid droplets noticeably increased in *TMEM41B* depleted cancer cells, a similar pattern to the ATG9A results (Figure 60). These results suggest that TMEM41B plays a significant role in lipid mobilization, further emphasizing its importance in the context of MPM cells.

A

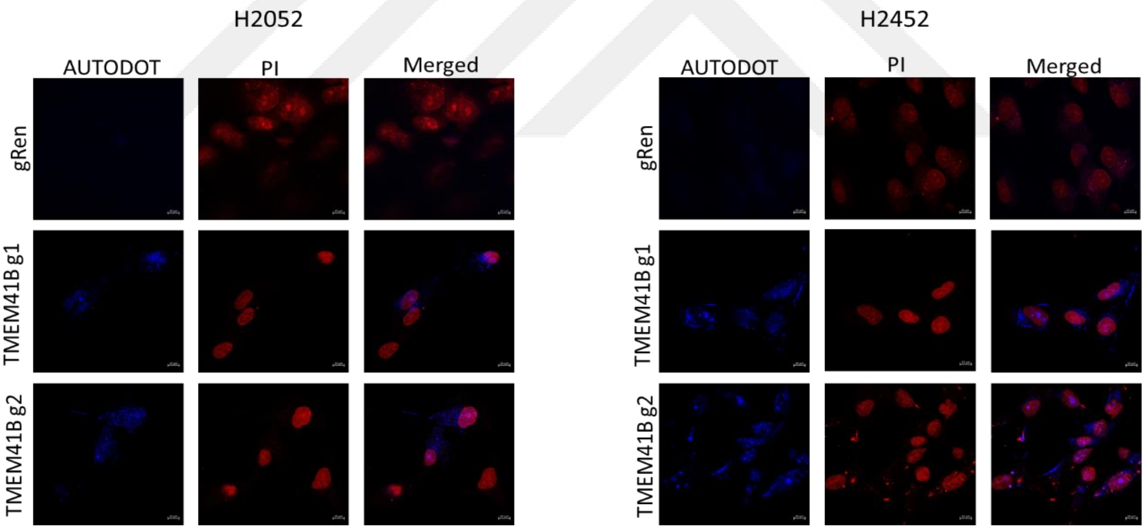

B

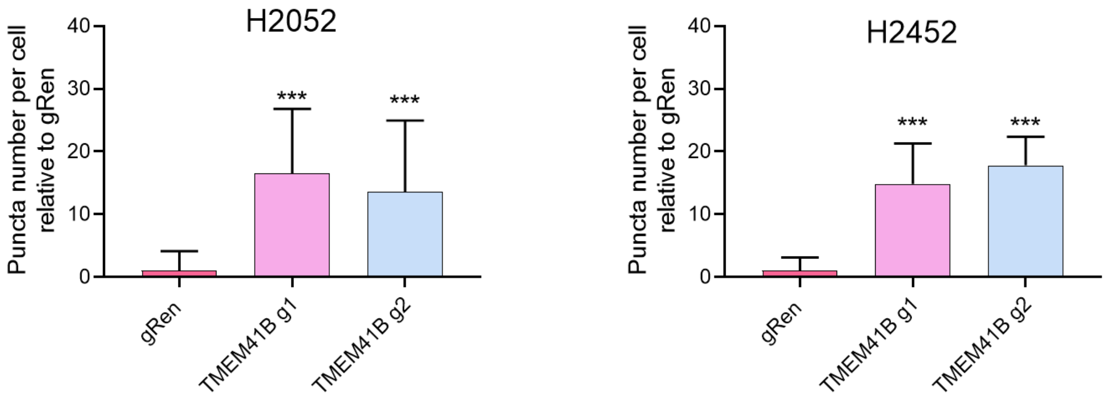

Figure 60: AUTODOT staining of control and *TMEM41B* depleted H2052 and H2452 cells. A) Representative images are shown. Images were acquired using a confocal microscope (magnification 63X). Scale bar: 10 Õm. Propidium iodide was used to counterstain the nucleus. B) The number of puncta (lipid droplets) per cell was quantified using ImageJ software. The data are presented as mean Ñ SD, with n=10. Statistical analysis was performed using one-way ANOVA, and ***p<0.001 indicates a significant difference.

4.15.3. Absence of TMEM41B Gene Causes Cellular Senescence and Decreases the Migration Ability of Cancer Cells

To assess whether *TMEM41B* perturbation leads to comparable phenotypes as ATG9A depletion, we conducted both a SA-ɓ-gal assay and a transwell migration assay. In the SA-ɓ-gal assay, cells were seeded accordingly followed by the addition of X-gal substrate. After incubating for 8 hours, images were captured using a light microscope. The number of cells displaying a blue color, indicative of SA-ɓ-gal positivity, was counted alongside unstained cells. Subsequently, the percentage of SA-ɓ-gal positive cells with a blue coloration was calculated. Our results demonstrated an increased presence of cellular senescence in *TMEM41B* deficient cancer cells, suggesting a potential role of TMEM41B in regulating the senescence phenotype (Figure 61).

A

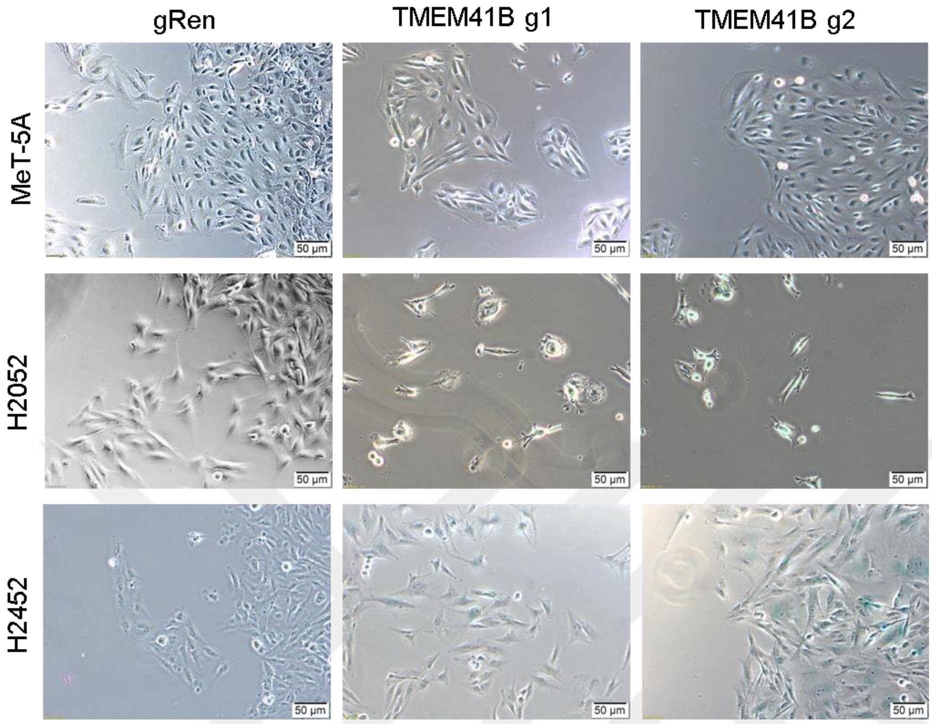

B

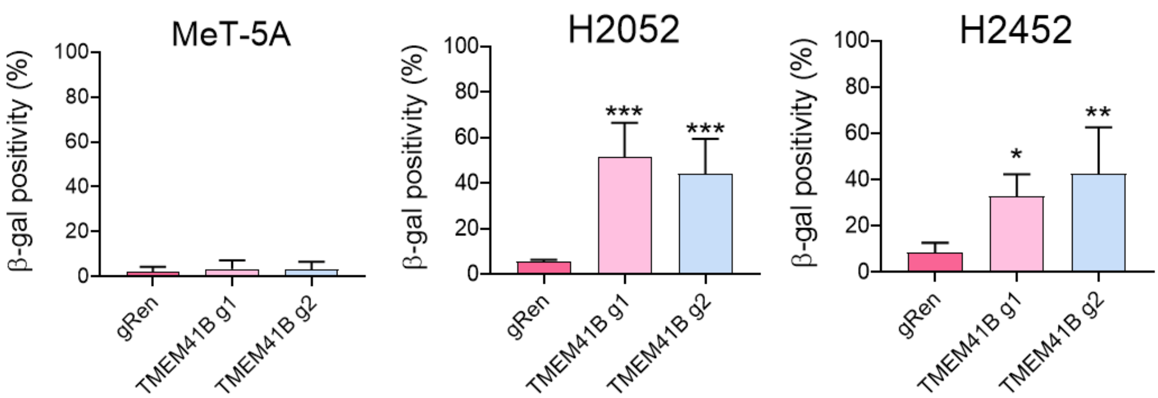

Figure 61: *TMEM41B* deficient cells undergo cellular senescence. A) Representative images are shown. The images were captured at a 20X magnification, and the scale bar represents 50 εm. B) The quantification of SA-ɓ-gal positivity was determined by calculating the ratio of stained cells to the total cell number. The data is presented as mean ÑSD, with n=5. Statistical analysis was conducted using a one-way ANOVA, and the significance levels were *p<0.05, **p<0.01 and ***p<0.001.

In the transwell migration assay, cells were seeded into the transwell Boyden chamber and images were captured 48 hrs later. Notably, our findings indicated a significant decrease in the migration capacity of *TMEM41B* deficient cancer cells, suggesting that *TMEM41B* reduction hampers the ability of cancer cells to migrate effectively (Figure 62).

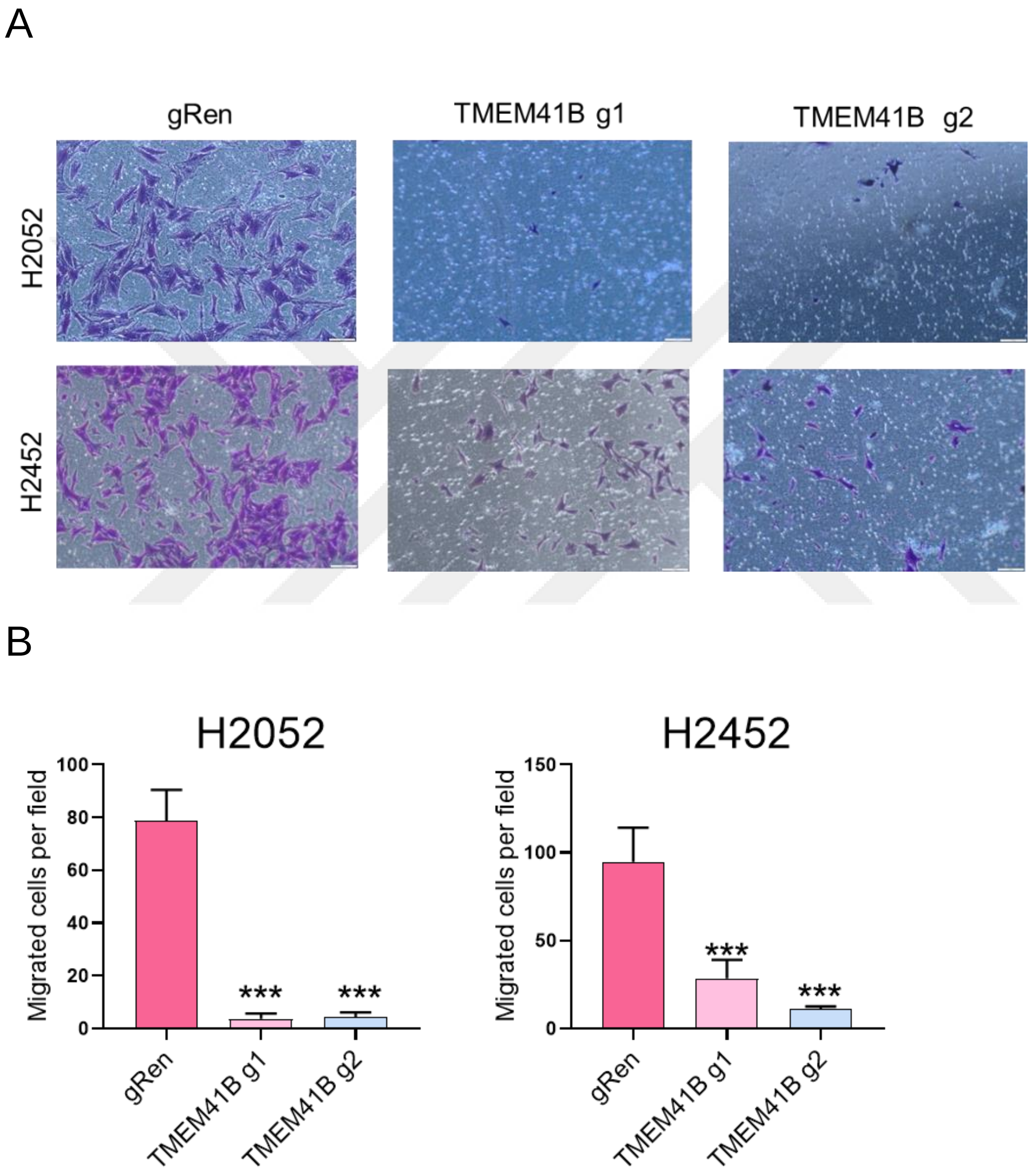

Figure 62: TMEM41B is required for the migration ability of H2052 and H2452 cells. The Boyden Chamber Assay was conducted in duplicate. A) Representative images, captured at 10X magnification, are presented. Scale bar: 100 εm. B) The quantification of migrated cells was performed by manually counting cells in five randomly selected areas. Mean ÑSD, n=5, ***p<0.001, One way ANOVA.

Building upon our previous experiments demonstrating that *ATG9A* silencing resulted in increased ROS levels, we conducted a colony formation assay using NAC treatment to investigate whether the phenotype observed upon *TMEM41B* deletion was also associated with an ROS increase. Strikingly, our results demonstrated that NAC treatment (10 mM) partially but significantly rescued the phenotype that emerged following *TMEM41B* depletion. This finding strongly suggests that the effects observed upon *TMEM41B* knockout are indeed linked to an increase in ROS levels (Figure 63).

A

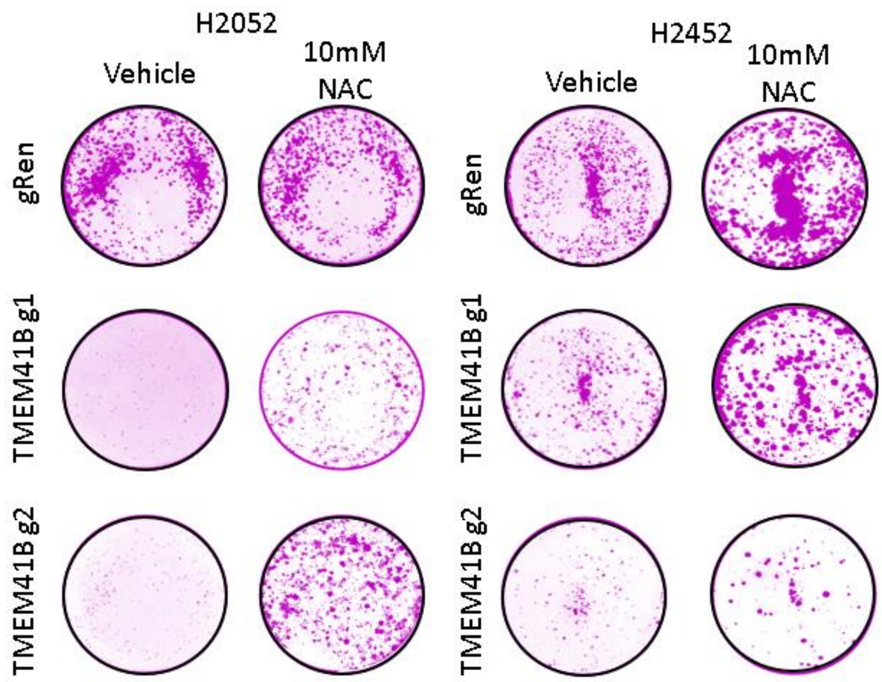

B

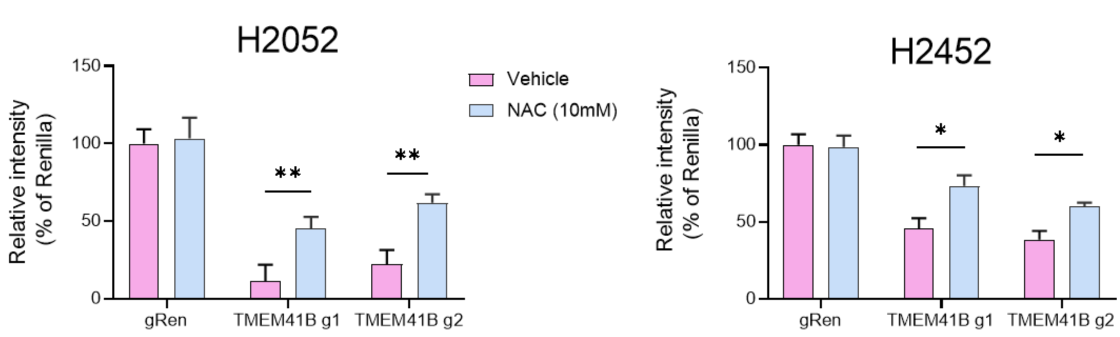

Figure 63: 2D colony formation assay results of the vehicle (DMSO) and NAC treated *TMEM41B* silenced cancer cells. A) Representative images from three replicates are

shown. B) gRen control was normalized to 100 in all cell lines. The intensities of other conditions were normalized relative to the control. Statistical analysis was performed using a One-way ANOVA test. The data are shown as mean ÑSD, with n=3,*p<0.05, **p<0.01.

5. DISCUSSION

MPM represents a malignancy originating from mesothelial cells within the pleura. Asbestos exposure stands as a predominant etiological factor, contributing to approximately 80% of cases (2,8). Characterized by its rarity and aggressive nature, MPM lacks effective targeted therapies, underscoring the need for novel treatment strategies. To address this, it is imperative to unravel the intricate molecular pathways underlying MPM carcinogenesis (1).

Functional genomics aims to uncover the connections between the observable disease characteristics and genes, with the ultimate goal of translating these discoveries into practical applications in clinical settings (1,36). The development of large-scale genomic and transcriptomic sequencing technologies has enabled researchers to identify new mutations and gene expression changes in cancer. CRISPR/Cas9 screening is often performed on a large scale, systematically testing multiple genes at once. By leveraging this technique, researchers can gain a better understanding of the underlying biology and potentially identify new therapeutic targets by identifying key genes and pathways involved in specific diseases or cellular processes (36). In the present thesis study, we conducted comprehensive molecular and functional studies on the gene *ATG9A*, which emerged as a key MPM cell survival candidate through the genome-wide CRISPR/Cas9 screen conducted in our laboratory, aimed to illuminate cancer essential genes in MPM.

ATG9A, a protein known to function as a scramblase in macroautophagy, exerts non-canonical functions as well (3). Specifically, ATG9A participates in lipid transportation from lipid droplets to mitochondria and plays a role in engaging mitophagy alongside the OPTN protein (52,53). Despite limited information regarding its association with cancer, previous studies have reported the loss of cancer aggressive phenotypes in triple-negative breast cancer and hepatocellular carcinoma when *ATG9A* is perturbed (4,5). However, the significance of ATG9A in MPM carcinogenesis remains unknown.

In this study, our primary objective was to examine the role of *ATG9A*, a gene identified through genome-wide CRISPR/Cas9 screen as a critical vulnerability in MPM carcinogenesis. For this purpose, we initially first performed CRISPR/Cas9-mediated *ATG9A* inactivation and comprehensively examined its impact on cell survival and growth using various assays, including 2D and 3D colony formation, MTT, BrdU incorporation, Sa-ɓ-gal staining, and cell cycle analysis. Additionally, we explored the effect of *ATG9A* depletion on cell death, migration, invasion, mitochondrial structure, lipid accumulation, mitophagy, and gene expression through detailed molecular and functional investigations.

To validate the results of the CRISPR screen, we performed a competition assay by selecting two *ATG9A* gRNAs that displayed high scores across all tested cells. However, due to a bias introduced by the gRNA efficiency, which was 2 out of 4, we designed two additional gRNAs to overcome this limitation. Ultimately, all the *ATG9A* gRNAs used confirmed the essentiality of ATG9A for the survival of MPM cells. Next, we cloned all these *ATG9A* specific gRNAs into the LentiCrispr V2 vector and verified their efficacy through western blotting. We observed that gRNA 3 and 4 exhibited lower efficiency in knocking out *ATG9A*. Based on these observations, we decided to proceed with gRNA 1 and 2 for subsequent experiments. Through our investigations, we discovered a significant decrease in both 2D colony formation and 3D soft agar anchorage-independent growth capacities in *ATG9A* deficient cancer cells. Intriguingly, however, MeT-5A results were particularly important. In particular, MeT-5A cells showed a notable impact upon *ATG9A* depletion. These non-tumorigenic cells were also responsive to *ATG9A* deletion, yet the effect was limited to approximately 20%. This suggests that ATG9A may not be essential for MeT-5A cells, but its absence could lead to some degree of response. Other compensatory proteins might attempt to offset the loss of ATG9A, preventing further growth suppression. As expected, MeT-5A cells, being non-tumorigenic, failed to form 3D colonies and only generated small-sized colonies in soft agar. Additionally, a spheroid formation experiment was performed to assess the effect of *ATG9A* depletion on 3D growth capacity. As anticipated, MeT-5A cells failed to form 3D spheroids. Despite multiple attempts, however, H2452 cells also did not generate spheroids, this failure could be attributed to the inherent inability of these cells to form spheroids or potentially other technical or biological optimization requirements. In the H2052 cell line, which was able to form spheroids, smaller spheroids were observed in *ATG9A* deleted cells, as expected. The MTT and BrdU assays provided evidence that cell growth was significantly impaired in *ATG9A* knockout cells. To confirm whether this slowdown was specifically attributed to ATG9A, a successful rescue experiment was conducted, where the phenotype was largely restored upon reintroducing *ATG9A* expression into the cells. Furthermore, similar to what was observed in the 2D colony formation assay, the BrdU experiment indicated a slight decrease in cell growth upon *ATG9A* depletion in MeT-5A cells. However, this decrease was not as pronounced and biologically significant compared to what was observed in cancer cells. In an effort to elucidate the underlying cause of the growth slowdown, a cell cycle experiment was conducted, revealing an increase in the duration of G2 phase in *ATG9A* depleted cells. Notably, in the H2052 cell line, there was a noticeable decrease in the S phase alongside a reciprocal increase in the G2 phase. Similarly, in the H2452 cell line, there was a decrease in both the S and G1 phases, accompanied by an increase in the G2 phase. Knocking out the *ATG9A* gene in MeT-5A cells resulted in an increase in the G2 phase, along with a slight increase in the S phase. Based on these findings, it can be inferred that *ATG9A* depletion in cancer cells induces a G2 arrest, considering the observed decrease in the S and G1 phases. In MeT-5A cells, the increase in the G2 phase while maintaining or even slightly increasing the S phase is consistent with the observed phenotype. Accumulation in the G2 phase is likely to have detrimental effects on cell behavior in cancer cells, whereas the absence of a significant reduction in the S phase does not lead to a significant change in MeT-5A cell proliferation. In addition to G2 arrest, we found that cells would undergo cellular senescence upon *ATG9A* depletion. This is consistent with the expected outcome since the enlarged and flattened phenotype exhibited by dying cells is indicative of this phenomenon. Similar to G2 arrest, we also observed the senescence phenotype in MeT-5A cells. However, the percentage of senescence in cancer cells was around 40%, and even up to 80% in H2052 cell lines, while it was limited to around 20% in MeT-5A cells.

Furthermore, considering the significant extent of cell death observed, we delved into the potential implications of apoptosis or autophagy. In the annexin V staining experiment, we discovered that cancer cells underwent apoptosis upon the loss of *ATG9A*. In the case of MeT-5A cells, a modest level of approximately 6% apoptosis was consistently observed across all experimental conditions. This baseline level of apoptosis in MeT-5A cells may stem from inherent apoptotic processes or, more plausibly, a general response triggered by the viral infection endured during the experimental course. To support our findings, we conducted western blot analysis and observed an increase in band intensities for cleaved caspase-3 and PARP. The weaker appearance of cleaved PARP in H2052 cells may be due to its low expression level in this specific cell line. In the autophagy experiment, we performed western blot analysis to assess the crucial proteins involved in the autophagy process. As ATG9A is an autophagy-related protein, it was expected that autophagy would be impacted by its depletion. Indeed, the results confirmed this expectation. LC3 protein undergoes a conversion from LC3I to LC3II when autophagy is functioning properly (75). Normal medium was used as control and starvation medium (EBSS) was used to induce autophagy. Under starvation conditions, the Renilla controls exhibited the expected conversion of LC3I to LC3II. However, in the cells where *ATG9A* was silenced, we observed an increase in both forms of LC3. This intriguing finding prompted further investigation into whether it indicated active autophagy or impaired autophagy. To shed light on this matter, we examined the levels of the p62 protein, which plays a critical role in the conversion process and is expected to decrease during active autophagy. Surprisingly, we observed an increase in p62 levels, suggesting impaired autophagy (76). Beclin1 was also used as another control for autophagy. As a result, we observed a decrease in beclin1, despite the expected increase in active autophagy. Finally, to determine whether the accumulation of p62 was somehow related to the accumulation of LC3, we performed LC3 puncta staining. Strikingly enough, we observed larger LC3 puncta than normal, providing additional evidence of autophagy impairment through an alternative approach (77).

Upon knocking out *ATG9A*, we presented compelling evidence of DNA damage through two distinct experiments. Interestingly, in stark contrast to prior findings in the MeT-5A cell line, all experimental conditions yielded consistent outcomes, with no discernible DNA damage detected. Conversely, the presence of DNA damage in MPM cell lines, reminiscent of senescence characteristics, raised inquiries regarding the potential association between *ATG9A* depletion and the accumulation of ROS. Therefore, in the experiments conducted, we demonstrated ROS accumulation in *ATG9A* perturbed cancer cells. To determine whether the observed phenotypes were directly related to ROS accumulation, we used NAC, a ROS scavenger (74), and performed 2D colony formation assay. Intriguingly, we discovered that NAC was capable of rescuing the phenotype induced by *ATG9A* ablation. However, this rescue was not entirely efficacious, suggesting that although ROS might play a significant role, the entire mechanism may not be solely dependent on ROS. Following a comprehensive examination of all phenotypes arising from *ATG9A* knockout, we contemplated its impact on the aggressive phenotype, which holds paramount importance for cancer patients. Consequently, we executed additional experiments such as migration and invasion assays. As a result, we observed the loss of the aggressive phenotype in *ATG9A* deleted cancer cells, aligning with previous findings. This finding has been shown in the literature in triple negative breast cancer, and also overlaps with the role of ATG9A in forming lamellipodia (4,78).

As mentioned earlier, ATG9A exhibits non-canonical pathways that we believe play a vital role in MPM. Therefore, our focus was directed towards exploring these particular functions. One such function is lipid mobilization. In a study by Mailler et al., it was demonstrated that ATG9A is located in close proximity to mitochondria and facilitates the transport of lipids from lipid droplets to the mitochondria, where they partake in mitochondrial respiration (53). They also demonstrated that this process varies in different conditions. To investigate this phenomenon, we first conducted a colocalization experiment under both normal and EBSS conditions. As expected, we observed apposition of ATG9A with mitochondria in both conditions. However, in the EBSS condition, the Pearson correlation coefficient value was closer to 1, indicating increased colocalization. To examine lipid transport, we performed lipid droplet staining and we observed an increase in the number of lipid droplets in *ATG9A* depleted cells since lipids cannot be transported and are accumulated. Based on this information, we can explain the increased apposition of ATG9A and mitochondria during starvation. In a state of starvation, considering that more lipids are directed towards mitochondria for respiration, it is expected that ATG9A, which is involved in lipid transport, would approach mitochondria more closely than in the normal condition of the cell.

Secondly, our attention was directed towards the initiation of mitophagy. According to the findings of Yamano et al., ATG9A plays a role in the initiation of mitophagy, in association with the OPTN protein (52). If ATG9A is unable to facilitate mitophagy or if it leads to impaired autophagy, cell death, or the accumulation of mitochondrial ROS, this raises the question of whether any structural damage has occurred to the mitochondria. To explore this aspect, we initially examined structural disparities using MitoTracker staining, which revealed the expected presence of certain structural variations. For a more comprehensive analysis, we employed TOMM20 staining to label the mitochondrial membrane and employed the MiNa tool in ImageJ software to analyze the results, thereby providing statistical evidence of the observed differences (84). Next, we performed a mitophagy experiment using the mt-mKeima plasmid. As anticipated, we observed an increase in mitophagy in the EBSS condition, while *ATG9A* ablated cells exhibited a decrease in mitophagy. In conclusion, we can infer that ATG9A contributes to the initiation of mitophagy in MPM cells. Furthermore, our findings indicate that cells are unable to engage in mitophagy in the absence of the *ATG9A* gene.

Following the RNA-seq analysis, it became evident that the knocking out ATG9A led to a considerable alteration in the expression of numerous genes in both cell lines, as compared to the gRen control. As anticipated, replicates of the *ATG9A* sufficient cells exhibited clustering, as did the replicates of *ATG9A* deficient cells. However, it became apparent that the underlying mechanisms driving the changes in gene expression were diverse, resulting in varying numbers of genes within the shared clusters. The range of genes exhibiting significant changes in expression spanned between 600 and 700. Given that only a single gene (*ATG9A*) was depleted, it is possible that there might not be a cumulative effect on the gene sets. Nevertheless, notable changes were observed in several important genes within the clusters, suggesting their potential association with the observed phenotypes. To further investigate this, our focus shifted to gene set enrichment analysis aimed at identifying gene sets specific to particular biological processes. Notably, our analysis revealed a higher number of biologically relevant gene sets when considering H2452, in comparison to H2052. In particular, we found genes that clustered into expected clusters such as senescence and apoptosis. In addition, we observed that genes were collected both in the trail-mediated apoptosis cluster and in the clusters of many genes related to the P53 signal pathway. Since the p53 pathway is known to increase in stress condition and its increase activates pathways such as apoptosis and senescence, these results were as expected when compared to previous findings (87). However, despite the informative nature of these findings, we were unable to identify a substantial number of processes that corresponded directly to the observed phenotype in H2052 cells, which likely indicates that the impacts of *ATG9A* deficiency may be context dependent.

After observing the detrimental consequences related to the absence of *ATG9A* in MPM cells, we became particularly intrigued about the potential impact of its ectopic. Surprisingly, however, no significant impact was observed in cells overexpressing *ATG9A*. One possible explanation for this finding could be the existence of a negative feedback loop within the cells, regulating the expression of autophagy related genes and the cells may not be affected by *ATG9A* upregulation due to this regulatory mechanism. The other plausible explanation may be the fact that the intrinsic mechanisms governed by ATG9A are finely tuned and remain unaffected by increased expression. Finally, our attention was subsequently drawn to the TMEM41B gene. This gene plays a supporting role in lipid transfer from the endoplasmic reticulum to other membranes (53). Based on this attribute, TMEM41B is involved in both autophagy and lipid mobilization (86). Given the crucial importance of autophagy and lipid mobilization in H2052 and H2452 cell lines and considering that the observed phenotypes were attributed to defects in these two processes, we decided to conduct experiments by silencing TMEM41B as a control. Remarkably, the absence of TMEM41B resulted in similar phenotypes as those observed in the absence of *ATG9A*. Taken together, our novel findings strongly suggest that ATG9A, as well as TMEM41B, and the cellular and molecular mechanisms elucidated in this work play indispensable roles in ensuring the survival of MPM cells.

6. CONCLUSION AND FUTURE PERSPECTIVES

When *ATG9A* was silenced in MPM cells using four different gRNAs, we observed a decrease in proliferation compared to non-tumorigenic cell line. While the decrease rate was around 20% in non-tumorigenic cell line, it reached around 80% in cancer cells. To rescue this decrease, we conducted experiments with *ATG9A* overexpression vector and successfully restored the proliferation. Subsequently, we conducted experiments with *ATG9A* gRNAs from two Brunello libraries and observed that the decrease in proliferation was associated with G2 arrest and senescence. Furthermore, we noticed an increase in apoptosis in *ATG9A*-silenced MPM cells compared to non-tumorigenic cell line. Through studies conducted with LC3, we concluded that autophagy was impaired. In experiments aiming to identify the underlying cause of cell death, we discovered that this effect occurred through ROS-induced DNA damage, and we observed partial rescue of the phenotype in experiments with a ROS scavenger. In addition to these findings, we observed that the silencing of *ATG9A* led to the loss of cancer aggressive phenotypes in the cancer cells. We attempted to explain all observed phenotypes with both the canonical and non-canonical functions of ATG9A. In this study, we focused on two non-canonical functions of ATG9A. First, we observed that ATG9A is involved in the transfer of lipids from lipid droplets to mitochondria, and in the absence of *ATG9A*, lipids accumulate in the lipid droplets in cancer cells. Secondly, when we focused on mitophagy, we observed a significant decrease in mitophagy in *ATG9A*-silenced cancer cells, indicating that these cells were unable to perform mitophagy when *ATG9A* was silenced. RNA sequencing analysis revealed significant changes in gene expression upon *ATG9A* silencing, and although these changes were generally different between the two MPM cell lines, we observed an increase in senescence and apoptosis in both cell lines through gene set enrichment analysis, confirming our previous findings. We noticed that overexpression of *ATG9A* did not have an impact on the phenotype. Based on the observed mechanisms and screening results, we conducted experiments with the *TMEM41B* gene to investigate whether the identified phenotypes were related to the functions of ATG9A as mentioned above. As a result, we observed that TMEM41B exhibited similar functions in MPM cells and its silencing, similar to *ATG9A* silencing, led to cell death. In summary, based on all these results, we can conclude that ATG9A is crucial for both autophagy and mitochondrial respiration in MPM cells. When ATG9A is unable to transport lipids, a decrease in respiration occurs, and when autophagy cannot be performed, an increase in ROS occurs and results in mitochondrial stress. Since the cells are unable to alleviate this stress through mitophagy, they undergo cell death. As future directions, if we aim to demonstrate the role of ATG9A in mitochondrial respiration, if not we will provide evidence for the mechanism mentioned above. Additionally, conducting a small-scale screen with selected genes can yield more in-depth results and help identify other important genes involved in autophagy and lipid transportation is another future aspect of ours. This way, we can present a more detailed mechanism. Before considering clinical applications of our findings, it would be advisable to perform *in vivo* experiments using the CRISPR system. Following that, a collaboration can be formed with a research group focusing on protein research to design a specific inhibitor targeting ATG9A, before moving closer to translational studies.

7. REFERENCES

1. Cakiroglu E, Senturk S. Genomics and Functional Genomics of Malignant Pleural Mesothelioma. Int J Mol Sci. 2020 Sep 1;21(17):6342.
2. Hmeljak J, Sanchez-Vega F, Hoadley KA, Shih J, Stewart C, Heiman D, et al. Integrative Molecular Characterization of Malignant Pleural Mesothelioma. Cancer Discov. 2018 Dec;8(12):1548ï 65.
3. Guardia CM, Tan XF, Lian T, Rana MS, Zhou W, Christenson ET, et al. Structure of Human ATG9A, the Only Transmembrane Protein of the Core Autophagy Machinery. Cell Reports. 2020 Jun;31(13):107837.

4. Kimkong I, Kunanopparat A. Autophagy related protein 9A increase in hepatitis B virus-associated hepatocellular carcinoma and the role in apoptosis. World J Hepatol. 2020 Dec 27;12(12):1367ï 71.

5. Claude-Taupin A, Fonderflick L, Gauthier T, Mansi L, Pallandre JR, Borg C, et al. ATG9A Is Overexpressed in Triple Negative Breast Cancer and Its In Vitro Extinction Leads to the Inhibition of Pro-Cancer Phenotypes. Cells. 2018 Dec 6;7(12):248.

6. Sung H, Ferlay J, Siegel RL, Laversanne M, Soerjomataram I, Jemal A, et al. Global Cancer Statistics 2020: GLOBOCAN Estimates of Incidence and Mortality Worldwide for 36 Cancers in 185 Countries. CA A Cancer J Clin. 2021 May;71(3):209ï 49.

7. Yap TA, Aerts JG, Popat S, Fennell DA. Novel insights into mesothelioma biology and implications for therapy. Nat Rev Cancer. 2017 Aug;17(8):475ï 88.

8. Tsao AS, Wistuba I, Roth JA, Kindler HL. Malignant Pleural Mesothelioma. JCO. 2009 Apr 20;27(12):2081ï 90.

9. Brcic L, Kern I. Clinical significance of histologic subtyping of malignant pleural mesothelioma. Transl Lung Cancer Res. 2020 Jun;9(3):924ï 33.

10. Verma V, Ahern CA, Berlind CG, Lindsay WD, Shabason J, Sharma S, et al. Survival by Histologic Subtype of Malignant Pleural Mesothelioma and the Impact of Surgical Resection on Overall Survival. Clinical Lung Cancer. 2018 Nov;19(6):e901ï 12.

11. Paajanen J, Laaksonen S, Ilonen I, Wolff H, Husgafvel-Pursiainen K, Kuosma E, et al. Computed tomography in the evaluation of malignant pleural mesotheliomað Association of tumor size to a sarcomatoid histology, a more advanced TNM stage and poor survival. Lung Cancer. 2018 Feb;116:73ï 9.

12. Attanoos RL, Churg A, Galateau-Salle F, Gibbs AR, Roggli VL. Malignant Mesothelioma and Its Non-Asbestos Causes. Arch Pathol Lab Med. 2018 Jun;142(6):753ï 60.

13. Gomez DR, Rimner A, Simone CB, Cho BCJ, de Perrot M, Adjei AA, et al. The Use of Radiation Therapy for the Treatment of Malignant Pleural Mesothelioma: Expert Opinion from the National Cancer Institute Thoracic Malignancy Steering

Committee, International Association for the Study of Lung Cancer, and Mesothelioma Applied Research Foundation. J Thorac Oncol. 2019 Jul;14(7):1172ï 83.

14. Sun HH, Vaynblat A, Pass HI. Diagnosis and prognosis-review of biomarkers for mesothelioma. Ann Transl Med. 2017 Jun;5(11):244.

15. Galani V, Varouktsi A, Papadatos SS, Mitselou A, Sainis I, Constantopoulos S, et al. The role of apoptosis defects in malignant mesothelioma pathogenesis with an impact on prognosis and treatment. Cancer Chemother Pharmacol. 2019 Aug;84(2):241ï 53.

16. Huang SXL, Jaurand MC, Kamp DW, Whysner J, Hei TK. Role of mutagenicity in asbestos fiber-induced carcinogenicity and other diseases. J Toxicol Environ Health B Crit Rev. 2011;14(1ï 4):179ï 245.

17. Pociask DA, Sime PJ, Brody AR. Asbestos-derived reactive oxygen species activate TGF-beta1. Lab Invest. 2004 Aug;84(8):1013ï 23.

18. Kamp DW, Weitzman SA. The molecular basis of asbestos induced lung injury. Thorax. 1999 Jul;54(7):638ï 52.

19. Crovella S, Moura RR, Cappellani S, Celsi F, Trevisan E, Schneider M, et al. A genetic variant of NLRP1 gene is associated with asbestos body burden in patients with malignant pleural mesothelioma. J Toxicol Environ Health A. 2018;81(5):98ï 105.

20. Dubois F, Bazille C, Levallet J, Maille E, Brosseau S, Madelaine J, et al. Molecular Alterations in Malignant Pleural Mesothelioma: A Hope for Effective Treatment by Targeting YAP. Target Oncol. 2022 Jul;17(4):407ï 31.

21. Carbone M, Ly BH, Dodson RF, Pagano I, Morris PT, Dogan UA, et al. Malignant mesothelioma: facts, myths, and hypotheses. J Cell Physiol. 2012 Jan;227(1):44ï 58.

22. Johnson B, Lee K, Cheng YY. Pre-Clinical Research Advancements Relating to Improving the Diagnosis and Treatment of Malignant Pleural Mesothelioma: A Review. Onco. 2021 Sep 26;1(2):49ï 82.

23. Thurneysen C, Opitz I, Kurtz S, Weder W, Stahel RA, Felley-Bosco E. Functional inactivation of NF2/merlin in human mesothelioma. Lung Cancer. 2009 May;64(2):140ï 7.

24. Illei PB, Rusch VW, Zakowski MF, Ladanyi M. Homozygous deletion of CDKN2A and codeletion of the methylthioadenosine phosphorylase gene in the majority of pleural mesotheliomas. Clin Cancer Res. 2003 Jun;9(6):2108ï 13.

25. Bott M, Brevet M, Taylor BS, Shimizu S, Ito T, Wang L, et al. The nuclear deubiquitinase BAP1 is commonly inactivated by somatic mutations and 3p21.1 losses in malignant pleural mesothelioma. Nat Genet. 2011 Jun 5;43(7):668ï 72.

26. Vinagre J, Almeida A, P· pulo H, Batista R, Lyra J, Pinto V, et al. Frequency of TERT promoter mutations in human cancers. Nat Commun. 2013;4:2185.

27. Tallet A, Nault JC, Renier A, Hysi I, Galateau-Sall® F, Cazes A, et al. Overexpression and promoter mutation of the TERT gene in malignant pleural mesothelioma. Oncogene. 2014 Jul 10;33(28):3748ï 52.

28. Quetel L, Meiller C, Assi® JB, Blum Y, Imbeaud S, Montagne F, et al. Genetic alterations of malignant pleural mesothelioma: association with tumor heterogeneity and overall survival. Mol Oncol. 2020 Jun;14(6):1207ï 23.

29. Gomez DR, Hong DS, Allen PK, Welsh JS, Mehran RJ, Tsao AS, et al. Patterns of failure, toxicity, and survival after extrapleural pneumonectomy and hemithoracic intensity-modulated radiation therapy for malignant pleural mesothelioma. J Thorac Oncol. 2013 Feb;8(2):238ï 45.

30. Rimner A, Zauderer MG, Gomez DR, Adusumilli PS, Parhar PK, Wu AJ, et al. Phase II Study of Hemithoracic Intensity-Modulated Pleural Radiation Therapy (IMPRINT) As Part of Lung-Sparing Multimodality Therapy in Patients With Malignant Pleural Mesothelioma. J Clin Oncol. 2016 Aug 10;34(23):2761ï 8.

31. Vogelzang NJ, Rusthoven JJ, Symanowski J, Denham C, Kaukel E, Ruffie P, et al. Phase III study of pemetrexed in combination with cisplatin versus cisplatin alone in patients with malignant pleural mesothelioma. J Clin Oncol. 2003 Jul 15;21(14):2636ï 44.

32. Santoro A, OÕBrien ME, Stahel RA, Nackaerts K, Baas P, Karthaus M, et al. Pemetrexed plus cisplatin or pemetrexed plus carboplatin for chemonaµve patients with malignant pleural mesothelioma: results of the International Expanded Access Program. J Thorac Oncol. 2008 Jul;3(7):756ï 63.

33. Baas P, Scherpereel A, Nowak A, Fujimoto N, Peters S, Tsao A, et al. ID:2908 First-Line Nivolumab + Ipilimumab vs Chemotherapy in Unresectable Malignant Pleural Mesothelioma: CheckMate 743. Journal of Thoracic Oncology. 2020 Oct;15(10):e42.

34. Bronte G, Incorvaia L, Rizzo S, Passiglia F, Galvano A, Rizzo F, et al. The resistance related to targeted therapy in malignant pleural mesothelioma: Why has not the target been hit yet? Crit Rev Oncol Hematol. 2016 Nov;107:20ï 32.

35. Nicolini F, Bocchini M, Bronte G, Delmonte A, Guidoboni M, Crin¸ L, et al. Malignant Pleural Mesothelioma: State-of-the-Art on Current Therapies and Promises for the Future. Front Oncol. 2019;9:1519.

36. Shalem O, Sanjana NE, Zhang F. High-throughput functional genomics using CRISPR-Cas9. Nat Rev Genet. 2015 May;16(5):299ï 311.

37. Lee A, Siders DB, Lee F, Konnak JW. Transrectal ultrasound. A case report related to the natural history of prostate cancer. Cancer. 1989 Apr 15;63(8):1548ï 51.

38. Aguirre AJ, Meyers RM, Weir BA, Vazquez F, Zhang CZ, Ben-David U, et al. Genomic Copy Number Dictates a Gene-Independent Cell Response to CRISPR/Cas9 Targeting. Cancer Discov. 2016 Aug;6(8):914ï 29.

39. Wang K, Schmied WH, Chin JW. Reprogramming the genetic code: from triplet to quadruplet codes. Angew Chem Int Ed Engl. 2012 Mar 5;51(10):2288ï 97.

40. Glick D, Barth S, Macleod KF. Autophagy: cellular and molecular mechanisms. J Pathol. 2010 May;221(1):3ï 12.

41. Li Y, Hyland F, Hu G. Prompting MEd students to engage with academia and the professional world through feedback. Journal of English for Academic Purposes. 2017 Mar;26:52ï 65.

42. Keller JN, Dimayuga E, Chen Q, Thorpe J, Gee J, Ding Q. Autophagy, proteasomes, lipofuscin, and oxidative stress in the aging brain. The International Journal of Biochemistry & Cell Biology. 2004 Dec;36(12):2376ï 91.

43. Saftig P, Beertsen W, Eskelinen EL. LAMP-2: a control step for phagosome and autophagosome maturation. Autophagy. 2008 May;4(4):510ï 2.

44. Rios J, Sequeida A, Albornoz A, Budini M. Chaperone Mediated Autophagy Substrates and Components in Cancer. Front Oncol. 2020;10:614677.

45. Levine B, Klionsky DJ. Development by self-digestion: molecular mechanisms and biological functions of autophagy. Dev Cell. 2004 Apr;6(4):463ï 77.

46. Klionsky DJ. Autophagy: from phenomenology to molecular understanding in less than a decade. Nat Rev Mol Cell Biol. 2007 Nov;8(11):931ï 7.

47. Maiuri MC, Zalckvar E, Kimchi A, Kroemer G. Self-eating and self-killing: crosstalk between autophagy and apoptosis. Nat Rev Mol Cell Biol. 2007 Sep;8(9):741ï 52.

48. Saikia R, Joseph J. AMPK: a key regulator of energy stress and calcium-induced autophagy. J Mol Med. 2021 Nov;99(11):1539ï 51.

49. Matoba K, Kotani T, Tsutsumi A, Tsuji T, Mori T, Noshiro D, et al. Atg9 is a lipid scramblase that mediates autophagosomal membrane expansion. Nat Struct Mol Biol. 2020 Dec;27(12):1185ï 93.

50. Maeda S, Yamamoto H, Kinch LN, Garza CM, Takahashi S, Otomo C, et al. Structure, lipid scrambling activity and role in autophagosome formation of ATG9A. Nat Struct Mol Biol. 2020 Dec;27(12):1194ï 201.

51. Claude-Taupin A, Jia J, Bhujabal Z, Garfa-Traor® M, Kumar S, da Silva GPD, et al. ATG9A protects the plasma membrane from programmed and incidental permeabilization. Nat Cell Biol. 2021 Aug;23(8):846ï 58.

52. Yamano K, Kikuchi R, Kojima W, Hayashida R, Koyano F, Kawawaki J, et al. Critical role of mitochondrial ubiquitination and the OPTN-ATG9A axis in mitophagy. J Cell Biol. 2020 Sep 7;219(9):e201912144.

53. Mailler E, Guardia CM, Bai X, Jarnik M, Williamson CD, Li Y, et al. The autophagy protein ATG9A enables lipid mobilization from lipid droplets. Nat Commun. 2021 Nov 19;12(1):6750.

54. Senturk S, Shirole NH, Nowak DG, Corbo V, Pal D, Vaughan A, et al. Rapid and tunable method to temporally control gene editing based on conditional Cas9 stabilization. Nat Commun. 2017 Feb 22;8:14370.

55. Gyori BM, Venkatachalam G, Thiagarajan PS, Hsu D, Clement MV. OpenComet: An automated tool for comet assay image analysis. Redox Biology. 2014;2:457ï 65.

56. Li H, Handsaker B, Wysoker A, Fennell T, Ruan J, Homer N, et al. The Sequence Alignment/Map format and SAMtools. Bioinformatics. 2009 Aug 15;25(16):2078ï 9.

57. Ito K, Murphy D. Application of ggplot2 to Pharmacometric Graphics. CPT Pharmacometrics Syst Pharmacol. 2013 Oct 16;2(10):e79.

58. UALCAN [Internet]. 2023. Available from: http://ualcan.path.uab.edu/.

59. GEPIA [Internet]. 2023. Available from: http://gepia.cancer-pku.cn/.

60. He X, Wang L, Riedel H, Wang K, Yang Y, Dinu CZ, et al. Mesothelin promotes epithelial-to-mesenchymal transition and tumorigenicity of human lung cancer and mesothelioma cells. Mol Cancer. 2017 Mar 14;16(1):63.

61. Crane AM, Bhattacharya SK. The use of bromodeoxyuridine incorporation assays to assess corneal stem cell proliferation. Methods Mol Biol. 2013;1014:65ï 70.

62. Itahana K, Campisi J, Dimri GP. Methods to detect biomarkers of cellular senescence: the senescence-associated beta-galactosidase assay. Methods Mol Biol. 2007;371:21ï 31.

63. Xu X, Lai Y, Hua ZC. Apoptosis and apoptotic body: disease message and therapeutic target potentials. Biosci Rep. 2019 Jan 31;39(1):BSR20180992.

64. Crowley LC, Marfell BJ, Scott AP, Waterhouse NJ. Quantitation of Apoptosis and Necrosis by Annexin V Binding, Propidium Iodide Uptake, and Flow Cytometry. Cold Spring Harb Protoc. 2016 Nov 1;2016(11).

65. Wang W, Zhu M, Xu Z, Li W, Dong X, Chen Y, et al. Ropivacaine promotes apoptosis of hepatocellular carcinoma cells through damaging mitochondria and activating caspase-3 activity. Biol Res. 2019 Jul 12;52(1):36.

66. Zhou L, Wang S, Cao L, Ren X, Li Y, Shao J, et al. Lead acetate induces apoptosis in Leydig cells by activating PPARɔ/caspase-3/PARP pathway. Int J Environ Health Res. 2021 Jan;31(1):34ï 44.

67. Yuan LQ, Wang C, Lu DF, Zhao XD, Tan LH, Chen X. Induction of apoptosis and ferroptosis by a tumor suppressing magnetic field through ROS-mediated DNA damage. Aging (Albany NY). 2020 Feb 18;12(4):3662ï 81.

68. Kaina B. DNA damage-triggered apoptosis: critical role of DNA repair, double-strand breaks, cell proliferation and signaling. Biochem Pharmacol. 2003 Oct 15;66(8):1547ï 54.

69. Rogakou EP, Pilch DR, Orr AH, Ivanova VS, Bonner WM. DNA double-stranded breaks induce histone H2AX phosphorylation on serine 139. J Biol Chem. 1998 Mar 6;273(10):5858ï 68.

70. Olive PL, Ban§th JP. The comet assay: a method to measure DNA damage in individual cells. Nat Protoc. 2006;1(1):23ï 9.

71. Yu F, Wei J, Cui X, Yu C, Ni W, Bungert J, et al. Post-translational modification of RNA m6A demethylase ALKBH5 regulates ROS-induced DNA damage response. Nucleic Acids Research. 2021 Jun 4;49(10):5779ï 97.

72. Eruslanov E, Kusmartsev S. Identification of ROS using oxidized DCFDA and flow-cytometry. Methods Mol Biol. 2010;594:57ï 72.

73. Parascandolo A, Laukkanen MO. Carcinogenesis and Reactive Oxygen Species Signaling: Interaction of the NADPH Oxidase NOX1ï 5 and Superoxide Dismutase 1ï 3 Signal Transduction Pathways. Antioxidants & Redox Signaling. 2019 Jan 20;30(3):443ï 86.

74. De Andrade K, Moura F, Dos Santos J, De Ara¼jo O, De Farias Santos J, Goulart M. Oxidative Stress and Inflammation in Hepatic Diseases: Therapeutic Possibilities of N-Acetylcysteine. IJMS. 2015 Dec 18;16(12):30269ï 308.

75. Mizushima N, Yoshimori T. How to Interpret LC3 Immunoblotting. Autophagy. 2007 Nov 26;3(6):542ï 5.

76. Girolamo F, Lia A, Annese T, Giannini M, Amati A, DôAbbicco D, et al. Autophagy markers LC3 and p62 accumulate in immune-mediated necrotizing myopathy. Muscle Nerve. 2019 Sep;60(3):315ï 27.

77. Runwal G, Stamatakou E, Siddiqi FH, Puri C, Zhu Y, Rubinsztein DC. LC3-positive structures are prominent in autophagy-deficient cells. Sci Rep. 2019 Jul 12;9(1):10147.

78. Campisi D, Desrues L, Demb®l® KP, Mutel A, Parment R, Gandolfo P, et al. The core autophagy protein ATG9A controls dynamics of cell protrusions and directed migration. Journal of Cell Biology. 2022 Mar 7;221(3):e202106014.

79. Suarez-Arnedo A, Torres Figueroa F, Clavijo C, Arbel§ez P, Cruz JC, Mu¶oz-Camargo C. An image J plugin for the high throughput image analysis of in vitro scratch wound healing assays. Chirico G, editor. PLoS ONE. 2020 Jul 28;15(7):e0232565.

80. Chen HC. Boyden chamber assay. Methods Mol Biol. 2005;294:15ï 22.

81. Park SH, Lee AR, Choi K, Joung S, Yoon JB, Kim S. TOMM20 as a potential therapeutic target of colorectal cancer. BMB Rep. 2019 Dec;52(12):712ï 7.

82. Mura A, Moriel-Carretero M. Lack of evidence for condensin or cohesin sequestration on lipid droplets with packing defects. MicroPubl Biol. 2021;2021.

83. Monteiro L de B, Davanzo GG, de Aguiar CF, Moraes-Vieira PMM. Using flow cytometry for mitochondrial assays. MethodsX. 2020;7:100938.

84. Valente AJ, Maddalena LA, Robb EL, Moradi F, Stuart JA. A simple ImageJ macro tool for analyzing mitochondrial network morphology in mammalian cell culture. Acta Histochem. 2017 Apr;119(3):315ï 26.

85. Alan P, Vandevoorde KR, Joshi B, Cardoen B, Gao G, Mohammadzadeh Y, et al. Basal Gp78-dependent mitophagy promotes mitochondrial health and limits mitochondrial ROS. Cell Mol Life Sci. 2022 Oct 25;79(11):565.

86. Moretti F, Bergman P, Dodgson S, Marcellin D, Claerr I, Goodwin JM, et al. TMEM 41B is a novel regulator of autophagy and lipid mobilization. EMBO Reports. 2018 Sep;19(9):e45889.

87. Marei HE, Althani A, Afifi N, Hasan A, Caceci T, Pozzoli G, et al. p53 signaling in cancer progression and therapy. Cancer Cell Int. 2021 Dec 24;21(1):703.

8. APPENDICES

İZMİR BİYOTIP VE GENOM MERKEZİ
GİRİŞİMSEL OLMAYAN ARAŞTIRMALAR ETİK KURULU (İBG-GOEK)
KARARI

Toplantı Tarihi	: 25/06/2021	**Toplantı Günü**	: Cuma
Toplantı Sayısı	: 7	**Toplantı Saati**	: 10:30

Sayın Doç. Dr. Şerif ŞENTÜRK,

2021-018 Protokol No'lu; sorumlusu olduğunuz "Malign Plevral Mezotelyoma Hücrelerinin Sağkalımında ATG9A Geninin Hayati Rolü" başlıklı araştırmanın uygulanmasında etik açıdan sakınca olmadığına oy birliği ile karar verilmiştir.

Bilgilerinizi ve gereğini rica ederiz.

Prof. Dr. H. Alper BAĞRIYANIK **Başkan**	**Dr. Serap ERKEK ÖZHAN** **Başkan Yardımcısı**
Prof. Dr. Sedef AKGÜNGÖR **Üye**	**Prof. Dr. İnci ALAÇALIOĞLU** **Üye**
Prof. Dr. Gülgün OKTAY **Üye**	**Prof. Dr. Hilmi ORHAN** **Üye**
Doç. Dr. Canan Aslı YILDIRIM **Üye**	

MERVE UYSAL

Personal Information

Contact Information

Contact Address

Telephone

Email

Web Page

Education Information

30 September 2020 - Now (2 Year 10 Month)
Yüksek Lisans, Tezli Program, DOKUZ EYLÜL ÜNİVERSİTESİ, TÜRKİYE
İZMİR ULUSLARARASI BİYOTIP VE GENOM ENSTİTÜSÜ, MOLEKÜLER BİYOLOJİ VE GENETİK (YL) (TEZLİ) (İNGİLİZCE)
Diploma Number: -

03 August 2015 - 16 July 2020 (5 Year)
Lisans, Anadal/Normal Öğretim, İZMİR YÜKSEK TEKNOLOJİ ENSTİTÜSÜ, TÜRKİYE
FEN FAKÜLTESİ, MOLEKÜLER BİYOLOJİ VE GENETİK PR. (İNGİLİZCE)
Diploma Number: 4604
Cumulative Grade Point Average: 3.55 / 4.0

R&D Competency

Articles

F. A. MAZİ, E. CAKİROGLU, M. UYSAL, M. KALYONCU, D. DEMİRCİ, P. Y. G. SOZERİ, G. O. YİLMAZ, S. E. OZHAN & S. SENTURK, The paracaspase MALT1 is a downstream target of Smad3 and potentiates the crosstalk between TGF-beta and NF-kB signaling pathways in cancer cells, CELLULAR SIGNALLING, 2023, 0898-6568, 105.

M. U. & S. S. M. Z. GÜNGÖR, , The Bright and the Dark Side of TGF-ß Signaling in Hepatocellular Carcinoma: Mechanisms, Dysregulation, and Therapeutic Implications, Cancers, 2022, 2072-6694, 14, 4, 940., CANCERS, 2022, 2072-6694, 14, 4, 940.

M. Z. GUNGOR, M. UYSAL, M. OZTURK & S. SENTURK, Systematic Analysis of Cytostatic TGF-Beta Response in Mesenchymal-Like Hepatocellular Carcinoma Cell Lines, JOURNAL OF GASTROINTESTINAL CANCER, 2021, 1941-6628, 52, 4, 1320-1335.

Conference Papers

M. UYSAL, E. ÇAKIROĞLU & Ş. ŞENTÜRK, The Vital Role of the ATG9A Gene in survival of the Malignant Pleural Mesothelioma Cells, Poster Sunumu, 33. TBS International Biochemistry Congress, 26 October 2022, 30 October 2022.

TÜBİTAK Scholarships and Fundings

Project Info

BIDEB Supports

MERVE UYSAL, Etkinlik Destekleri ve Eğitim Bursları Müdürlüğü, 2224-A Yurt Dışı Bilimsel Etkinliklere Katılma Desteği Programı, Destekleniyor, 2022 - 2.
MERVE UYSAL, Etkinlik Destekleri ve Eğitim Bursları Müdürlüğü, 2210-A Genel Yurt İçi Yüksek Lisans Burs Programı, Bursu Kesildi, 2020 - 2, 3/1/21 - 2/28/23.

Number of Panelist/Observer/Reporter Jobs

Refereeing/Panelist/Outer Consultant Count	ARDEB/BİDEB 0	TEYDEB 0	Total 0
Number of Observer/Consultant Jobs	ARDEB/BİDEB 0	TEYDEB 0	Total 0
Number of Reporter Jobs	ARDEB/BİDEB 0	TEYDEB 0	Total 0